Aeroacoustic Prediction Framework for Airborne Wind Energy Systems

A. I. Mitrea

Technische Universiteit Delft

TU Delft Delft University of Technology

Challenge the future

Note: The cover image is courtesy of Kitepower and was taken during a test flight on 6 September 2023 in Dirksland, The Netherlands, for a televised interview. It shows their airborne wind energy (AWE) system in operation.

Aeroacoustic Prediction Framework for Airborne Wind Energy Systems

by

A. I. Mitrea

in partial fulfillment of the requirements for the degree of

Master of Science
in Aerospace Engineering

at the Delft University of Technology,
to be defended publicly on Monday - May 26, 2025 at 9:30 AM.

Supervisors:	Dr. -Ing. R. Schmehl,	TU Delft
	Dr. D. Ragni,	TU Delft
Thesis committee:	Dr. ir. R. Vos,	TU Delft
	Dr. R. Merino Martinez,	TU Delft

An electronic version of this thesis is available at http://repository.tudelft.nl/.

TU Delft
Delft University of Technology

Abstract

This thesis presents the development, implementation, and validation of a low-fidelity Aeroacoustic Prediction Framework designed for airborne wind energy systems (AWES), with the Kitepower system as a case study. As AWES technology moves toward commercial viability, understanding and predicting its acoustic emissions becomes critical for regulatory compliance, public acceptance, and design optimization.

The framework integrates established analytical and semi-empirical aeroacoustic models with aerodynamic data based on derived geometry and detailed flight information. It models all major noise sources from the airborne components, such as the Leading Edge Inflatable (LEI) kite, bridle lines, tether, and onboard ram-air turbine. The most significant contributions to the overall noise signature were found to be turbulent boundary layer trailing edge (TBL-TE) noise from airfoils, modeled using the Brooks–Pope–Marcolini (BPM) approach, vortex-shedding noise from cylindrical structures such as the tether and bridle lines, and tonal harmonics produced by the rotating turbine blades, captured through Hanson's helicoidal surface theory.

To generate aerodynamic input, spanwise airfoil profiles were automatically extracted from 3D CAD models and analyzed through XFOIL. Real-time flight data was provided by an onboard sensor suite and processed through an Extended Kalman Filter (EKF), allowing dynamic simulation of flight conditions. Audio recordings were collected during test flights using GoPro® cameras, enabling experimental validation of the acoustic predictions despite the absence of calibrated SPL measurements.

Validation showed strong agreement between predicted and measured spectra up to 5 kHz, particularly for turbine harmonics and general spectral shape. Deviations in the lower tonal harmonics were primarily attributed to acoustic shielding caused by the turbine's duct structure. Additionally, the use of GoPro® cameras introduced limitations due to their lack of calibration data and the presence of internal low-pass filtering above 5 kHz. Despite these constraints, the model successfully predicted tonal peaks, including the blade passing frequency and higher-order harmonics, aligning well with the experimental observations.

Additionally, the framework investigates the influence of the propagation effects, such as atmospheric absorption and geometric spreading, and integrates them to produce realistic observer-based predictions. Despite using non-professional audio hardware, the predictions captured key features including harmonic roll-off and broadband trends, affirming the framework's validity for early-stage design and evaluation.

This work demonstrates that low-order, physics-based models paired with aerodynamic inputs and synchronized flight data can yield meaningful acoustic predictions for AWES. The framework offers modularity, computational efficiency, and adaptability for future upgrades, such as the use of calibrated microphones or high-fidelity CFD data. It serves as a foundation for future extensions in auralization, psychoacoustic testing, and component-level noise reduction strategies.

Ultimately, the thesis bridges theoretical modeling with field-based validation, supporting the responsible integration of AWES technologies into noise-sensitive environments.

A. I. Mitrea
Delft, May 2025

Contents

Nomenclature

Symbols

Symbol	Definition	Unit
a	Empirical scaling parameter for spectral shape function	$[-]$
A	Wing area	$[m^2]$
$A_{\text{min}}, A_{\text{max}}$	Min and max amplitude functions for spectral shape	$[-]$
A_R	Relative amplitude ratio in BPM model	$[-]$
$A(f)$	Amplitude at frequency f	$[-]$
b	Spanwise chord distribution	$[m]$
B	Number of blades	$[-]$
c	Chord length	$[m]$
C_L	Lift coefficient	$[-]$
C_D	Drag coefficient	$[-]$
c_0	Speed of sound in air	$[m/s]$
d	Cylinder or bridle line diameter	$[m]$
δ^*	Boundary layer displacement thickness	$[m]$
f	Frequency	$[Hz]$
f_s	Sampling frequency	$[Hz]$
f_{tonal}	Tonal frequency component	$[Hz]$
F_s	Sampling rate	$[Hz]$
G_4, G_5	Shape functions in BPM model for TE bluntness noise	$[-]$
h	Trailing edge thickness	$[m]$
k_x, k_y	Non-dimensional wavenumbers	$[-]$
L	Tether length	$[m]$
M	Mach number	$[-]$
M_x	Mach number in x-direction	$[-]$
M_r	Retarded Mach number	$[-]$
M_T	Tip Mach number	$[-]$
N	Number of FFT points	$[-]$
N_{FFT}	FFT points in signal processing	$[-]$
P	Acoustic power	$[W]$
P_{vm}, P_{Dm}, P_{Lm}	Pressure from volume, drag, and lift	$[Pa]$
p_0	Reference pressure	$[Pa]$
R_c	Reynolds number based on chord	$[-]$
SPL	Sound Pressure Level	$[dB]$
St	Strouhal number	$[-]$
St_p, St_s	Strouhal number on pressure/suction side	$[-]$
St_{peak}	Peak Strouhal number	$[-]$
t	Time	$[s]$
t_b	Blade thickness time function	$[-]$
τ_1, τ_2	Travel times for direct and reflected paths	$[s]$
T	Window duration in FFT analysis	$[s]$
α	Angle of attack	$[°]$
θ	Observer angle	$[°]$
Ψ	Radiation or grazing angle	$[°]$
ϕ_0, ϕ_s	Phase lags	$[rad]$
Δf	Frequency resolution	$[Hz]$
ω	Angular frequency	$[rad/s]$

Acronym	Definition
AWES	Airborne Wind Energy System
BEM	Blade Element Momentum
BPF	Blade Passing Frequency
BPM	Brooks–Pope–Marcolini model
CAD	Computer-Aided Design
CFD	Computational Fluid Dynamics
EKF	Extended Kalman Filter
FFT	Fast Fourier Transform
GS	Ground Station
HPF	High-Pass Filter
IMU	Inertial Measurement Unit
KCU	Kite Control Unit
LBL-VS	Laminar Boundary Layer - Vortex Shedding (Noise)
LE	Leading Edge
LEI	Leading Edge Inflatable
LBL	Laminar Boundary Layer
RANS	Reynolds-Averaged Navier–Stokes
RPM	Rotations Per Minute
SPL	Sound Pressure Level
TE	Trailing Edge
TEB	Trailing Edge Bluntness (Noise)
TBL	Turbulent Boundary Layer
TBL-TE	Turbulent Boundary Layer–Trailing Edge (Noise)
TV	Tip Vortex (Noise)
VIV	Vortex-Induced Vibration
VS	Vortex Shedding

1

Introduction

1.1. Background and Motivation

The increasing global demand for renewable energy sources has driven innovation in alternative technologies for sustainable power generation. Wind energy is one of the most widely available renewable energy sources, but it is important to note that studies suggest its capacity must increase by 320 GW by 2030 to meet the Paris Agreement climate goals [1]. Wind energy potential increases with altitude, generally following a logarithmic trend within the first few hundred meters [2]. Therefore, it is more efficient to target higher altitudes in order to access stronger and more consistent winds.

The most common wind energy production method is through axial wind turbines. The design of wind turbines has evolved over the past decades, often increasing in size due to advances in materials and manufacturing methods [3]. This has led to concerns such as visual impact and persistent noise pollution, mainly from aerodynamic sources despite noise-reduction efforts [4, 5].

In recent years, Airborne Wind Energy Systems (AWES) have emerged as a promising solution for generating electricity from wind energy, capable of harnessing stronger, more consistent high-altitude winds. AWES offer several advantages over conventional wind turbines, including access to faster wind speeds, reduced infrastructure costs, and suitability for deployment in locations otherwise inaccessible to traditional installations. The ground footprint of an AWES is usually small, considering that the main operating unit is approximately the size of a shipping container. However, the broader adoption of AWES faces several technical and regulatory challenges—among which aeroacoustics-related issues are the focus of this research.

The noise generated by such systems can pose a barrier to social acceptance, raise environmental concerns, and complicate regulatory approval. This has already been observed in the deployment of axial wind turbines, which have negatively impacted nearby residents, causing annoyance and elevated stress levels [6]. Therefore, it is essential to understand the main noise sources of AWES and to mitigate them wherever possible. A framework capable of accurately predicting the total sound generated by the system could be a valuable tool for further psychoacoustic studies and for guiding component-level improvements to reduce noise.

This research paper investigates the noise produced by the kite-powered system developed by Kitepower. Their system consists of the wing itself, which is a Leading Edge Inflatable (LEI) kite, the tether that transfers the load to the ground station, the bridle lines used to control the kite's direction and power setting, and the ram-air wind turbine for onboard electricity. An accurate prediction of the noise generated by this system is essential to enable the safe and widespread deployment of AWES in populated or noise-sensitive environments. This thesis focuses on developing a computational framework for analyzing and predicting the aeroacoustic emissions from an AWES, with the specific aim of evaluating the Kitepower system and validating the model using audio recordings made during test flights.

1.2. Research Aim and Guiding Questions

This thesis addresses the challenge of predicting and analyzing noise emissions from airborne wind energy systems (AWES), using the Kitepower system as a case study. As the deployment of AWES moves closer to commercial viability, understanding their environmental impact, particularly acoustic emissions, becomes increasingly important.

To frame the scope of this thesis, the following guiding questions are considered:

- What are the dominant noise sources associated with the components of an AWES?
- Can existing aeroacoustic models accurately represent the physics of an AWES, or be adapted to predict the noise emissions of an AWES configuration?
- How can flight test data be integrated into an aeroacoustic prediction framework to improve realism and validation?

These guiding questions set the foundation for the more detailed research question and methodology, which are introduced following the review of relevant literature.

1.3. THESIS STRUCTURE

This thesis is structured to guide the reader through the background, development, and validation of a low-fidelity aeroacoustic prediction framework for airborne wind energy systems. The chapters are organized as follows:

The report is structured in three main parts, each comprising several chapters:

• **Part I: Literature Review**

- **Chapter 2 – Overview of Airborne Wind Energy:** Introduces the fundamentals of airborne wind energy systems, describes the components of the Kitepower system, explains relevant aeroacoustic concepts, and outlines regulatory considerations.
- **Chapter 3 – AWES Acoustic Emissions:** Reviews prior studies and existing literature related to AWES noise generation. Discusses dominant mechanisms such as vortex shedding, airfoil self-noise, and tonal noise, as well as previous experimental observations.
- **Chapter 4 – Problem Statement:** Description of the objectives and the research questions of the thesis.

• **Part II: Methodology**

- **Chapter 5 – Aeroacoustic Prediction Model:** Details the theoretical basis and implementation of the prediction framework, including component-level noise modeling and sound propagation formulations.
- **Chapter 6 – Geometry Extraction and Properties:** Describes the automated method developed to extract geometric data from 3D models of the kite and turbine. These extracted profiles are used to obtain relevant aerodynamic properties for noise prediction. The tether and bridle lines are modeled as simple cylindrical structures and are not included in the 3D extraction process.
- **Chapter 7 – Simulation and Analysis Tools:** Explains the role of the Extended Kalman Filter (EKF) in providing time-resolved flight data and outlines how XFOIL is used to obtain aerodynamic parameters for the kite and turbine airfoils.
- **Chapter 8 – Audio Analysis:** Presents the experimental setup, describes the audio processing techniques used for frequency-domain analysis, and addresses limitations related to microphone response.

• **Part III: Results and Conclusion**

- **Chapter 9 – Results and Discussion:** Compares predicted acoustic spectra with flight recordings, highlights key findings, and evaluates the accuracy and limitations of the prediction model.
- **Chapter 10 – Conclusions and Recommendations:** Summarizes the main conclusions of the study, discusses the broader implications, and offers guidance for future research and model enhancements.

This structure aims to provide a clear and logical flow from theoretical context to practical implementation, enabling a thorough understanding of the aeroacoustic behavior of AWES and the capabilities of the proposed prediction framework.

I

Literature Review

2

Overview of Airborne Wind Energy

As the name suggests, airborne wind energy systems (AWESs) represent devices that can convert wind energy into electrical energy using one or multiple flying, buoyant, or lifting devices. All these conversion concepts are connecting the lift devices to the ground employing one or multiple tethers. Moreover, some of the concepts use additional bridle lines that make the connection between the tether and the lifting device in order to distribute the load. Therefore, airborne wind energy (AWE) can be classified into three main groups based on their working principle as presented in Figure 2.1. Ground-gen refers to the systems that generate electricity with a generator positioned inside the ground station (GS), which can be fixed or moving. The fixed type is more common and uses a rotational hinge such that the tether can easily be guided around the GS. The moving ground stations are usually constructed on a horizontal loop track or a carousel-type, but their complexity brings them quite far from realization. However, for both moving GS and fixed GS types, the working principle is similar: a tether is wrapped around a drum and the reeling in or out of the tether converts linear motion into shaft power. The last category, also named Fly-gen, includes devices where the generator is placed on the flying device, requiring a conductive tether for electricity transfer. However, these three groups are still very broad. Within each category, lots of design choices can be made for their structure or for the kite itself. Soft kites, hard kites, or even hybrid are being developed. As this field has seen significant interest over the last years, there are continuous advancements or new technologies brought to the current designs. More detailed overviews of the implemented concepts can be found in Cherubini et al. [7] and Schmehl [8].

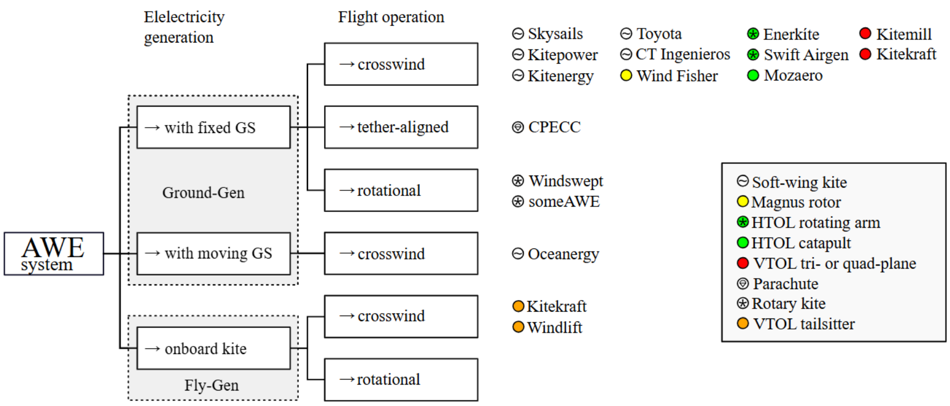

Figure 2.1: Classification of AWES Technologies as of 2019. Retrieved from Schmehl [9].

2.1. Airborne Wind Energy System of Kitepower

This report will focus on the architecture of Kitepower, a Dutch company founded in 2016 in Delft. The system used by the company has as its flying device a leading-edge inflatable (LEI) kite that is flying figure of eights in crosswind conditions. A brief description of each component forming the system will follow below. This will help to better understand the working principle of the AWE system, and to reach the goal of identifying the main noise sources for the analysis. A generic soft-kite ground-gen system is presented in Figure 2.2, including the wireless network connection and sensors. Thus, the overall setup comprises a flying kite with its kite control unit (KCU) connected through a single braided tether to a fixed ground station, which also features an electric winch and the control center [10].

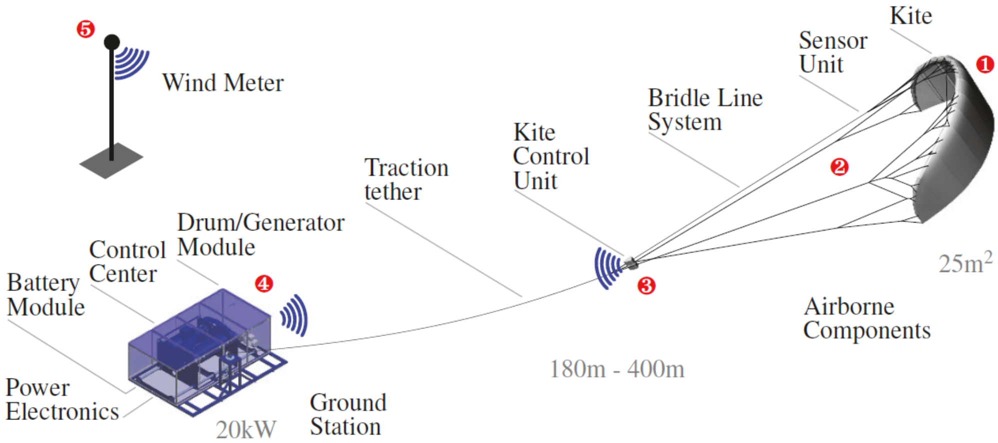

Figure 2.2: System components, sensors, and wireless connections of a generic kite power system. Retrieved from van der Vlugt et al.[11].

2.1.1. LEADING EDGE INFLATABLE KITE

Multiple iterations led Kitepower to use a LEI kite of an impressive size of 60 square meters called Falcon V9.60, which has a rated power of 100 kW, and it is presented in Figure 2.3. The kite's design is inspired by kite surfing, and it features a sail with inflatable beams in spanwise and chordwise directions. The main inflatable tube forms the entire leading edge of the kite, but it connects with the trailing edge around the tips of the canopy. The chord in the middle of the kite reaches around 4 m, and it is slowly decreasing towards the tips. The projected area of the kite is $A_{proj} = 47\ \text{m}^2$ with a flattened area of $A_{flat} = 60\ \text{m}^2$, that is sectioned in 13 parts by inflatable struts. The canopy between the struts has a small thickness compared to the inflatable parts, and it is a tensile member of the structure. The total mass of the kite is around 62 kg including the bridle system. Under the aerodynamic load, the kite can suffer large deformation since the materials do not have structural rigidity, so the internal air pressure inside the inflatable members is important in order to retain the desired shape. Some of these deformation modes will be discussed in Section 2.2.5.

Figure 2.3: Photo of the 60 m^2 kite compared to the smaller designs (25 m^2 and 40 m^2) of Kitepower. Retrieved from Bouman [12].

2.1.2. TETHER AND BRIDLE LINES

The kite is attached to the ground station through a single braided tether. In the case of Kitepower, the tether is not a conductive one, therefore not transmitting any electrical power or signals to the kite. Thus, its only purpose is to transfer the traction force towards the drum, as the tether and bridle lines are tensile structures engineered solely to transfer tensile loads. Depending on the phase in which the flight is, the distance between the position of the kite and the ground station can increase or decrease. Therefore, the length of the tether that is in the air is constantly changing. This is done by reeling the tether onto the winch's drum (retraction phase) or by reeling it off (traction phase). It is important to mention that one of the limitations of the reeling speed is dictated by the maximum force that the line can sustain. This is important as there is no other redundancy in the system, making it a critical safety component. In his work, Loyd [13] formulated analytical models to predict the power output of basic kites engaged in reel-out motion, as well as those incorporating crosswind maneuvers. It was concluded that the power output is highly influenced by the aerodynamic drag generated by the tether and bridle lines, which can constitute a substantial portion of the overall drag as they are held in the air [14]. Therefore, all these variables must be considered when designing and choosing the material. Kitepower uses a braided tether from Dyneema® of 14 mm in a set-up similar with the one pictured in Figure 2.4.

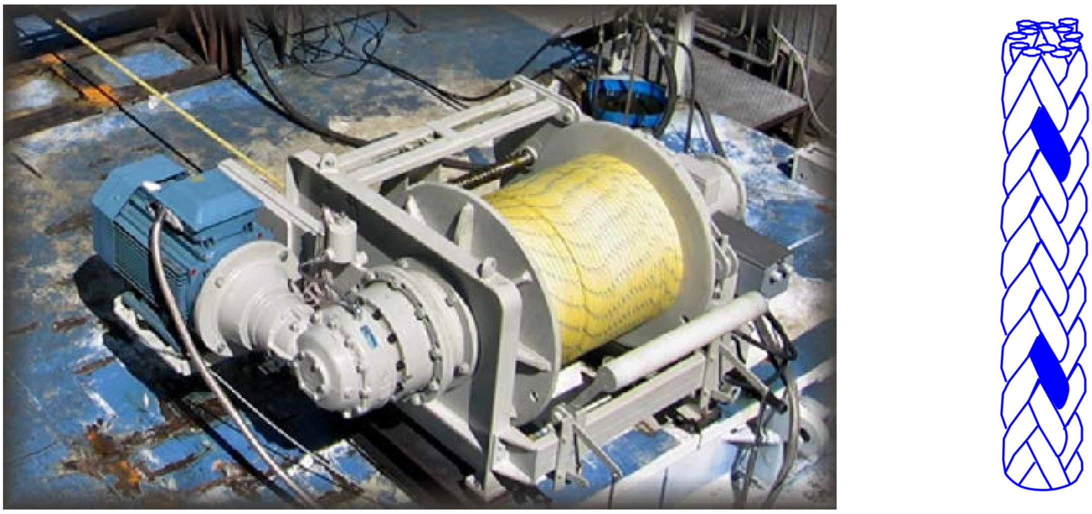

Figure 2.4: Tether on the drum actioned by the winch (left) and depiction of braided tether (right). Retrieved from Bosman et al. [15].

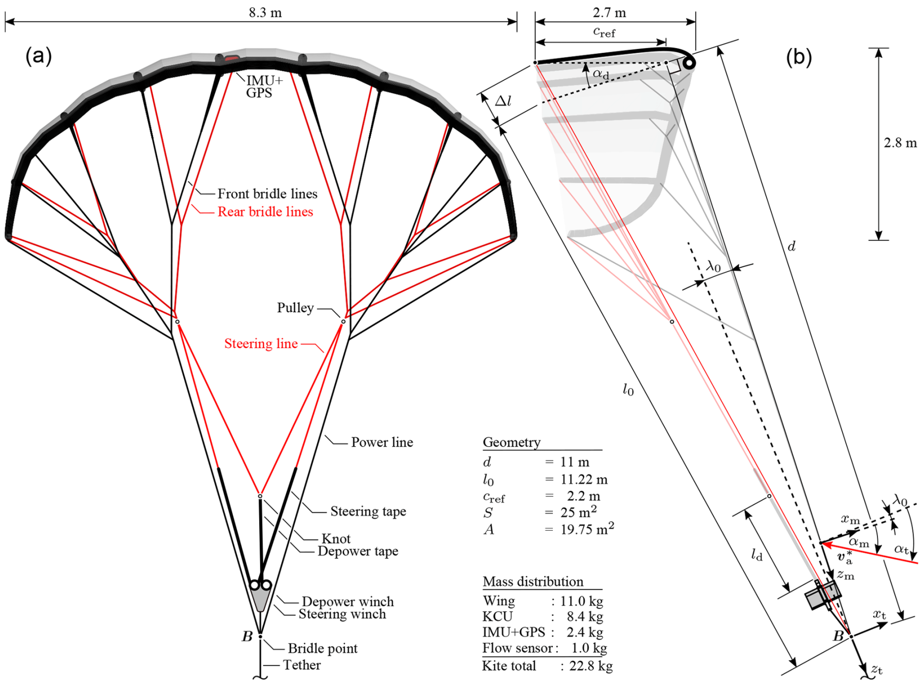

Figure 2.5: Front view (a) and side view (b) of the LEI V3 kite with the bridle lines. Retrieved from Oehler & Schmehl [16].

It is important to notice that the tether is not directly connected to the kite. This connection is done through a joint called the bridle point, where the tether and the bridle lines meet. A depiction of this is presented in Figure 2.5. The steering or powering of the kite is controlled by changing the distribution of the bridle lines attached to the leading edge and the tips of the kite. One can imagine that the shape of the wing is dictated to a large degree by the bridle geometry. These lines must constantly adapt to the flight conditions. In order for the tension inside the lines to be balanced, pulleys offer the ability to adjust the apparent forces within the bridle system. The bridle lines used for steering are connected to steering tapes that pass through the KCU. When these tapes are varied asymmetrically, the wing shape is deformed, and the aerodynamic forces introduce a twisting moment. Moreover, pulling both steering lines changes the angle of incidence of the kite, which in fact can power or depower the wing. The bridle lines are thinner than the tether due to the distributed load. The thicknesses used by Kitepower for the bridle lines are present in a wide variety, ranging from 2 to 8 mm, and their added length sums to around 420 m.

2.1.3. KCU and Onboard Ram-Air Turbine

The kite control unit (KCU) is responsible for controlling the direction of the wing by adjusting the lengths of the bridle lines. The KCU receives all the steering commands wirelessly from the control center (inside the ground station) and it can steer or (de-)power the wing. The KCU is situated at approximately 20-25 m below the kite and it does not receive any electricity from the ground as the tether is not conductive. Because all the motors and sensors inside the KCU need power to function, it was opted to integrate an onboard turbine next to the control unit. The primary role of this turbine is to convert the rotational mechanical energy into electricity. In this way, the turbine can supply all the electrical components of the KCU, together with the GPS and inertial measurement unit (IMU+) sensors.

Figure 2.6: Example of a KCU with onboard ram-air turbine and mounted shroud. Retrieved from Van Den Kieboom [17].

2.1.4. Ground Station

The main function of the ground station is to locate the control center and all the components needed for converting the traction force into electrical energy. The tether exits the ground station through a special directional pulley, also named swivel head. During the reel-in phase, an electric motor spins the drum to which the tether is attached. The generator is used during the reel-out with a clutch actuation, such that the speed of the drum is controlled. At the moment, the ground station of Kitepower is entirely fitted inside a standard cargo container, making the transportation and deployment processes easier. An example of all the components inside a ground station is shown in Figure 2.7. The electricity produced during the traction phase is stored in a battery, such that a part of it can be used for the retraction. This dependency on the battery creates some complications regarding the direct connection to the grid.

2.2. Terminology for AWES

2.2.1. Flight Envelope

For most kite systems, the ground station is taken as a reference point, especially in the case of fixed GS types. Based on this, two zones are delimited by the wind direction: the downwind zone (in the direction of the velocity vector from the ground station) and the upwind zone (from where the wind blows, opposite to the vector's direction) [19]. The kite can fly in a controlled manner only in the downwind area, forming a region represented as a quarter sphere, as shown in Figure 2.8. This quarter sphere, with the ground station at its center, is also referred to as the 'wind window'. Within this flight envelope, two important angles define the position of the kite: the azimuth and the elevation angle. The azimuth (φ) is the angle between the projection of the kite's position and the wind direction in the horizontal plane, parallel to the ground. The elevation angle (β) defines the angle in the vertical plane between the kite's position and the ground. The power zone, located within the wind window, is where the kite generates maximum pulling force due to higher angles of

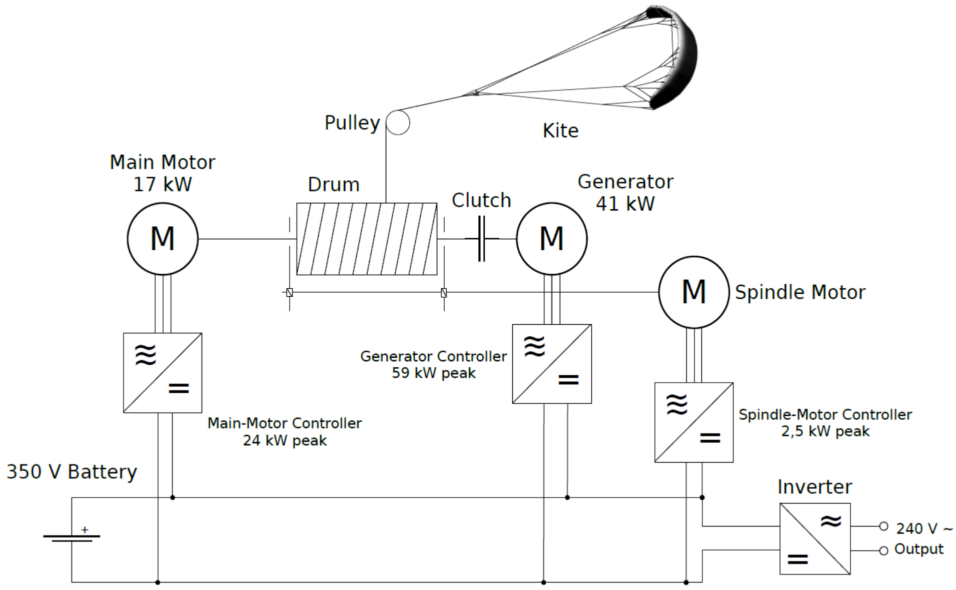

Figure 2.7: Schematic of a generic ground station. Retrieved from Fechner [18].

attack. To maximize energy output, the kite is flown in crosswind patterns such as circles or figure-eights (as Kitepower does). In contrast, positions near the wind window edge, such as the zenith, yield minimal force and are mainly part of the transition phase.

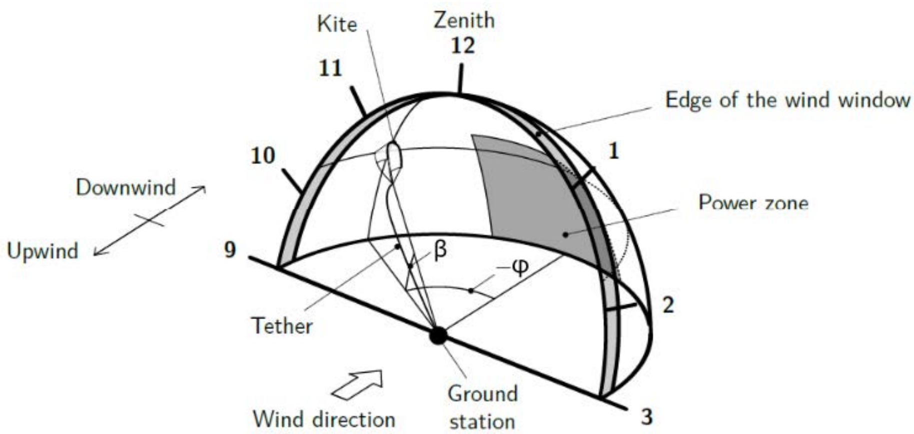

Figure 2.8: Terminology of the flight envelope. Retrieved from Friedl [19].

2.2.2. FLIGHT PHASES

The flight plan usually consists of two main phases called reel-in and reel-out and the transitions between these two phases. The reel-out is the phase in which the kite flies in figure-of-eights, as mentioned previously. This is when the power is generated, also called traction phase. Even if the tether is reeled-off, so the distance between the wing and ground station increases, the kite is controlled such that it starts turning at a pre-defined constant azimuth angle.

Once it reaches the maximum tether length, there is a transition phase in which the kite is brought towards the 12 o'clock direction of the wind window. The KCU depowers the wing, such that it requires less energy to be pulled back by reeling-in the tether around the drum. Once the starting position is reestablished, the second transition phase starts in order to prepare the kite for another power generation cycle. A simulation of such a flight path is presented in Figure 2.9

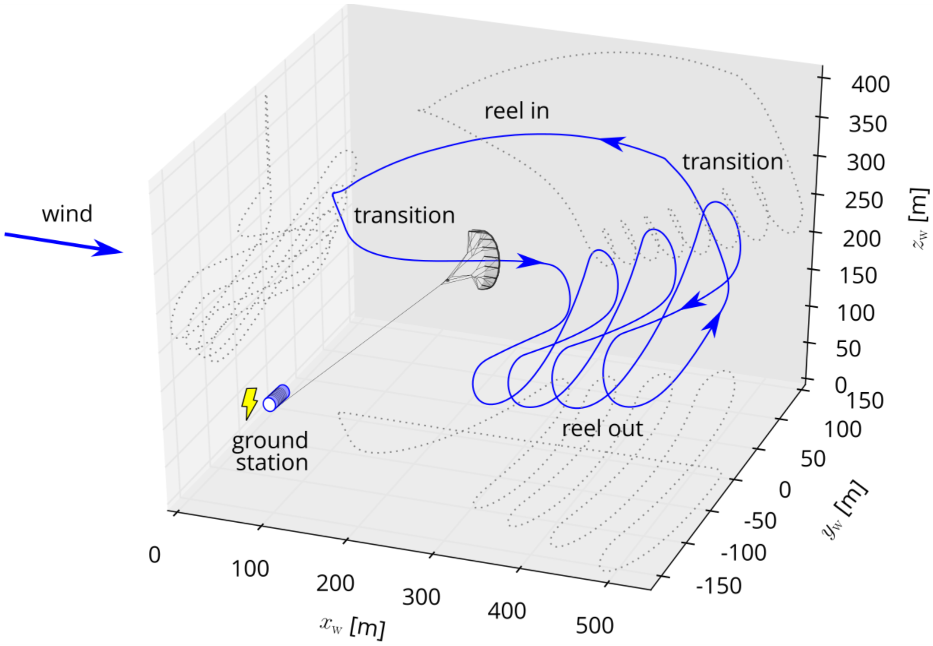

Figure 2.9: Simulated path of a LEI kite showing all the flight phases. Retrieved from Fechner [18].

2.2.3. PUMPING CYCLE

Specific to AWE devices, the combination of the tether reel-in and reel-out creates the so-called 'pumping cycle'. Similar to a 2-stroke thermodynamic cycle, only one of these phases will generate useful energy, while the other will consume a part of it. To be more specific, the reel-out phase produces electricity, while during the reel-in a small part is used to bring the kite back into the position for another pumping cycle. A simulation of a generic power cycle is presented in Figure 2.10 for a mean wind speed of 6 m/s. The net mechanical power output is around 12 kW (also presented with the dashed line), but it can be seen clearly that during reel-out, the power output is usually significantly larger.

The power fluctuations observed during the reel-out phase result from the interaction between the strong turbulence of the simulated wind field and the compensatory response of the control system. The diagram on the right presents the mechanical power curve for this specific pumping kite power system, spanning the entire range of ground wind speeds. The marked symbol denotes the operational state analyzed in the left diagram, which closely aligns with the nominal operating conditions of the system. At this nominal point, the mechanical power output is approximately 12 kW. However, due to conversion losses, the resulting nominal electrical power output is reduced depending on generator efficiency and other factors.

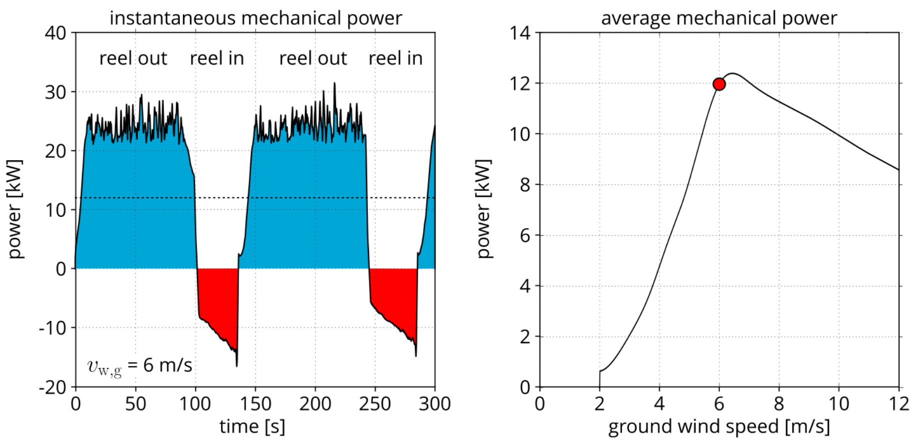

Figure 2.10: Simulation of two power cycles with a mean wind speed of 6 m/s. Retrieved from Schmehl [20].

APPARENT WIND SPEED

The wind speeds in which the Kitepower operates are anywhere between 4-15 m/s, so the power that could be directly extracted from it can be considered rather low. Flying crosswind increases the apparent wind speed experienced by the kite, therefore increasing the lift force. The apparent wind speed is the vector difference between the wind velocity and kite velocity (highly dependent on the reeling speed), as presented in Equation 2.1. The vector summation, also presented graphically in Figure 2.11, demonstrates the benefit of this crosswind flying maneuver. In real-life scenarios, the apparent speed can reach values up to 40 m/s in normal wind conditions.

$$\mathbf{v_a} = \mathbf{v_w} - \mathbf{v_k} \tag{2.1}$$

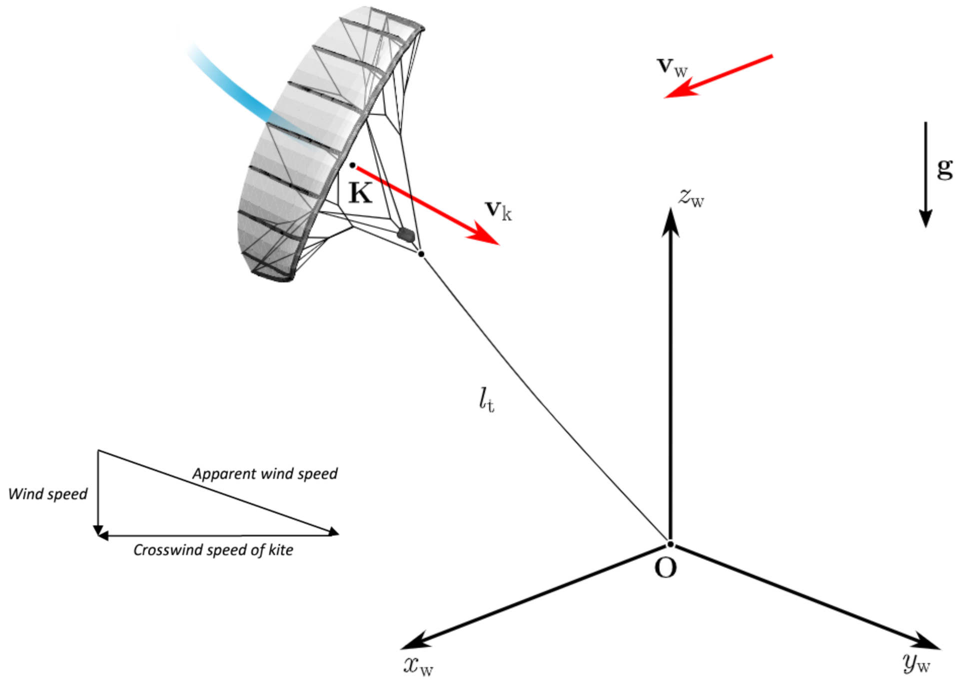

Figure 2.11: Apparent wind speed vector summation for the kite. Retrieved and adapted from Schmehl [21].

2.2.4. KITE KINEMATICS

In 1980, Miles L. Loyd [13] provided a foundational theoretical analysis of crosswind kite power, quantifying the potential energy extraction from tethered wings flying in crosswind patterns. In the ideal case, the maximum power that can be extracted by a kite is given by:

$$P = \frac{2}{27}\rho A v_\mathrm{w}^3 C_L \left(\frac{C_L}{C_D}\right)^2 \tag{2.2}$$

where ρ is the air density, A is the wing area, C_L and C_D are the lift and drag coefficients respectively, and v_w is the wind speed [22]. This expression can also be related to the wind power density, defined as:

$$P_w = \frac{1}{2}\rho v_\mathrm{w}^3 \tag{2.3}$$

2.2.5. DEFORMATION MODES OF LEI KITE

Since LEI kites are not rigid, they are subject to multiple types of deformation modes. The membrane can only resist tensile forces, while the only way to oppose compressive forces is through the inflatable tubes. Deformation modes refer to the various ways in which the wing can change its shape and deform during operation. These deformation modes are classified based on the kite's geometry—from local to global—or by the frequency they exhibit, from slow to fast. Figure 2.12 presents the most important deformation modes that a soft kite can experience. Leuthold [23] investigated these modes and concluded that local deformations are usually faster than global ones. Therefore, it is more common for one section of the kite to experience a deformation mode than for the entire structure to do so.

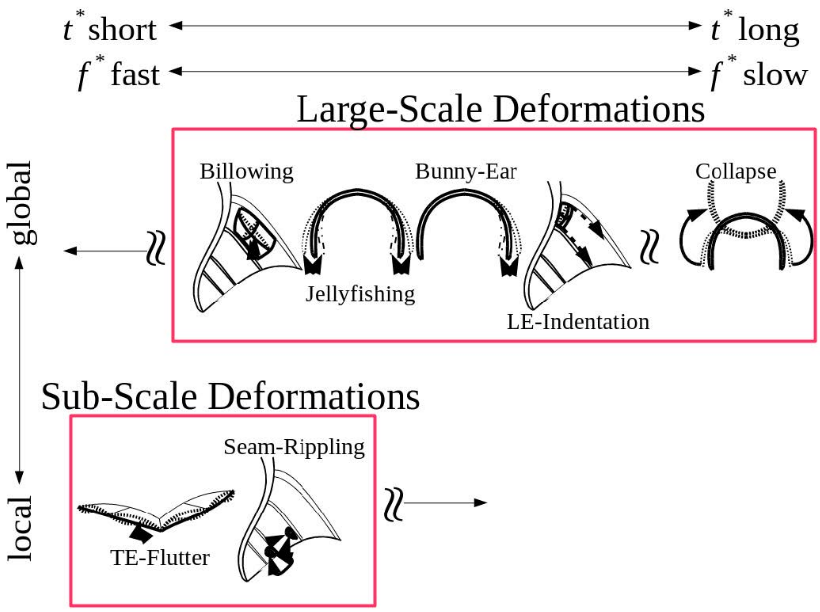

Figure 2.12: Typical deformation modes seen in operation of LEI kites. Retrieved from Leuthold [23].

Considering that the audible range for humans spans from 20 Hz to 20 kHz, only a subset of the deformation modes generates noise within this range. Leuthold [23] concluded that the large-scale deformation behaviors shown in Figure 2.12 occur at frequencies below 20 Hz and are thus inaudible to the human ear. In contrast, higher-frequency sub-scale deformation modes—specifically trailing-edge (TE) flutter and seam rippling—exhibit frequencies above the 20 Hz threshold and could therefore be perceived as audible noise.

Trailing-edge flutter refers to the deformation of the canopy's free trailing edge as a result of periodic aerodynamic force oscillations caused by vortex shedding. This phenomenon is very common in kite surfing and can become relatively loud. It has been observed that Kitepower is currently experiencing this TE fluttering, so it would be highly valuable to simulate the noise generated by this deformation mode. Leuthold [23] performed an analysis on video footage from a test flight of the TU Delft KitePlane, where the effects of trailing-edge fluttering were clearly visible. Based on the recording's frame rate, he concluded that the fluttering frequency is between 20.4 Hz and 87.1 Hz.

Seam rippling is another sub-scale deformation mode that occurs near the struts close to the trailing edge in the form of a traveling wave. In these specific spots, the tension in the chord-wise direction is much smaller compared to the tension in the span-wise direction. However, this deformation mode is extremely local, and its frequency could not be identified from the video footage by Leuthold.

2.3. FUNDAMENTALS OF AEROACOUSTICS

Sound, in the simplest way of defining it, is the propagation of pressure waves through a medium, such as air [24]. These waves can be heard by humans and animals within a specific frequency range, typically from 20 Hz to 20 kHz. If sound is perceived as unwanted, it is referred to as noise. The perception of noise is subjective and depends on various factors such as loudness, frequency, and individual sensitivity.

IMPORTANT QUANTITIES

One metric used to measure sound is the sound pressure level (SPL), which relates the effective pressure of a sound wave to a reference pressure. SPL is calculated using the following equation [25]:

$$SPL = 10 \cdot \log_{10}\left(\frac{p_{\mathrm{rms}}^2}{p_{\mathrm{ref}}^2}\right) = 20 \cdot \log_{10}\left(\frac{p_{\mathrm{rms}}}{p_{\mathrm{ref}}}\right) \tag{2.4}$$

Here, p_{rms} represents the root mean square (RMS) sound pressure, and it is calculated using the time integral of pressure fluctuation as [26]:

$$p_{\text{rms}} = \sqrt{\lim_{T\to\infty}\left(\frac{1}{T}\int_0^T p^2(t)\,dt\right)} \tag{2.5}$$

The term p_{ref} is the reference pressure, set at $2\cdot10^{-5}$ Pa, which corresponds to the human hearing threshold at 1 kHz. According to this definition, doubling the sound pressure of the source results in an increase of 6 dB (since $20\cdot\log_{10}(2)\approx 6\,\text{dB}$). Similarly, when the amplitude is increased by a factor of 10, the difference in sound pressure level will be 20 dB.

Another important quantity is sound power, which represents the total energy emitted by a sound source and is independent of the observer's position. Unlike sound intensity or sound pressure, which decrease with distance, sound power remains constant because it accounts for the full energy output over a surrounding surface [26]. This is explained by the inverse square law, which states that as sound radiates spherically, its intensity diminishes with the square of the distance, while the surface area over which it spreads increases by the same factor. As a result, the total power, calculated as intensity integrated over the area, remains unchanged, as shown in Figure 2.13.

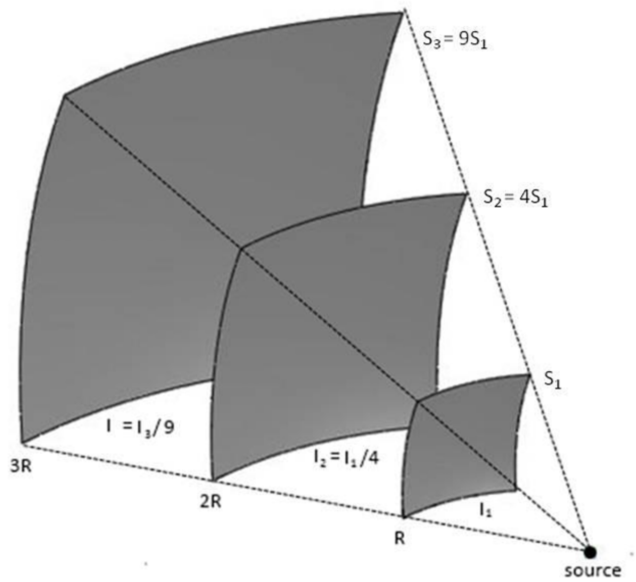

Figure 2.13: Depiction of the law of spherical spreading. Retrieved from Dijkstra [27].

NOISE WEIGHTING

The sensitivity of humans to noise depends highly on the frequency of the source. While frequencies in the range of 3000–4000 Hz have a hearing threshold of 0 dB, the threshold for lower frequencies is significantly higher [25]. To address this, researchers organized a frequency weighting depending on the level of sensitivity or annoyance, which is applied to make noise measurements more representative of human perception. Such a weighting function $W(f)$ can be described as:

$$W(f) = 10^{\Delta L_W(f)/10} \tag{2.6}$$

where $\Delta L_W(f)$ is the relative response (usually negative) in decibels at a specific frequency. Therefore, the weighted sound pressure level is calculated with [26]:

$$SPL_w = SPL + \Delta L_W(f) \tag{2.7}$$

Noise investigations in the 1/3 octave bands can be carried out with several weighting filters, such as A-weighting, B-weighting, and C-weighting, which are the most commonly employed. These filters are specifically designed to reduce the contribution of lower frequencies to the overall noise level, as shown in Figure

2.14. The OASPL (overall A-weighted sound pressure level) is the most known way of describing the total contribution of a noise source over the entire frequency spectrum.

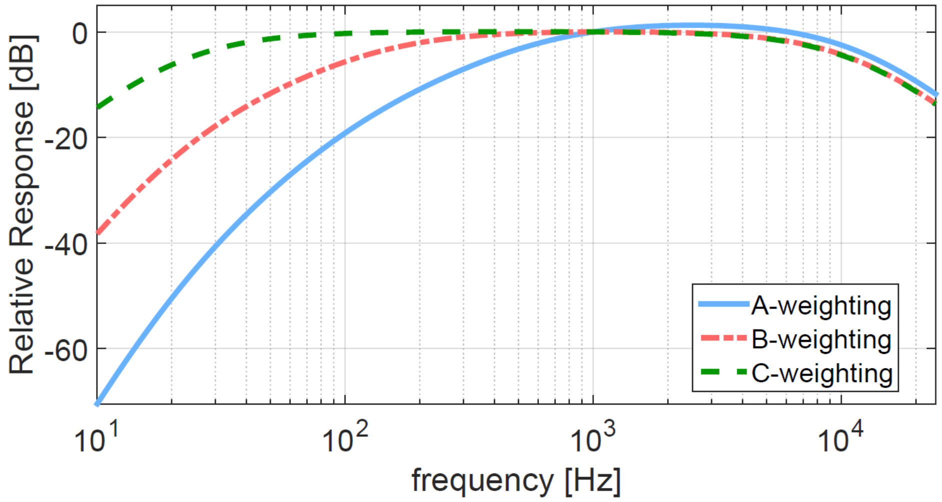

Figure 2.14: Relative response in dB of different noise weighting methods. Retrieved from Wagner [25].

DIRECTIVITY

A source that emits with the same power omnidirectional is called a monopole. In practice, any sound source whose dimensions can be considered much smaller than the wavelength of the sound radiated can be regarded as a monopole radiating sound equally in all directions [28]. The sound power Π radiated by a monopole source is proportional to the frequency squared [29]:

$$\Pi \sim \omega^2 = (2\pi f)^2 \tag{2.8}$$

The other two common directivity patterns are referred as to dipole and quadrupole, depending on the shape they exhibit. A dipole usually has the maxima along 0° and 180° directions and no sound radiated along the 90° and 270° directions. The dipole power varies with frequency as ω^4 and a quadrupole as ω^6 [30], which means that dipoles or quadrupoles are less efficient at radiating low frequency sounds with the same source strength. Moreover, the sound intensity of a monopole decays as $\frac{1}{r^2}$ because the power radiates spherically over a surface area proportional to $4\pi r^2$. In contrast, the decay for a dipole is $\frac{1}{r^4}$ and a quadrupole is $\frac{1}{r^6}$. Because of this, quadrupole sources are usually disregarded in the far-field noise calculations. These patterns are presented in Figure 2.15.

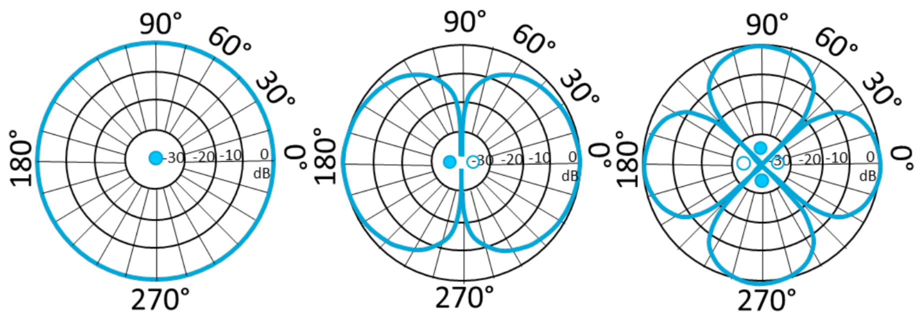

Figure 2.15: Examples of monopole (left), dipole (center), and quadrupole (right). Retrieved from Russel [31].

TONAL AND BROADBAND NOISES

A sound source may emit over a wide range of frequencies simultaneously, which is referred to as broadband noise. If the energy of a sound is concentrated at a specific frequency, it is classified as tonal noise [24].

Harmonic or tonal noise is the periodic component represented by a pulse that repeats at a constant rate [32]. For an ideal propeller with B blades spinning at a constant rotational speed N, harmonic noise appears only at multiples of the fundamental frequency $B \cdot N$. In contrast, broadband noise is more complex, exhibiting inherently random behavior and spreading across the entire frequency spectrum [33].

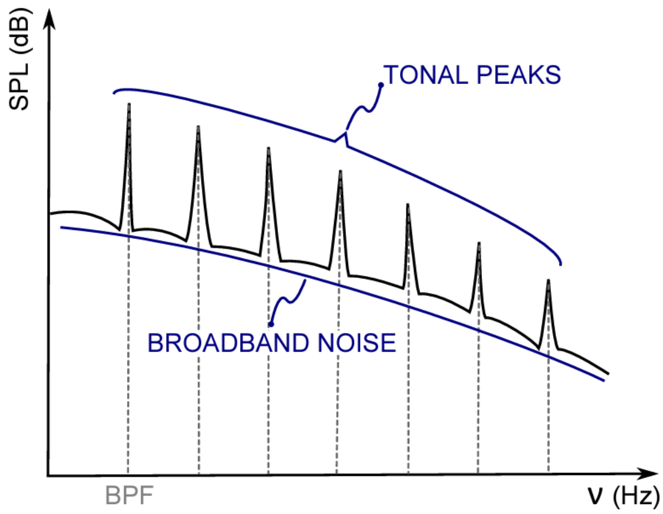

Figure 2.16: Examples of a propeller noise spectrum displaying tonal and broadband components. Retrieved from Marinus [34].

2.4. PHYSICS OF OUTDOOR SOUND PROPAGATION

In outdoor environments, the sound pressure level (SPL) at the receiver's location often differs from that at the source due to factors such as geometric spreading, atmospheric absorption, and ground interactions. Accurate simulation of outdoor sound propagation requires adjusting the source SPL to account for distance-related attenuation, weather conditions, and terrain characteristics [35]. A wide range of environmental variables, such as wind direction, temperature and wind gradients, and atmospheric turbulence, can significantly influence the result. Sound propagation is primarily governed by five physical phenomena: absorption, reflection, refraction, diffraction, and scattering [36]. These effects are illustrated in Figure 2.17 and further discussed in Section 5.4.

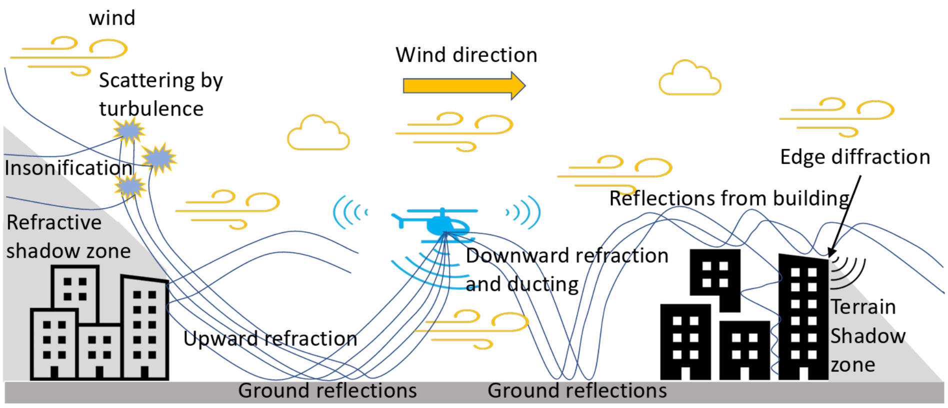

Figure 2.17: Illustration of outdoor sound propagation mechanisms. Retrieved from Yunus [36].

2.4.1. DOPPLER FREQUENCY SHIFT

When a sound source is moving relative to a static observer, the frequency the observer hears is different from the emitted one. This pitch change happens because of a difference in time between each emission, and it depends on the moving speed. Therefore, if the source of the sound wave moves towards the observer, each successive cycle is emitted from a closer position than the previous cycle [37], meaning that the frequency increases. When the source moves away from the observer, the opposite effect happens. The equation that calculates this shift is:

$$f_o = \frac{f_s}{1 - M\cos\theta} \tag{2.9}$$

where f_s is the frequency at the source, f_o is the frequency at the observer, M is the Mach number, and θ is the angle between the moving axis and the observer.

2.4.2. GEOMETRICAL SPREADING

While it is often described as a loss, during spherical spreading there is no actual energy loss, but rather an energy spread. Because the sound propagates over a larger area, the amplitude of the sound waves decreases. The type of spreading usually depends on multiple factors and affects sound attenuation differently, but the most common form is spherical spreading. This concept is depicted in Figure 2.13 and is described in ISO 9613-2:1996 [38] and ISO 9613-2:2024 [39].

2.5. REGULATIONS FOR AIRBORNE WIND ENERGY SYSTEMS

Airborne Wind Energy (AWE) systems face significant regulatory challenges due to their unique characteristics, operating at the intersection of aviation and renewable energy. Current frameworks are fragmented, with most prototypes operating under special permits granted by local aviation authorities. These temporary permits lack standardization, underscoring the need for harmonized regulations at both national and international levels [40]. Regulatory authorities are exploring three primary categories for integrating AWE systems:

1. **Unmanned Aerial Vehicles (UAVs):** AWE systems with autonomous capabilities may align with UAV regulations, but discrepancies between jurisdictions complicate this pathway.
2. **Air Navigation Obstacles:** Similar to wind turbines, AWE systems could be classified as obstacles requiring visibility markings, lighting, and operational constraints in accordance with ICAO standards.
3. **Tethered Gas Balloons:** Some static AWE systems could follow certification pathways similar to tethered balloons, particularly under CS-31TGB, which specifies safety and tether requirements.

International bodies like ICAO, FAA, EASA, and JARUS are actively exploring tailored regulations for AWE systems [40]. Collaborative efforts aim to close gaps in existing frameworks and enable integration into controlled airspace. The harmonization of global rules will be vital to ensure seamless operation across jurisdictions and promote industry growth.

2.5.1. NOISE REGULATIONS

The key concerns regarding social acceptance of airborne wind energy systems are identified as similar to those surrounding traditional wind turbines: safety aspect, visual impact, sound emissions, ecological impact, and siting [6]. This work focuses specifically on sound emissions and strategies to minimize the noise footprint.

Excessive noise can cause stress, sleep disruption, reduced performance, and communication issues, prompting regulatory controls for products such as vehicles, aircraft, and wind turbines [41, 42]. For AWES, compliance with noise regulations will be crucial for certification and public acceptance, ensuring minimal disruption to communities and ecosystems [43]. However, Schmidt et al. [6] noted that many studies on AWE social acceptance rely more on assumptions than empirical evidence. As such, this research references wind turbine noise regulations due to system similarities.

In the Netherlands, wind turbine noise regulations aim to protect noise-sensitive areas like residential zones, without distinguishing between urban and rural locations. A national limit of 47 dB for the yearly averaged equivalent sound level L_{den} applies at sensitive receptors [44]. The L_{den} metric accounts for three time periods— day (07:00–19:00), evening (19:00–23:00), and night (23:00–07:00) —with 5 dB and 10 dB penalties added to evening and night noise levels, respectively [45]. It is calculated as follows [46]:

$$L_{\text{den}} = 10 \cdot \log_{10}\left(\frac{12}{24} \cdot 10^{\frac{L_{\text{day}}}{10}} + \frac{4}{24} \cdot 10^{\frac{L_{\text{evening}}+5}{10}} + \frac{8}{24} \cdot 10^{\frac{L_{\text{night}}+10}{10}}\right) \tag{2.10}$$

Additionally, a specific nighttime limit of 41 dB applies. A 5 dB penalty may be added for tonal components, though this is rarely an issue with modern axial wind turbines [27], but it should be assessed for AWES. While international regulations vary—some using region-specific limits—they all aim to reduce environmental and social noise impacts. A similar framework is likely to emerge for AWES, highlighting the importance of understanding noise sources early in the design process.

3

AWES ACOUSTIC EMISSIONS

Noise constitutes a significant challenge in technologies involving moving parts and fluid dynamics, with Airborne Wind Energy Systems (AWES) being no exception. A thorough understanding of the acoustic emissions from each AWES component and the factors influencing them is critical. Such knowledge is essential to mitigate effects that may otherwise impact nearby human communities, disrupt wildlife habitats, and raise broader environmental concerns.

This section explores the topic of AWES acoustics by first reviewing foundational studies and early measurements of sound levels. It then progresses to analyze specific noise sources within AWES and examines models capable of predicting their behavior. Addressing these issues provides a comprehensive approach for understanding and managing the acoustic footprint of AWES and supporting its future development.

3.1. PREVIOUS NOISE MEASUREMENTS AND OBSERVATIONS

Szücs [47] published in 2017 one of the first research papers that investigated the acoustic environmental impact of the airborne wind energy system of Kitepower. Using an array of microphones, she took measurements at different positions from the ground station at distances of 5, 10, 25, 50, 100, and 200 m. At distances up to 25 m, the generator and electric motor used for reeling are the main sources of noise. At around 25 m, some peaks in frequencies in the range of 500–1000 Hz were identified, and it was concluded that the vortex shedding of the tether could produce this noise. The most interesting results were found at a distance of 100 m from the GS. The highest SPL values were found at this location and they were correlated to the noises produced by the flying kite due to their periodicity. This is demonstrated in Figure 3.1.

The SPL values depending on the measuring position are presented in Figure 3.2. However, there is no clear conclusion drawn from the values obtained through the measurements in this research paper. The main reason for this is the fact that the wind noise was included in the results. The microphones were not equipped with a dead-cat or wind-muff to prevent it. Szücs [47] observed that in some of the recordings, the wind noises were louder than the ones produced by the AWES.

Bouman [12] published a relevant study on the aeroacoustics of AWES, focusing on two companies with different configurations: Kitepower and Kitemill. This paper evaluates analytical and semi-empirical models for the AWES components and validates them using experimental data measured during flight tests. Measurements taken up to 650 m from the ground station were recorded and analyzed. Additionally, measurements of the background noise (without the kite flying) were taken. It was demonstrated that removing wind noise from these measurements through spectral subtraction or high-pass filters eliminated important parts of the data. The comparisons for two different scenarios are shown in Figure 3.3. Both graphs display two distinct bumps in the measurement data, the first within the 300–400 Hz range and the second around 1–2 kHz, depending on the flight velocity. For the lower speed, the predictive analysis closely matches the measurement data. The predictions replicate the behavior of the bumps, albeit with slightly different SPL values and frequencies. Bouman suggested that these frequency bumps were due to vortex shedding from the tether at lower frequencies and from the bridle lines at higher frequencies. However, findings from the current research paper suggest that this interpretation is only partially accurate.

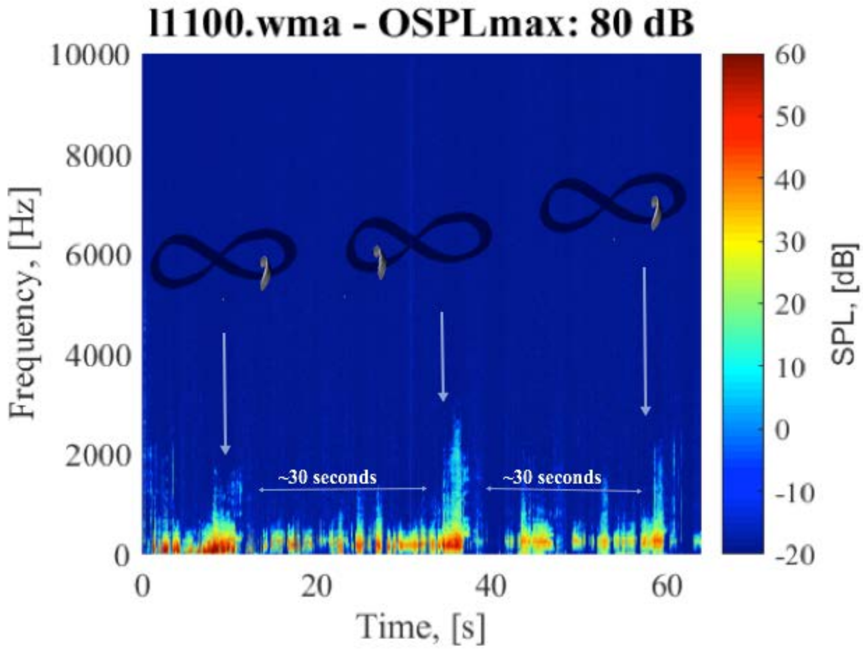

Figure 3.1: Noises measured at 100 m from the GS showing the correlation with the kite position. Retrieved from Szücs [47].

The broadband noise from the kite was analyzed using the Amiet model [48, 49] and the BPM model [50]. Upon validation, it was evident that the BPM model outperformed the Amiet model and provided better results. However, definitive conclusions cannot be drawn due to the nuances of the model's implementation and potential inaccuracies in the sound recordings' analysis. The components analyzed were the tether, bridle lines, kite, and KCU bullet. However, the noise from the KCU bullet was found to be insignificant and was therefore excluded from further analysis.

It is important to note that the analysis by Bouman [12] did not include several sound phenomena that might be of high importance. These include the sounds produced by the ram-air turbine and the trailing edge flutter of the kite itself. On the day of the experimental measurements, the turbine was not attached; therefore, its sound was neither measured nor included in the prediction code. Furthermore, trailing-edge flutter was observed in the video footage recorded during testing but was not modeled in the prediction code. These noise sources contribute both tonal and broadband noise, and it is believed that the tonal noise could have significant SPL peaks.

The noises produced by the ram-air turbine of the AWE system should be investigated as mentioned earlier. Dijkstra [27] presents a comprehensive investigation into the aeroacoustic performance of a standard axial wind turbine. The research employs an optimization framework for airfoil parameterization, with a cost function based on aerodynamic performance and noise emissions. For aeroacoustic noise prediction, tonal noise was not included or modeled at all. The focus was only on the broadband component, which was investigated using the Brooks-Pope-Marcolini model [50] from 1989 and the TNO model [51] from 1998. Surprisingly, even though it is older, the BPM model proves to be significantly more accurate in predicting the broadband noise from an axial wind turbine.

Using a similar methodology to that of Dijkstra, Van Den Kieboom [17] investigated the aerodynamics and noise emissions of a ram-air turbine intended for AWES. The research uses the Books-Pope-Marcolini (BPM) method and incorporates Hanson's analytical model [52] to predict and evaluate the turbine's noise emissions, excluding the mounting shroud. These methods are applied to assess the contribution of not only broadband noise, as in Dijkstra's work, but also tonal noise generated by the turbine blades. The aerodynamics are derived with Blade Momentum Element Theory (BEMT) and Lifting Line (LL). Using the predictive models and an optimization process, an airfoil shape is selected for the blades by balancing aerodynamic performance with noise reduction strategies. A prototype is built based on the results and tested in a wind tunnel to validate the prediction code. Although the experimental results follow the same trend as the predictive model, the measured values are significantly higher. Van Den Kieboom concludes that this discrepancy

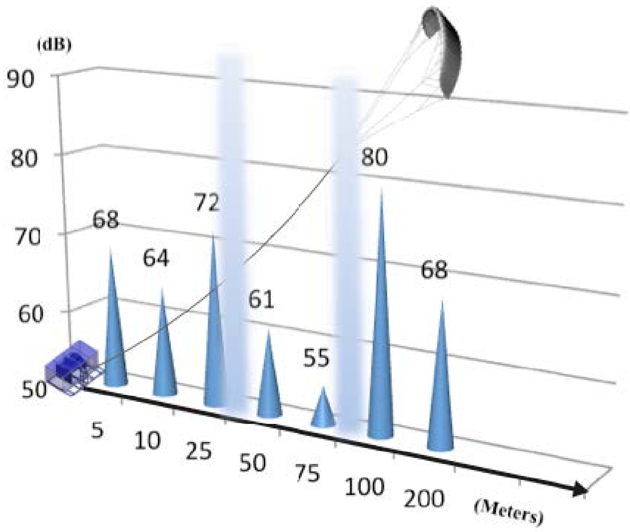

Figure 3.2: SPL values at different distances from the ground station. Retrieved from Szücs [47].

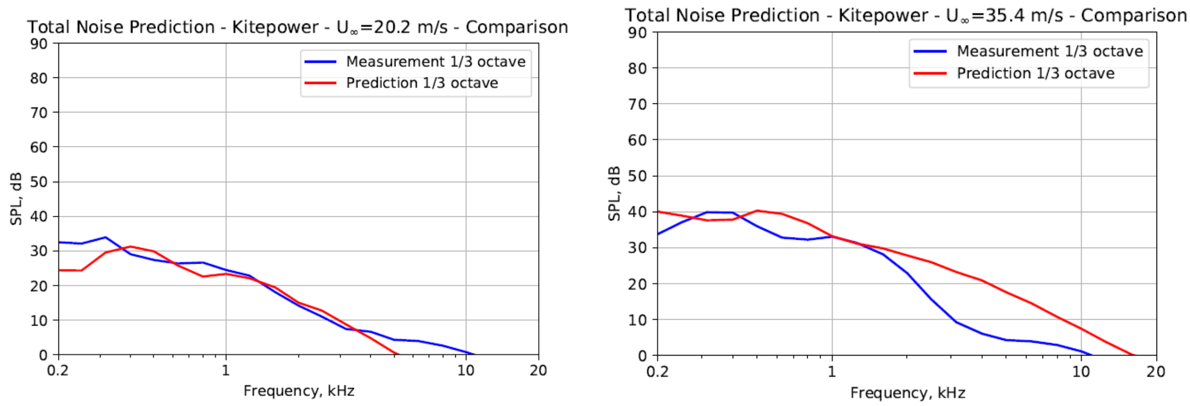

Figure 3.3: Measurement data versus prediction data for the AWE system of Kitepower at $U_\infty = 20.2m/s$ (left) and $U_\infty = 35.4m/s$ (right). Retrieved from Bouman [12].

is primarily due to the quality of the measurements, as the wind tunnel produced substantial background noise that could not be filtered out. Because of this, there is no conclusion about the accuracy of the models used for sound production.

The primary objective of this research paper is to develop a low-order numerical tool for estimating the noise emissions of the entire Kitepower airborne wind energy system. Given the complexity of the kite's aerodynamics, employing frameworks based on computational fluid dynamics (CFD) or computational aeroacoustics (CAA) was deemed beyond the scope of this thesis. The main reason for this decision is the intricate nature of the aerodynamics involved and the challenge of identifying an aeroacoustic model capable of accurately predicting the noise. Consequently, low-fidelity models were chosen due to their advantages of rapid computational results and ease of adjustment when necessary.

This work builds upon the contributions of Szücs [47], Bouman [12], and Van Den Kieboom [17] by enhancing or integrating the analytical and semi-empirical models based on their findings. Notably, two models have demonstrated potential effectiveness for these innovative systems: the BPM model for broadband noises [50] and Hanson's model for tonal noises [53]. Research from several other studies indicates that combining these two models can yield precise outcomes, particularly for propellers in axial flight [54–56]. Subsequent subsections will describe the sound production mechanisms of the Kitepower AWES components and the models employed for their analysis.

3.2. Vortex Shedding Noise from Cylindrical Bodies

When a cylindrical object is exposed to uniform airflow, it can generate a Von Kármán vortex street—a pattern of alternating vortices formed downstream due to flow separation. This phenomenon depends heavily on the Reynolds number (Re) and the geometry of the object. In AWES, tethers and bridle lines are typically flexible, braided textile structures that can stretch and twist, but they are often approximated as circular cylinders for flow analysis. This simplification may become inaccurate when the line deforms into non-cylindrical shapes, such as tapes or twisted segments [10, 14].

For an airborne wind energy system, the Reynolds number can be estimated based on the flight envelope and the dimensions of the lines. Dunker [14] calculated a broad range of possible Reynolds numbers. These were based on a hypothetical AWES, but the same approach will be followed next. For Kitepower, the diameter of the tether and braided lines typically ranges from 2 mm to 14 mm. As flight altitudes are usually below 500 m, atmospheric properties can be considered approximately constant. Although both air density and dynamic viscosity decrease with altitude, the variation in their ratio (kinematic viscosity) is only a few percent.

The apparent flow speed, which should be considered in the calculation, typically ranges between 2.5 m/s and 50 m/s. Different parts of the tether experience different velocities due to their distance from the ground station and varying angles. The Reynolds number for a cylinder is calculated as:

$$Re = \frac{\rho \cdot v_a \cdot D}{\mu} = \frac{v_a \cdot D}{\nu}, \tag{3.1}$$

where ρ is the air density, v_a the apparent speed, μ the dynamic viscosity, and $\nu = \mu/\rho$ the kinematic viscosity. The non-dimensional Reynolds number represents the ratio between inertial and viscous forces acting on the cable. Based on the discussed parameters, the expected Reynolds number range is $332 \leq Re \leq 47380$. In the context of Kitepower, this range falls within the regime of a fully turbulent vortex street, typically observed for $300 < Re_d < 2.9 \cdot 10^5$ [57–59].

The vortex shedding frequency is characterized by the Strouhal number, defined as:

$$St = \frac{f_s \cdot D}{v_a} \quad \Rightarrow \quad f_s = \frac{St \cdot v_a}{D} \tag{3.2}$$

The relationship between the Strouhal and Reynolds numbers is shown in Figure 3.4. According to Goldstein's empirical formula [60], the Strouhal number can be approximated as:

$$St = 0.198\left(1 - \frac{19.7}{Re}\right) \tag{3.3}$$

The typical approximation for vortex shedding around a cylinder is $St \approx 0.2$. Based on the previously calculated Reynolds number for the tether and bridle lines, the Strouhal number falls within the range $0.186 \leq St \leq 0.198$. This closely aligns with the commonly used value in literature and the data presented in Figure 3.4.

Effects of Inclination

The tether of the Kitepower is usually under different angles because of sagging. An inclination of a cylinder relative to the flow direction affects the shedding frequency for small deviations from a perpendicular orientation. According to King [61], the angled shedding frequency can be modeled as:

$$f_s = f_{s,\tau} \sin(\alpha), \quad \text{for } \alpha \geq 60^\circ, \tag{3.4}$$

where $f_{s,\tau}$ is the shedding frequency when the inclination angle α is 90°. Naudascher et al. [62] emphasized that predicting vibration frequencies becomes more complex when $\alpha < 60°$, as the shedding process transitions to a more three-dimensional behavior. Dunker [63] recorded through a series of experiments that the primary vibration frequency under certain conditions was twice the shedding frequency when the Reynolds number was near 300 and the inclination angle α was approximately 76.5°. Furthermore, as the Reynolds number approaches 1000, additional secondary frequencies, occurring at twice the shedding frequency, emerge but remain non-dominant.

As the Strouhal number is calculated based on the flow velocity, this will be influenced as well. Based on the independence principle described in Zdravkovich [64], the updated Strouhal number is presented in Equation 3.5. The decrease in noise generated with inclination and change in shedding frequency with inclination angle was researched experimentally by Latorre Iglesias et al. [65]. In this paper, the cylinder yaw

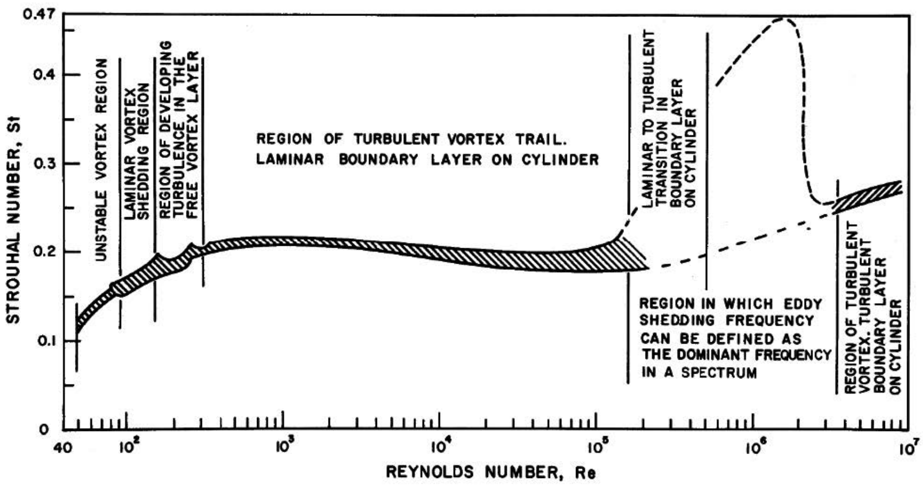

Figure 3.4: Strouhal number as a function of Reynolds number for the shedding producing von Kármán vortex street behind a circular cylinder. Retrieved from Lienhard [57].

angle β is defined differently than the inclination angle α discussed before: a yaw angle of 0° corresponds to a cross flow, whereas at 90° the cylinder is aligned with the flow.

$$St(\alpha) = \frac{f_{s,\tau}\sin(\alpha)\cdot D}{v_a} = \frac{f_{s,\tau}\cos(\beta)\cdot D}{v_a} \tag{3.5}$$

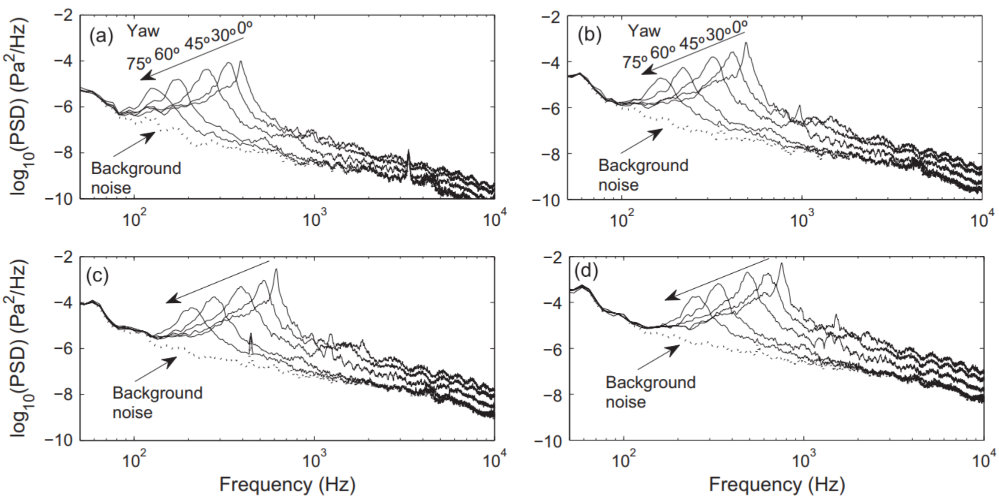

Figure 3.5: Narrow-band PSD spectra emitted by the circular cylinder at various yaw angles and flow speeds, as recorded by microphone without any corrections applied. (a) 25 m/s, (b) 31.5 m/s, (c) 40 m/s, (d) 50 m/s. Retrieved from Latorre Iglesias et al. [65].

3.2.1. Lock-in Behavior

Lock-in behavior is a phenomenon that happens when the vortex shedding frequency becomes close to a natural fundamental frequency of vibration of a structure. When this occurs, the vibrations of the structure become synchronized with the vortex-shedding frequency, amplifying the oscillations and, consequently, the noise generated. Audible tonal noises and whistling for the tether in flight are generally strong indicators of vibration lock-in. Besides louder Aeolian tones generated, these amplified vibrations could also be the cause of material wear and fatigue in certain structures (such as bridges, chimneys, or electrical cables). This can be very dangerous if not mitigated, and it can cause catastrophic failure.

The tether under tension in an AWES can be approximated as a string, although it is not fixed on both ends. However, due to the high tension and relatively large mass of the kite, it could be considered an end-

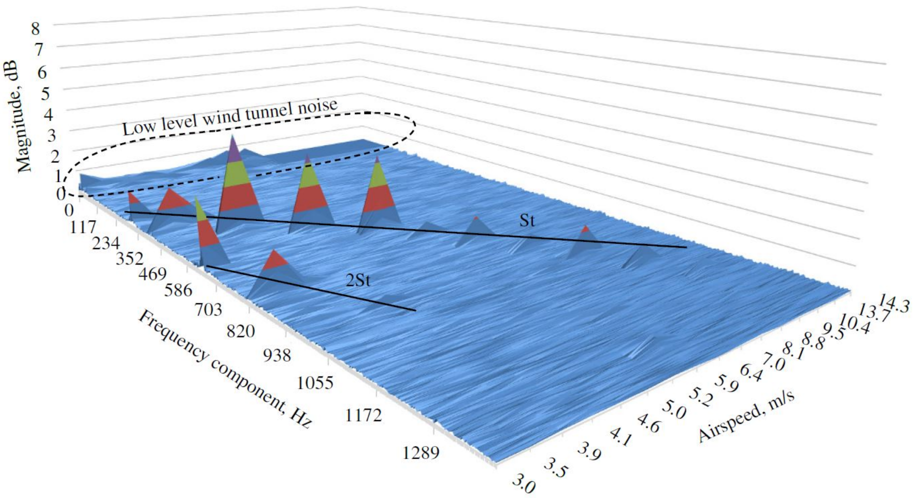

Figure 3.6: Vibration spectrum landscape of a cylindrical line. Retrieved from Dunker [63].

point. The natural frequencies of an elastic string are multiples of the fundamental frequency, formulated as:

$$f_n = \frac{n}{2l_t}\sqrt{\frac{F_t}{\lambda}} \tag{3.6}$$

where n is a positive integer representing the node number, l_t is the length of the string, F_t is the tensile force, and λ is the mass per unit length. Based on Dunker [14], a common range in which a tether would be prone to the lock-in phenomenon is around $0.7f_s < f_n < 1.3f_s$.

Dunker [63] conducted a series of experiments with different tether lines (from cylindrical to braided ones) in order to investigate the lock-in mechanisms. In the paper, a set-up is created that tries to mimic the tension of kite-boarding lines. Therefore, only one end is fixed in place, while the other one is tensioned by supporting some heavy weights. As discussed before, this is very similar to the scenario found in AWES. Dunker discovered that even at small airspeeds (thus low Reynold numbers), the lock-in is present and has a direct correspondence with the Strouhal number. Moreover, in some cases, a secondary vibration frequency was observed, corresponding to twice the shedding frequency. This trend is presented in Figure 3.6.

Figure 3.7 presents the dominant vibration frequencies of a Dyneema® line similar to a bridle line used by Kitepower. The line was tested initially with a pluck test and it was observed that the fundamental frequency was around $f_1 = 84Hz$. The lock-in can be seen best occurring at the frequencies of 408 and 665 Hz, where one vibration condition was observed across a velocity range. It can be seen that the lock-in happens on either side of the stationary shedding frequency, as mentioned before. From the same laboratory experiments, in certain regimes, it was observed the drag forces to be over 300%, attributed to the vortex induced vibrations (VIV) during lock-in. Therefore, it is important to find ways of mitigating this phenomenon.

MECHANISMS TO ATTENUATE VIBRATION AND REDUCE DRAG

In another study, Saur et al. [66] performed a series of experiments for braided lines with different cross-sections and under different tension forces. Figure 3.8 presents all the types of tether lines used in the set-up. It was concluded that greater surface roughness increases sound radiation, while the tension has negligible effects. Moreover, it was found that with a simple protrusion, such as a single-helix-shaped one, the total radiated sound pressure level can be reduced by up to 9 dB. For decreasing AOA, the noise suppression effect of helical surface protrusions and helical line shape is significantly reduced. As the aerodynamic forces and the noise are related, it was found that the drag force is reduced by up to 20%, and the improvement was attributed to the reduced susceptibility to VIV. Another mitigation method comes from Jung [67] that has shown that a latex coating over rope braids for helicopters consistently reduces the drag coefficient by 15% to 50%. However, these solutions might be difficult to implement as the shape of the tether will influence how the tether will sit on the drum or the pulleys.

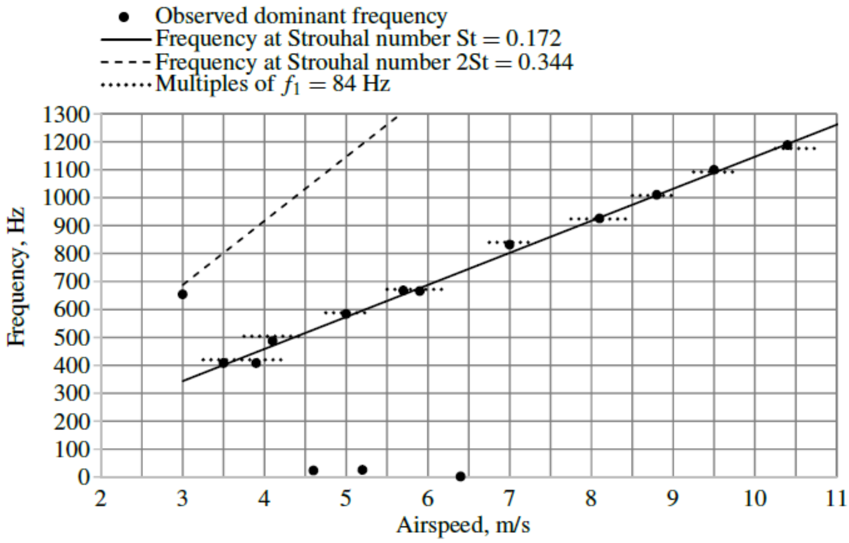

Figure 3.7: Dominant vibration frequencies and lock-in for a line with a diameter of 1.5 mm and $\alpha = 76.5°$ at Re = 300 to 1000. Retrieved from Dunker [63].

Image		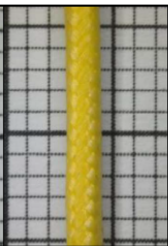			
Name	**Ref 2**	**Ref 3**	**Helix A**	**Helix B**	**Helix C**
Average Diameter	3.3 mm	1.65 mm	1.85 mm	1.87 mm	1.87 mm
Material, Construction	HMPE yarn core with 32 HMPE carrier sheath	HMPE yarn core with 16 HMPE carrier sheath	HMPE yarn core with 16 HMPE carrier sheath	HMPE yarn core with 16 HMPE carrier sheath	HMPE yarn core with 16 HMPE carrier sheath
Helix Design	-	-	1 start; pitch λ = 2D height h = 0.1D	1 wide start; pitch λ = 2D height h = 0.1D	2 start; pitch λ = 2D height h = 0.1D
Cross section	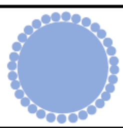	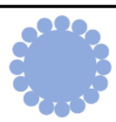	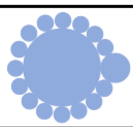	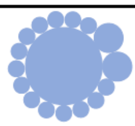	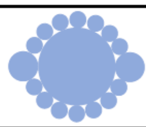

Figure 3.8: Different types of braided lines used in the experiment by Dunker. Retrieved from Saur et al. [66].

3.3. AIRFOIL SELF-NOISES - BROADBAND CONTRIBUTION

Airfoil self-noise refers to the sounds generated by the interaction between an airfoil and the instabilities in the boundary layer. One of the most well-known and comprehensive studies in this field was conducted by Brooks, Pope, and Marcolini, who developed the acoustic BPM model [50]. In their research, they utilized an anechoic wind tunnel at NASA to conduct experiments predominantly with the NACA0012 airfoil. Through various testing configurations and thorough data analysis, they established a semi-empirical scaling formulation that encapsulates the five dominant noise sources associated with the airfoil:

- Turbulent Boundary Layer-Trailing Edge Noise (TBL-TE): This noise arises from the interaction of a turbulent boundary layer with the trailing edge of the airfoil. The boundary layer's characteristics, such as roughness and Reynolds number, influence the intensity of this noise.

- Separation-Stall Noise (S-S): This noise occurs when the flow separates from the airfoil's surface at higher angles of attack. Separation eddies form on the suction side, leading to increased noise levels.
- Laminar Boundary Layer-Vortex Shedding Noise (LBL-VS): This noise is generated by the periodic shedding of vortices from the trailing edge of an airfoil with a laminar boundary layer
- Trailing Edge Bluntness Noise (TEB): The bluntness of the trailing edge can contribute to noise generation due to pressure fluctuation, emitting especially towards higher frequencies.
- Tip Vortex Formation Noise (TV): For airfoils with a finite span compared to the wind tunnel test set-up, tip vortices can form at the wingtips, generating noise.

The following subsections will investigate each of the 5 noise mechanisms and discuss how to determine their contribution.

TURBULENT BOUNDARY LAYER - TBL-TE AND S-S

As the flow progresses over an airfoil surface, a boundary layer will develop on it. The boundary layer will start laminar at the leading edge (LE). However, depending on the Reynolds number, angle of attack, and airfoil geometry, it can transition from laminar to turbulent at a certain chordwise position. These turbulences in the boundary layer induce a fluctuating pressure field, which in turn will generate noise. At lower Mach numbers, the turbulent eddies are not very efficient sound sources [27]. However, when the eddies arrive at a discontinuity such as the trailing edge (TE), the pressure and suction side interact and can produce a loud swishing sound. This mechanism is presented in Figure 3.9.

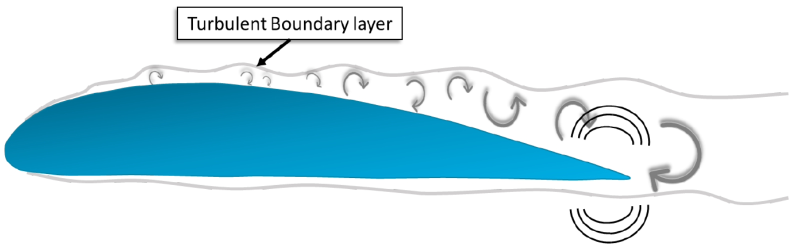

Figure 3.9: Depiction of turbulent trailing edge noise. Retrieved from Van Den Kieboom [17].

The model considers three contributions for the overall TBL-TE noise and these are: the suction side noise SPL_s, the pressure side noise SPL_p, and the separation stall noise depending on the angle of attack SPL_α. In regimes with high angles of attack, the flow can completely separate on the suction side, as can be seen in Figure 3.10. This will form large eddies and extra noise. At the point where the airfoil is completely stalled, the separation-stall noise will become dominant.

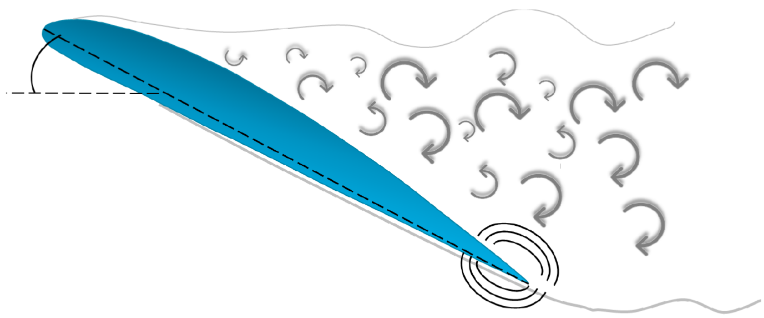

Figure 3.10: Depiction of deep stall of an airfoil, which causes separation-stall noise. Retrieved from Van Den Kieboom [17].

Considering all the components of the TBL-TE noise, the total contribution can be summed as:

$$SPL_{TBL-TE} = 10\log_{10}\left(10^{\frac{SPL_S}{10}} + 10^{\frac{SPL_P}{10}} + 10^{\frac{SPL_\alpha}{10}}\right) \tag{3.7}$$

Based on the experimental data, the BPM model incorporates scaling factors for each of the aforementioned noise contributions. These scaling factors primarily depend on the Strouhal number and the Reynolds number calculated with the chord length. Each contribution can be calculated through the BPM model as follows [50]:

$$SPL_p = 10\log_{10}\left(\frac{\delta_p^* M^5 L \bar{D}_h}{r_e^2}\right) + A\left(\frac{St_p}{St_1}\right) + (K_1 - 3) + \Delta K_1 \tag{3.8}$$

$$SPL_s = 10\log_{10}\left(\frac{\delta_s^* M^5 L \bar{D}_h}{r_e^2}\right) + A\left(\frac{St_s}{St_1}\right) + (K_1 - 3) \tag{3.9}$$

$$SPL_\alpha = 10\log_{10}\left(\frac{\delta_s^* M^5 L \bar{D}_h}{r_e^2}\right) + B\left(\frac{St_s}{St_2}\right) + K_2 \tag{3.10}$$

where δ^* represents the boundary layer displacement thickness on the suction or pressure side, while St denotes the Strouhal number calculated based on δ^*. The Mach number is given by M, L represents the blade length, and r_e is the effective distance between the source and the observer. The term $\bar{D}_h$ denotes the directivity function for higher frequencies. The remaining variables, A, B, K_1, and K_2, are scaling factors dependent on the Strouhal or Reynolds number derived empirically.

It is evident that sound pressure levels are strongly influenced by flight speed, as the Mach number appears with an exponent of 5. Additionally, boundary layer parameters play a crucial role in the calculations, along with the observer's distance from the source. When the AoA surpasses the stall angle, the airfoil is considered in deep stall, and the separation-stall noise becomes dominant. At this point, the suction and pressure side noises can be neglected and are equal to $-\infty$. The contribution from the angle of attack becomes:

$$SPL_\alpha = 10\log_{10}\left(\frac{\delta_s^* M^5 L \bar{D}_l}{r_e^2}\right) + A'\left(\frac{St_s}{St_2}\right) + K_2, \tag{3.11}$$

where the main change comes from the directivity $\bar{D}_l$ for low frequencies and a different shape function A'.

LAMINAR BOUNDARY LAYER-VORTEX SHEDDING NOISE (LBL-VS)

Not only the turbulent boundary layer can generate noise, but also the laminar one. Depending on the radius and shape of the airfoil, some sections of it might present mostly a laminar boundary layer on any of the pressure or suction side. Because of a resonant interaction between the unsteady laminar-turbulent transition, some small instabilities can occur. If they interact with the TE, tonal noise or a narrow band distributed noise is generated. The equation for calculating the LBL-VS is as follows:

$$SPL_{LBL-VS} = 10\log_{10}\left(\frac{\delta_p M^5 L \bar{D}_h}{r_e^2}\right) + G_1\left(\frac{St}{St'_{peak}}\right) + G_2\left(\frac{R_c}{(R_c)_0}\right) + G_3(\alpha), \tag{3.12}$$

where the boundary layer thickness δ_p is used for scaling compared to the TBL-TE. The other parameters are shape functions that depend on the Strouhal number for G_1, the Reynolds number for G_2, and the angle of attack for G_3.

Figure 3.11: Depiction of vortex shedding for laminar boundary layer. Retrieved from Van Den Kieboom [17].

TRAILING EDGE BLUNTNESS NOISE (TEB)

Trailing edge vortex shedding noise occurs when the edge is sufficiently blunt compared to the boundary layer thickness, leading to the periodic shedding of vortices as shown in Figure 3.12. This process can generate narrowband noise with tonal peaks, with its frequency and amplitude largely dictated by the shape of the trailing edge. The formulation for the TEB is:

$$SPL_{TEB} = 10\log_{10}\left(\frac{hM^{5.5}L\bar{D}_h}{r_e^2}\right) + G_4\left(\frac{h}{\delta^*_{avg}},\Psi\right) + G_5\left(\frac{h}{\delta^*_{avg}},\Psi,\frac{St'''}{St'''_{peak}}\right) \tag{3.13}$$

Important factors influencing this noise include the average displacement thickness of the boundary layer on both sides of the airfoil (δ^*_{avg}), the height of the trailing edge (h), and the angle (Ψ) between the suction and pressure surfaces. The ratio of trailing edge thickness to boundary layer thickness (h/δ^*_{avg}) plays a crucial role, as higher values make the noise more tonal by narrowing its bandwidth. Moreover, G_4 and G_5, which are empirical functions, and the peak Strouhal number are all calculated using this ratio. However, it is considered that the shedding frequency increases with lowering the trailing edge-thickness [68]. A well-known way to mitigate this effect is by sharpening the trailing edge, which increases the vortex shedding frequency and moves the noise into the ultrasound range, making it less perceptible to human ears [17].

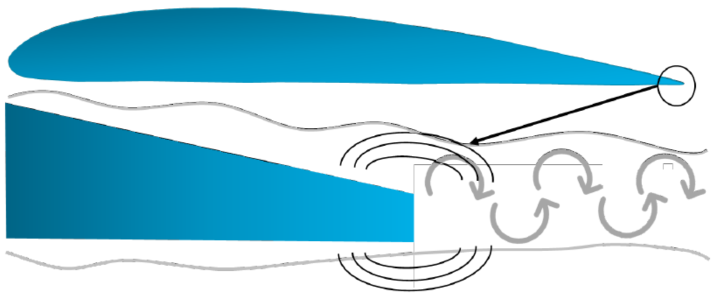

Figure 3.12: Depiction of the fluctuating flow pattern at a blunt trailing edge. Retrieved from Van Den Kieboom [17].

Vortex shedding can also lead to asymmetric flow patterns around the airfoil, forming a von Kármán vortex street that alters the pressure distribution and enhances surface pressure fluctuations near the trailing edge [27]. Blake [68] suggests that if the bluntness ratio remains below a threshold (0.05–0.3), vortex shedding tones do not develop, but once it exceeds 0.3, the geometry of the edge becomes the dominant factor in noise generation. These findings highlight how modifying the trailing edge shape is an effective strategy for reducing airfoil self-noise.

TIP VORTEX FORMATION NOISE (TV)

Brooks, Pope, and Marcolini performed experiments with finite and so-called infinite wings in the wind tunnel. They concluded that with the finite wings where circulation is present, there appears to be an additional noise mechanism. It is generated due to a cross-flow over the tip which creates perturbation in the pressure field of the suction or pressure side. The vortex created by this pressure difference has a highly turbulent core that interacts with the trailing edge in a manner similar to TBL-TE noise created through boundary layer turbulences [50]. Figure 3.13 presents this tip noise generation. Thus, minimizing tip noise primarily depends on optimizing the tip shape design. TV noise occurs exclusively at the blade's tip, where the outer region contributing to the noise is defined by the viscous core size (l). Its prediction can be determined using:

$$SPL_{TV} = 10\log_{10}\left(\frac{M^2M^3_{max}l^2\bar{D}_h}{r_e^2}\right) - 30.5\left(\log_{10}(St'')+0.3\right)^2 + 126 \tag{3.14}$$

TOTAL NOISE

While analyzing SPL from individual noise sources or blade sections is valuable, the primary goal is to determine the total SPL at a specific observer location. Notably, the BPM model computes noise 1 meter behind the rotor center and adjusts SPL values for each blade section based on directivity patterns. Therefore, it is

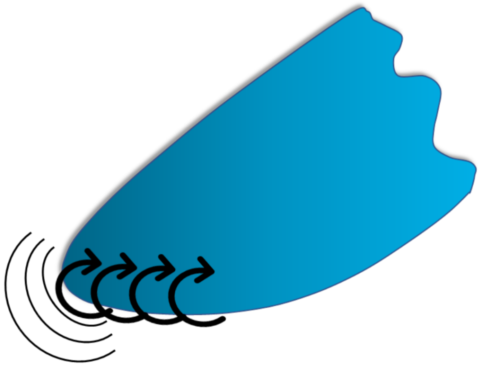

Figure 3.13: Depiction of the circulation generating tip vortex noise. Retrieved from Van Den Kieboom [17].

as the noise source is 1 meter behind the trailing edge. To obtain the total noise level, SPL values from all sources are first converted to pressure, summed, and then transformed back into dB. Finally, the total noise contribution from a single blade is scaled by the number of blades to determine the overall SPL, as outlined in the model. The summation of the contribution is as follows:

$$SPL_{total} = 10\log_{10}\left(10^{\frac{SPL_{TBL-TE}}{10}} + 10^{\frac{SPL_{LBL-VS}}{10}} + 10^{\frac{SPL_{TEB}}{10}} + 10^{\frac{SPL_{TV}}{10}}\right) \tag{3.15}$$

3.4. AIRFOIL HARMONIC NOISES - TONAL CONTRIBUTION

One widely used method for modeling harmonic propeller noise in the frequency domain is Hanson's far-field acoustic model [52]. Known as the Helicoidal Surface Theory [53], it accounts for blade thickness, surface loading, and the effects of forward flight, including Doppler shifts, which vary with observer position.

Hanson's model represents the blade as moving on a helicoidal surface, which rotates at constant angular velocity while advancing at flight speed. The angle of attack is defined relative to this surface, allowing frequency-domain prediction of blade loading. The method is based on Goldstein's acoustic analogy for moving surfaces [69], which builds on the Ffowcs Williams and Hawkings (FW-H) formulation [70].

The theory simplifies the FW-H equations by assuming source strengths act on the mean blade surface, consistent with thin wing theory. This results in a mathematical formulation describing steady thickness and loading noise under axial inflow. Quadrupole sources, which arise at high Mach numbers, are neglected since AWES operates at low Mach numbers and with distant observers, where such sources decay rapidly.

The acoustic pressure in the far-field can be represented as a sum over harmonics of the blade passing frequency (BPF) using the following expression:

$$p(t) = \sum_{m=-\infty}^{\infty} P_{mB}\, e^{-imB\Omega_D t} = 2\,\mathrm{Re}\left[\sum_{m=1}^{\infty} P_{mB}\, e^{-imB\Omega_D t}\right] \tag{3.16}$$

where P_{mB} is the Fourier transform of the acoustic pressure for the m-th harmonic of the BPF, B is the number of blades, and Ω_D is the angular velocity, incorporating the Doppler effect.

At the time of noise emission, the observer is at a radial distance r from the source under the angle θ, but the reception occurs when the source has already moved to a visual position at θ_1, as illustrated in Figure 3.14. This shift in position is influenced by the flight speed, which is why the Mach number M_x appears in the expression for Ω_D.

The term P_{mB} includes the acoustic pressure produced by the thickness and loading noises. Thickness noise and loading noise are fundamental phenomena governed by linear aerodynamic theory. Thickness noise occurs as a result of the volume displacement of the fluid caused by the rotor blades. On the other hand, loading noise originates from the steady aerodynamic forces exerted on the blade surfaces while in motion. Therefore, the term P_{mB} can be decomposed into three distinct components:

- P_{Vm}: The volume displacement monopole contribution.
- P_{Dm}: The drag dipole contribution.
- P_{Lm}: The lift dipole contribution.

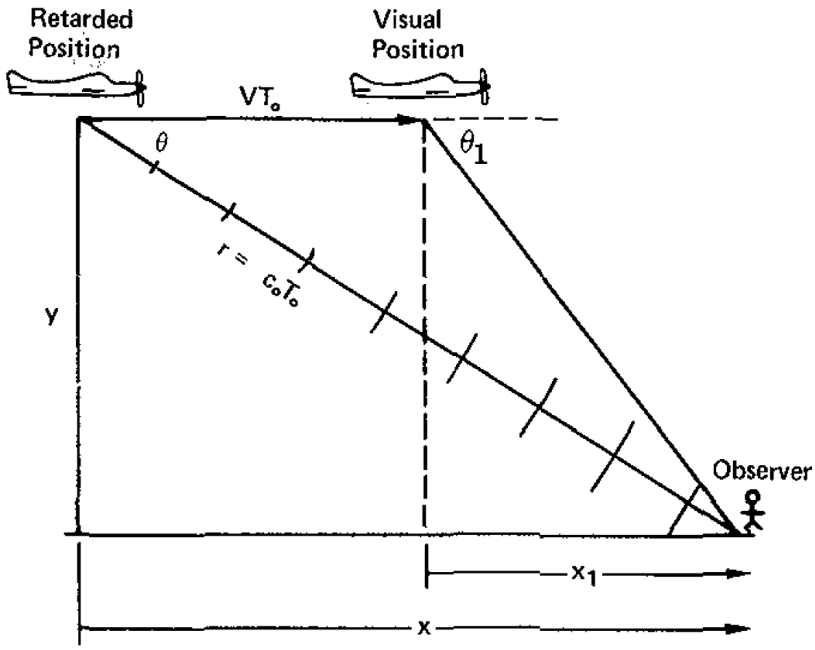

Figure 3.14: Relationship between the retarded angle θ and visual angle for an observer at distance r. Retrieved from Magliozzi et al. [32]

The value of P_{mB} is determined by summing these components, as expressed by $P_{mB} = P_{Vm} + P_{Dm} + P_{Lm}$. These noise-generating components are computed using the following expressions:

$$\begin{bmatrix} P_{Vm} \\ P_{Dm} \\ P_{Lm} \end{bmatrix} = -\frac{\rho_0 c_0^2 B \sin\theta \, e^{i mB\left(\frac{\Omega_D r}{c_0} - \frac{\pi}{2}\right)}}{8\pi \frac{y}{D}(1 - M_x \cos\theta)} \int M_r^2 e^{i(\phi_0 + \phi_s)} J_{mB}\left(\frac{mBzM_T \sin\theta}{1 - M_x \cos\theta}\right) \begin{bmatrix} k_x^2 t_b \Psi_V(k_x) \\ i k_x (C_D/2) \Psi_D(k_x) \\ -i k_y (C_L/2) \Psi_L(k_x) \end{bmatrix} dz \tag{3.17}$$

where m represents the harmonic number, and B is the number of blades. The terms ϕ_0 and ϕ_s are phase lags, while the k-parameters denote non-dimensional wavenumbers that influence the loading and thickness distributions, represented by the functions Ψ. The aerodynamic characteristics required for computing the drag and lift components are described by the coefficients C_L and C_D, corresponding to lift and drag, respectively.

Before noise calculations can be performed, the blade geometry must be defined as a function of the radius ratio $z = r_z / r_t$, where r_t is the tip radius and r_z is the radial location of interest along the blade (from hub to tip). The tip rotational Mach number is denoted by M_T, while the section-relative Mach number M_r varies with z and is computed using:

$$M_r = \sqrt{M_x^2 + z^2 M_T^2}, \tag{3.18}$$

All other geometric properties are illustrated in Figure 3.15, including the spanwise chord distribution b, the sweep defined by the ratio of mid-chord alignment (MCA) to diameter, and the normalized thickness distribution $H(x)$. A more detailed description of these parameters can be found in Hanson's paper [53].

Another important parameter in Hanson's harmonic noise model is the Bessel function J_{mB}, which acts as a radiation efficiency factor and can often be tuned for specific propeller designs. This function peaks at orders where $mB \neq 0$, approaches zero for small arguments, and exhibits oscillatory behavior for large arguments. The behavior of J_{mB} for various orders and arguments is illustrated in Figure 3.17.

The function $H(x)$ represents the previously described chordwise thickness distribution, while $f_D(x)$ and $f_L(x)$ denote the chordwise distributions of drag and lift, respectively. Typical examples of these normalized distributions are shown in Figure 3.16. These shape functions are first integrated from the leading edge to the trailing edge, and then over the entire propeller radius to determine their overall contribution.

By calculating all the necessary variables, the acoustic pressure can be calculated. This is done by summing only the real part of the Fourier coefficients. Afterwards, the result must be multiplied by two, as only the positive harmonic numbers are considered.

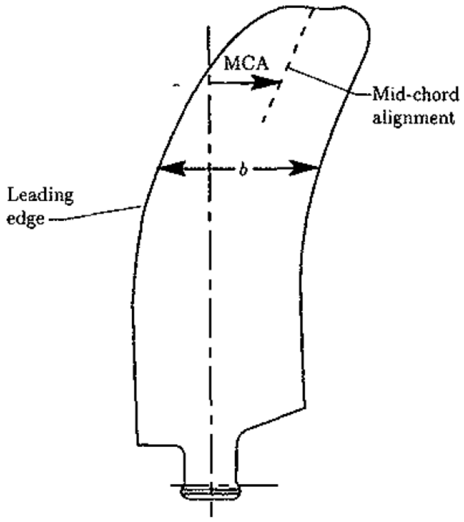

(a) Blade planform showing the chord b and sweep as function of radius ratio z.

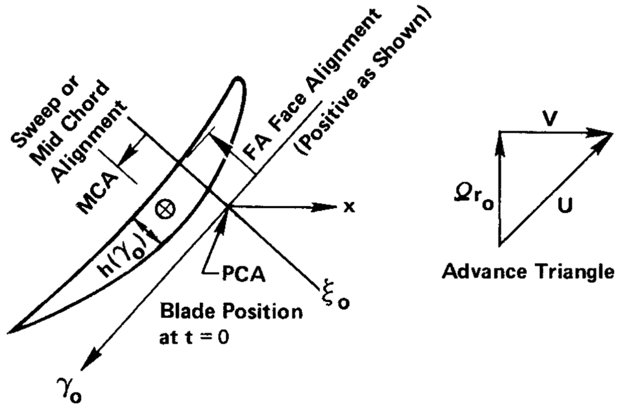

(b) Blade element shown in helical coordinates, defining the mid-chord alignment and face alignment.

Figure 3.15: Example of blade geometric properties. Retrieved from Hanson [53].

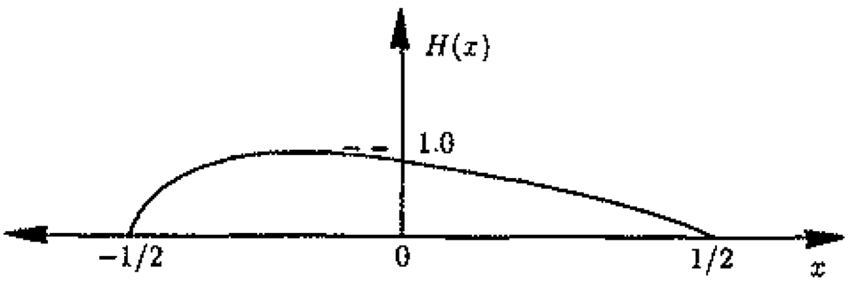

(a) Chordwise distribution of the thickness shape functions.

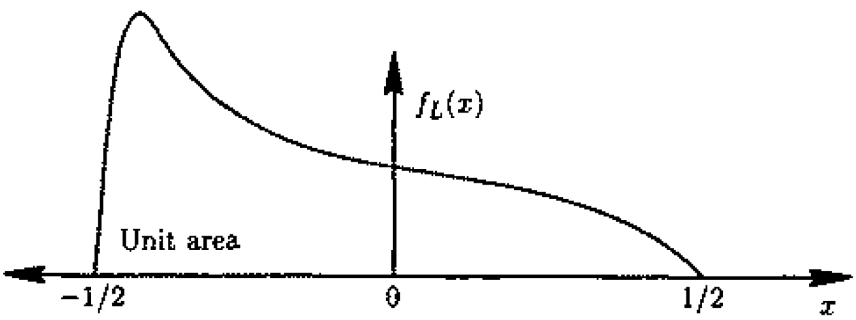

(b) Chordwise distribution of the lift shape functions.

Figure 3.16: Example of blade shape functions for thickness and loading. Retrieved from Magliozzi et al. [32].

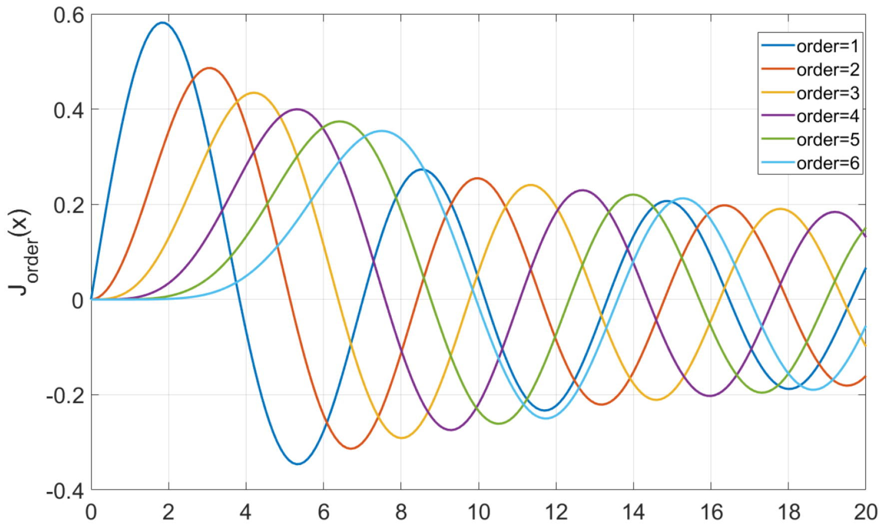

Figure 3.17: Bessel function for different orders and arguments. Retrieved from Haddaoui [33].

4

Problem Statement

4.1. Research Question

This thesis aims to bridge the gap between established theoretical noise models and their application to airborne wind energy systems by adapting these models for the Kitepower configuration and validating them using flight test data and audio recordings.

The **main research question** guiding this work is therefore formulated as follows:

> *How accurately can existing aeroacoustic models capture and represent the physical mechanisms underlying noise generation of the airborne wind energy system developed by Kitepower?*

This question focuses on the adaptation and evaluation of established aeroacoustic prediction models and their physical formulations, aiming to assess their applicability for airborne wind energy systems. The goal is to balance computational efficiency with predictive accuracy, and to validate the framework using component and flight data from the Kitepower system.

To support the investigation of this main question, the following *sub-questions* are addressed:

- What are the dominant noise generation mechanisms of the components in airborne wind energy systems, and how can they be modeled using low-fidelity analytical or semi-empirical approaches?
- How can the geometric data from the kite and turbine be used in combination with aerodynamic solvers to generate reliable and realistic input parameters for noise prediction?
- How do the predicted noise results from the framework compare with experimental measurements, and what limitations affect the agreement between them?

Together, these questions define the scope of the research and lay the foundation for the development, validation, and evaluation of the proposed aeroacoustic prediction framework presented in the following chapters.

4.2. Research Objectives

This thesis aims to develop a computationally efficient framework for predicting the noise generated by airborne wind energy systems. The focus is on the Kitepower system, which includes a Leading Edge Inflatable (LEI) kite, an onboard ram-air turbine, tether, and bridle lines. The research seeks to assess whether established aeroacoustic models can be effectively used to predict the noise generated by these components. By applying these models to the Kitepower configuration and comparing their output to audio recordings from flight tests, the goal is to evaluate the accuracy and practical applicability of low-fidelity, physics-based prediction methods.

To achieve this, the work is guided by the following core objectives:

- To extract accurate geometric data from 3D CAD models of the kite and turbine and use aerodynamic solvers to derive key parameters such as blade loading distributions and boundary layer properties.
- To implement analytical or empirical models capable of estimating both broadband and tonal noise contributions from the kite, bridle lines, tether, and ram-air turbine, based on established aeroacoustic theory.
- To incorporate flight data into the framework by processing onboard sensor measurements, allowing for dynamic simulation of noise generation throughout all phases of flight.
- To evaluate the model's accuracy by comparing its predicted acoustic spectra with audio recordings captured during test flights.
- To evaluate the framework's strengths and limitations in isolating dominant noise sources and assess its suitability for future integration in psychoacoustic research, regulatory assessments, and component-level noise reduction strategies.

Achieving these objectives will result in a versatile prediction tool that supports early-stage design and analysis of AWES, enhances the understanding of their acoustic behavior in real operational conditions, and facilitates future research in multiple areas.

II

Methodology

5

Aeroacoustic Prediction Model

The prediction model for the aeroacoustic noise generated by the Airborne Wind Energy System (AWES) is built upon a multi-step computational framework. An overview of the complete structure of the prediction process is provided in Figure 5.1. This framework requires a range of inputs related to component geometries, flight dynamics, and aerodynamic properties, each of which can vary significantly depending on the specific flight phase and conditions at a given moment.

This chapter focuses on detailing the Aeroacoustic Prediction Model, covering not only the specific models used for each sound-generating source, but also the investigation of propagation effects considered from the source to the observer. The objective is to construct a physical representation that closely approximates how an observer would actually perceive the noise produced by the system during flight.

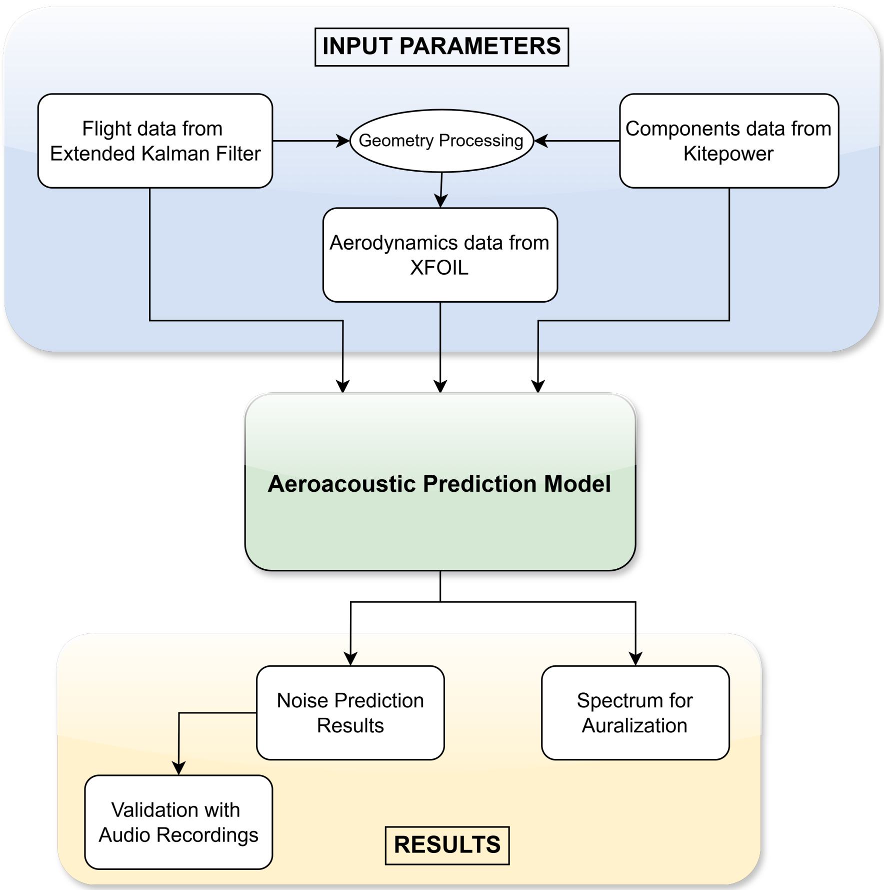

Figure 5.1: Complete schematic layout of the low-fidelity Aeroacoustic Prediction Framework.

As highlighted previously, the most critical components from an aeroacoustic standpoint are the kite itself, the ram-air turbine, the tether, and the bridle lines. The geometrical and aerodynamic characteristics of these components play a key role in noise generation. For relatively simple components such as the tether and bridle lines, basic dimensional parameters are sufficient. In contrast, the airfoil shape and other geometrical properties for the turbine blades and the kite were obtained from 3D CAD models. All the necessary data was obtained directly from Kitepower and subsequently processed to extract the relevant input parameters. The data extraction and pre-processing methods are described in detail in Chapter 6.

To achieve an accurate representation of the system's flight dynamics, the Extended Kalman Filter (EKF) from Cayon et al. [71] was utilized. Their work presents an iterated EKF-based sensor fusion technique capable of estimating the critical state variables of AWESs. This method integrates diverse sensor data, including position, velocity, tether force, and reel-out measurements, to produce reliable estimations of the system dynamics. From this, essential parameters such as the kite's angle of attack (AoA), apparent wind speed, elevation angle, tether length, and many more can be extracted at specific flight instances.

Depending on the flight properties derived from the EKF, certain aerodynamics properties are required for predicting the noise of the components. Parameters such as boundary layer thickness or displacement, lift coefficient, and drag coefficient are necessary inputs. As the flight properties are changing rapidly, it was opted for a fast solver that could provide some estimations of these parameters with an acceptable level of accuracy. Due to the need for quick computations with reasonable accuracy, high-fidelity CFD solvers were ruled out owing to their computational cost and complexity for automation. Instead, the low-fidelity tool, XFOIL [72], was selected for its balance of speed and accuracy. XFOIL's panel method and boundary layer modeling capabilities have previously been employed by Bouman [12], showing satisfactory results for a low-order aeroacoustic analysis. These steps are dicussed in Chapter 7.

The compiled data serves as the foundation for the Aeroacoustic Noise Prediction Model. Aerodynamic results from XFOIL, flight data from the Extended Kalman Filter (EKF), and detailed geometrical properties provided by Kitepower are all integrated into the framework to form the input set for the simulation. The structure of the model, which is introduced in this chapter, uses these inputs to generate individual noise predictions for each component of the system. These component-level outputs are then combined and passed through propagation and attenuation models to calculate the total noise perceived by an observer at a specified location. The final predictions are validated using flight audio recordings, as discussed in Chapter 9.3.

Additionally, when multiple sound spectra are computed at short time intervals, they can be processed and used for auralization. Auralization is the process of creating audible sound files from computer-generated data, simulating how sound behaves in a specific environment. It's akin to acoustic virtual reality, allowing listeners to hear how a space or product will sound [35]. Auralization allows for immersive acoustic simulations, enabling one to experience how the AWES would sound under various operational conditions.

In summary, the procedures outlined above define the entire framework for predicting the noise emissions of an AWES. Each step will be explored in greater detail in the following chapters.

5.1. Prediction Model for Tether and Bridle Line Noise

The tether and bridle lines of the Kitepower system are constructed from Dyneema® braided lines. While their cross-sectional shape is not perfectly circular, they can be reasonably approximated as cylindrical bodies. The methodology for determining the vortex-shedding frequency associated with the von Kármán vortex street behind a circular cylinder was previously discussed in Section 3.2. It was noted that the inclination angle of the cylinder affects both the amplitude and frequency of the emitted noise due to the independence principle related to the velocity component normal to the cylinder axis. The next step involves identifying a suitable estimation model for the pressure fluctuations induced by vortex shedding around cylindrical structures.

Curle [73] demonstrated that the sound emitted from an 'acoustically compact' solid surface with fluctuating force F_i can be expressed with the sound pressure $p(r,t)$ as:

$$p(r,t) = \frac{1}{4\pi c_0}\frac{r_i}{r^2}\frac{\partial F_i\left(t-\frac{r}{c_0}\right)}{\partial t}, \tag{5.1}$$

where c_0 is the speed of sound in the medium and r is the distance between the center of the source and the observer. By definition, an 'acoustically compact' surface implies that the wavelength radiated by the surface should be larger than the characteristic dimensions of the body in question [74]. For the generation of the Aeolian tone, only the fluctuating lift force needs to be considered based on Fujita [75].

Therefore, F_i can be replaced by the lift force, which depends on the diameter of the cylinder d, its length l, the apparent wind speed v_a, and the fluctuating lift coefficient $C_L(t)$, as:

$$F_i(t) = \frac{1}{2}\rho_0 v_a^2\, d\, l\, C_L(t) \tag{5.2}$$

A usual simplification implies that the lift fluctuation is sinusoidal, and the time derivative of $C_L(t)$ can be expressed under the form:

$$\frac{\partial C_L(t)}{\partial t} = \omega\, C_L(t), \tag{5.3}$$

with ω being the angular frequency of the fluctuation.

This frequency can be derived through the formula of the Strouhal number, and it becomes:

$$\omega = 2\pi \frac{v_a St}{d}. \tag{5.4}$$

For calculating the sound pressure, the time derivative of the fluctuating force F_i is of interest. By substituting all of the above, we obtain:

$$\frac{\partial F_i(t)}{\partial t} = \pi \rho_0 v_a^3\, l\, St\, C_L(t) \tag{5.5}$$

Finally, the mean square sound pressure can be calculated by substituting the Equation 5.5 in Equation 5.1. A more general form is presented in Latorre Iglesias et al. [65] that takes into account propagation effects:

$$\overline{p^2(r)} = \frac{\rho_0^2 v_a^6 St^2\, l\, l_C\, C_{L,RMS}^2}{16 c_0^2\, r^2} \frac{D_{rad}(\Psi)}{(1 - M\cos\phi)^4}, \tag{5.6}$$

where $C_{L,RMS}$ is the root-mean-square of the lift coefficient fluctuation, and l_C is the correlation length based on the diameter of the cylinder such that $l_C = m\,d$, where m is a normalization factor. The second fraction has at the numerator the directivity function that becomes $D_{rad}(\Psi) = \cos^2\Psi$ for a theoretical dipole, and at the denominator the convective amplification factor for a dipole source $(1 - M\cos\phi)^4$ [65]. Radiation angle Ψ is defined as the angle between the observer and the axis of fluctuating lift force (perpendicular to the flow direction), the Mach number is defined as $M = v_a/c_0$, and the angle ϕ is the angle between the direction of the flow and the observer position.

The only step left for calculating the sound pressure level is to find the root-mean-square of the lift coefficient fluctuation and the correlation length. Through a series of experiments and literature review, Norberg [76] described empirical formulations for both the root-mean-square of the lift coefficient fluctuation and the correlation length for the circular cylinders based on Reynolds number. The range which Norberg [76] describes includes Reynolds numbers between $47 \leq Re \leq 3 \cdot 10^5$, which bounds are well containing the ones for the tether or bridle lines in Kitepower system.

Influence of the yaw angle on the sound pressure - As mentioned before, the independence principle [64] is used as an approximation to assess the change of shedding frequency based on the yaw angle β. The incident flow v_a, usually symbolized with U_∞, is decomposed into two perpendicular components. The normal flow speed is simply:

$$v_{a,n} = v_a \cos\beta. \tag{5.7}$$

Feeding this back to Equation 5.6, it can be deduced how the mean-square sound pressure depends on the yaw angle [65]:

$$\overline{p^2(\beta,\mathbf{x})} = \overline{p^2(0,\mathbf{x})}\cos^6\beta \tag{5.8}$$

The sound pressure level can be computed now, and it is:

$$\mathrm{SPL}(r) = 10\log_{10}\left(\frac{\overline{p^2(r)}}{p_0^2}\right) = 10\log_{10}\left(\frac{\rho_0^2 v_a^6 St^2\, l\, l_C\, C_{L,\mathrm{RMS}}^2}{16 c_0^2\, r^2\, p_0^2} \cdot \frac{D_{\mathrm{rad}}(\Psi)\cos^6\beta}{(1 - M\cos\phi)^4}\right) \tag{5.9}$$

The original formula also includes another factor for the near-field contribution, but it was not included here as the observer's position is far from the source. This vortex-shedding noise model for tether and bridle lines was implemented in MATLAB. Its implementation and functionality were verified against experimental data from Latorre Iglesias et al. [65], as presented in Appendix A.

5.1.1. Tether Model

Acoustic modeling of the tether requires knowing its position and apparent velocity, as the shedding frequency and SPL value change depending on these parameters, as shown previously. During the power cycles, the length of the tether changes between a minimum r_{min} and a maximum r_{max} value. The speed and inclination of the tether will differ along its length, based on the kite's flight speed and the tether length. Because of this, the shedding noise will be produced along the tether with different characteristics. Moreover, Dunker [14] even observed that different regions of the tether can exhibit multiple localized lock-in mechanisms, vibrating over a larger spectrum at once. Therefore, it is important to analyze the tether noise by sectioning it to simulate the coexisting noise from every region.

Dunker [14] presents a method for calculating the velocity of the tether based on the kite's velocity, wind speed, and reeling factor. If the tether is considered straight, any point on it can be described by radial coordinates as:

$$\mathbf{r} = r\mathbf{e}_r \tag{5.10}$$

where r is the radial distance and $\mathbf{e}_r$ is the unit vector in radial direction. This can be normalized if the total tether length l_t is known by:

$$R = \frac{r}{l_t}, \text{with } 0 \leq R \leq 1 \tag{5.11}$$

During the power cycle, the value of l_t changes based on the reeling motion, and to a minor degree, due to the strain of the tether. Moreover, it can be considered that the tether and the kite radial velocity dictated by the reeling motion are equal:

$$\mathbf{v}_{t,r} = \mathbf{v}_{k,r}, \text{ for } 0 \leq R \leq 1 \tag{5.12}$$

On the other hand, the tangential velocity for a straight tether increases linearly with the non-dimensional tether coordinate R. At the ground station, the tangential velocity of the tether is zero, while at maximum length l_t, it can be considered to be equal to the tangential velocity of the kite. Substituting everything in Equation 2.1, the apparent wind velocity of a material point on the tether is defined as:

$$\begin{aligned} \mathbf{v}_a &= \mathbf{v}_w - \mathbf{v}_t, \\ &= \mathbf{v}_w - \mathbf{v}_{k,r} - \mathbf{v}_{k,\tau} R, \quad \text{for } 0 \leq R \leq 1. \end{aligned} \tag{5.13}$$

It is important to notice that during reel-out, the approximation of a straight tether is fairly accurate due to the high operating tension [77]. However, the tether generally sags during reel-in, which must be taken into account for accurate noise production. Because of the sag, the incidence angle changes over the length, leading to regions with different shedding behavior. The position of the tether, and especially its inclination angle due to sagging, can be calculated through a model described by the tension in the tether. Breukels [78] presents a model that takes into account the aerodynamic loading and the gravitational forces for calculating the shape of the tether. If the tether force at the kite $\mathbf{T}_K$ is known, the tether force at the ground station $\mathbf{T}_G$ can be derived as:

$$\mathbf{T}_G = -\mathbf{T}_K - \int_0^l \left[\mathbf{q}_g(s) + \mathbf{q}_D(s)\right] ds \tag{5.14}$$

where $\mathbf{q}_g$ is the distributed gravitational force and $\mathbf{q}_D$ is the aerodynamic force along the tether path described by coordinate s. If a stepwise integration is applied with known boundaries, the tether force at the ground station can be calculated, and subsequently, the tension and inclination angle of the tether at any position.

Although the position and velocity of the tether are important parameters in aeroacoustic modeling, the development of a new tether dynamics model is considered beyond the scope of this thesis. Instead, the necessary variables for both the tether and bridle lines are extracted from the Extended Kalman Filter developed by Cayon et al. [71]. Once the total tether length is provided from the EKF, it is discretized into multiple segments of equal length. Knowing the kite's velocity, the velocity of each tether segment is estimated at its midpoint as of Equation 5.13 for use in the prediction code. For the bridle lines, it is assumed that the flow velocity is equivalent to that of the kite and the onboard ram-air turbine.

5.2. ONBOARD RAM-AIR TURBINE NOISES

The onboard ram-air turbine is a crucial component of the AWES, generating the electricity needed to power all onboard electrical motors and sensors. However, it is also a significant source of noise, making it essential to understand the mechanisms behind its noise production thoroughly.

Ram-air turbine noise can be categorized into two types. The first is tonal noise, which is closely linked to the blade passing frequency:

$$BPF = \frac{B \times RPM}{60} = B \times N, \tag{5.15}$$

where B is the number of blades and N is the rotational frequency. The second category is broadband noise, which is spread over a wide range of frequencies. The broadband noises are usually induced by turbulence, which makes them unsteady and random in nature. Due to this complexity, developing predictive models is extremely challenging, and most rely on semi-empirical or fitted data.

As discussed in Chapter 3, the most widely used approach for predicting turbine or propeller noise is a combination of two models: the analytical model by Hanson and the semi-empirical Brooks–Pope–Marcolini (BPM) model [17, 33, 79, 80]. For tonal noise components, Hanson's model [52, 53] has shown high accuracy, particularly for the first few harmonics. It accounts for blade geometry, flight speed, turbine RPM, environmental conditions, and observer position. Based on the flying conditions and the pitch angle of the blade, spanwise and chordwise distributions of lift and drag coefficients must be derived and be used as inputs for the loading of the blade. The aerodynamics coefficients will be derived through XFOIL [72], as will be explained in Section 7.

For the broadband contribution, although more complex and more difficult to quantify, the semi-empirical Brooks-Pope-Marcolini [50] or BPM model proves to be reliable, especially for the axial wind turbine noises [27]. The semi-empirical model is based on the NACA0012 airfoil. Therefore, the fitted data for some of the boundary layer quantities are specific for this airfoil, and they should be investigated for the actual used airfoil. Besides the geometry of the blade, the model needs a clear spanwise distribution of the angle of attack (AoA) as many of the quantities required are fitted data based on the Reynolds number and AoA. Moreover, for an accurate prediction of the self-noises mechanism, boundary layer parameters such as boundary layer thickness or thickness displacement at the trailing edge (TE) should be derived depending on the flight speed, RPM, and angle of attack. It was decided to obtain these parameters through XFOIL [72] boundary layer analysis for simplicity, as the tool was already implemented and it presents this capability. The BPM model is constructed in such a way that the sound source is considered one meter behind the TE. If the observer's position is specified, the sound from its perspective can be computed.

Both models are described in Section 3.3 and Section 3.4. The formulations already include the effects of the spherical spreading, directivity, and Doppler shift. Finally, these models were implemented in MATLAB as functions that take as input the flight properties and airfoil's geometric properties, and their implementation was verified against experimental data from literature, as shown in Appendix B. The inputs required for these models to compute the noise emissions of the onboard ram-air turbine are presented in Table 5.1.

5.3. KITE NOISE

When a rigid airfoil is placed in a turbulent flow, surface pressure fluctuations occur along its surface. As these fluctuations reach a sharp trailing edge (TE), they are scattered and generate acoustic energy that propagates into the far field. This effect may be even more pronounced when using a flexible, inflatable kite [12].

Certain types of trailing edge noise—particularly those caused by vortex shedding, such as laminar boundary layer noise and blunt trailing edge noise—can produce narrowband or tonal sounds that are especially prominent at higher frequencies. In contrast, turbulent boundary layer trailing edge noise leads to broadband acoustic emissions. These often feature two distinct peaks, with the lower-frequency peak dominated by the suction side and the higher-frequency peak by the pressure side, depending on the displacement thickness

Table 5.1: Overview of input parameters required for the aeroacoustic prediction of the turbine.

Common Inputs (Hanson and BPM Models)	
Blade geometry	Includes chord distribution, blade radius, and sweep. Used for defining the aerodynamic and structural shape of the blade.
Flight speed	Ambient flow velocity affecting compressibility and sound propagation. Used for calculating the flight Mach number and Reynolds number.
Blade rotational Mach number	Local Mach number along the blade span, crucial for high-speed blade tips and tonal noise generation.
RPM of the turbine	Rotational speed of the blades; directly influences tonal noise components.
Number of blades	Determines frequency harmonics and affects the amplitude of the radiated noise.
Observer position in 3D space	Spatial coordinates of the observer used to compute relative angles and propagation direction.
Distance to observer	Required to compute the sound pressure level (SPL) at the observation point.
Environmental conditions	Includes ambient pressure, air density, and speed of sound. These influence both source noise generation and propagation through the atmosphere.
Hanson Model Specific Inputs	
Lift coefficient distribution - spanwise and chordwise -	Used to evaluate loading noise due to aerodynamic lift forces along the blade surface.
Drag coefficient distribution - spanwise and chordwise -	Required for modeling loading noise resulting from aerodynamic drag effects.
Blade thickness distribution - spanwise and chordwise -	Essential for computing thickness noise, which arises from volume displacement by the rotating blade.
BPM Model Specific Inputs	
Boundary layer thickness at TE - spanwise -	Determines trailing edge noise generation by controlling turbulence interaction with the blade edge.
Displacement thickness at TE - spanwise -	Represents boundary layer momentum loss; affects trailing edge noise predictions.
Angle of attack distribution - spanwise -	Affects the aerodynamic loading and the characteristic frequencies of broadband noise.

of the boundary layer. The pressure side typically emits lower-intensity sound, resulting in a decreasing trend in the overall acoustic spectrum.

The mid-span chord of the LEI kite of Kitepower measures approximately 4 meters, which implies a high Reynolds number and suggests that turbulent boundary layer TE noise will be the dominant source mechanism. However, given their significant contribution, all these noise mechanisms must be carefully considered and investigated with specific aerodynamic properties for noise modeling.

The Brooks–Pope–Marcolini (BPM) model [50], introduced in Chapter 3.3, is designed for fixed airfoils and has been widely used for propeller blades and axial wind turbines. However, the aerodynamics and resulting noise emissions of a leading-edge inflatable (LEI) kite are likely to differ. At the current moment, no aeroacoustic model has been specifically developed for soft kites. Bouman [12] applied the BPM model to simulate the noise generated by an LEI kite with relatively promising results. Accordingly, the BPM model is also utilized in this study to predict the self-noise produced by the LEI kite during flight.

One of the primary sources of inaccuracy in Bouman's work stems from geometric inconsistencies in the kite model and the treatment of boundary layer (BL) parameters. Rather than computing BL parameters for the specific flight conditions of the kite, Bouman [12] relied on empirical data fitted for the NACA0012 airfoil, as provided in the original BPM model. Additionally, the kite's geometry, particularly the chord and AoA distributions, was assumed to remain constant along the span, effectively modeling it as a rectangular wing, which does not accurately reflect its actual shape.

In the present study, the kite geometry is extracted with precision from a 3D model, as described in Chapter 6, and the boundary layer parameters at the trailing edge are computed using XFOIL [72], as detailed in Chapter 7. The needed input data for the prediction model of the self-airfoil noises of the kite are precisely the same as the ones needed for the onboard ram-air turbine as explained in the previous section, excluding the ones for Hanson's model. An overview of all the required inputs is found in Table 5.1.

5.3.1. ASSESSMENT OF FLUTTER-INDUCED NOISE IN LEI KITES

In addition to the self-noise mechanisms described for rigid airfoils in the Brooks–Pope–Marcolini report [50], an elastic airfoil can exhibit additional noise generation mechanisms. The deformation modes of the kite were discussed in Section 2.2.5, where it was concluded that the only mode operating within the audible range is associated with trailing-edge flutter.

The flutter frequency was estimated by drawing an analogy with the behavior of sails under tension or flags in flow. For both of these cases, experimental studies or DNS analyses have shown that the Strouhal number is typically close to unity [81, 82], with higher harmonics occurring at integer multiples. For the V9.60 kite developed by Kitepower, this corresponds to a flutter frequency in the range of approximately 10–40 Hz, depending on the flight velocity, chord, and tension within the material. This interval is consistent with the analytical formulations presented by Leuthold [23], as well as with the conclusions drawn from the analysis of flight video footage.

However, no suitable models were found in the literature to predict the pressure fluctuations or the resulting sound pressure levels generated by this phenomenon. Due to the lack of an established model, flutter noise was not included in the aeroacoustic prediction framework. Furthermore, the flight test audio recordings are dominated by wind noise in the lower frequency range. As a result, even if the flutter noise had been modeled, it would have been nearly impossible to validate or even identify it using the current audio data.

5.4. SOUND PROPAGATION EFFECTS

Several fundamental sound propagation mechanisms were considered during the development of the aeroacoustic prediction framework, including spherical spreading, Doppler shift, atmospheric absorption, and ground reflection. Among these, spherical spreading and Doppler shift are inherently accounted for in the component-level models used to simulate the noise generated by the kite, ram-air turbine, bridle lines, and tether. These two effects are particularly influential when source motion is considered: spherical spreading depends quadratically on the distance to the observer, while the Doppler shift is strongly affected by the relative speed of the system.

Additional effects—such as atmospheric absorption and ground reflection—were also implemented and evaluated. However, their influence on the predicted sound pressure levels was found to be minimal under the operational conditions considered in this study. Specifically, the open-field environment in which the Kitepower V9.60 system operates, along with the relatively short source-observer distances, reduces the impact of these secondary propagation effects. Simulation results showed variations of less than ± 1.5 dB due to reflection, which are within acceptable modeling uncertainty margins. Atmospheric attenuation was found to have a noticeable effect only at very high frequencies, above 10 kHz.

Although these secondary propagation effects have limited influence, they were implemented in the low-fidelity prediction framework for completeness. A full technical description of their implementation and evaluation is provided in Appendix C.

5.4.1. OVERALL A-WEIGHTED SOUND PRESSURE LEVEL

As previously discussed in Section 2.3, human hearing sensitivity varies across the frequency spectrum. To account for this perceptual bias, the A-weighting filter was selected for this study, as it is the most widely used standard in environmental noise assessments. The A-weighting correction was applied using the mathematical formulation defined by the International Electrotechnical Commission (IEC 61672-1:2013) [83]:

$$\Delta L_A = -145.528 + 98.262 \log(f) - 19.509 (\log(f))^2 + 0.975 (\log(f))^3, \tag{5.16}$$

where f is the frequency in Hz. This correction is added to the unweighted SPL at each frequency to approximate how sound would be perceived by a human listener. The Overall A-weighted Sound Pressure Level

(OASPL), expressed in dBA, provides a practical way to quantify perceived loudness by logarithmically summing the A-weighted SPL values across the frequency spectrum.

Although A-weighting is not a physical propagation effect, it can be applied in the post-processing phase to produce perceptually meaningful results. However, it was not applied to the flight audio recordings, as the microphone captures sound based on its own sensitivity—not human hearing—making A-weighting inappropriate for this comparison. Applying A-weighting to the simulated data in this context would compromise the validity of the comparison.

5.5. FINAL AEROACOUSTIC PREDICTION MODEL LAYOUT

In the Aeroacoustic Prediction Framework developed in this study, different modeling approaches are applied to each major component of the Airborne Wind Energy System, as explained in the above sections. The kite's self-noise is modeled using the Brooks–Pope–Marcolini (BPM) model, which accounts for trailing-edge noise mechanisms typical of airfoils. The ram-air turbine combines both the BPM model for broadband noise and Hanson's analytical model for tonal noise generated by rotating blades. For the tether and bridle lines, a vortex-shedding model is employed to estimate noise caused by unsteady flow separation around the cylindrical elements.

All of the component-specific models incorporate essential propagation effects—such as Doppler shift, directivity, and spherical spreading—within their respective formulations. However, atmospheric absorption, which becomes increasingly significant at higher frequencies and longer distances, is not inherently included in these models. To address this, it is implemented separately as a dedicated function within the framework. Additionally, an A-weighting filter is integrated into the post-processing stage, allowing for the calculation of Overall A-weighted Sound Pressure Level (OASPL) values to better reflect human auditory perception. An overview of the complete aeroacoustic prediction process is presented in Figure 5.2.

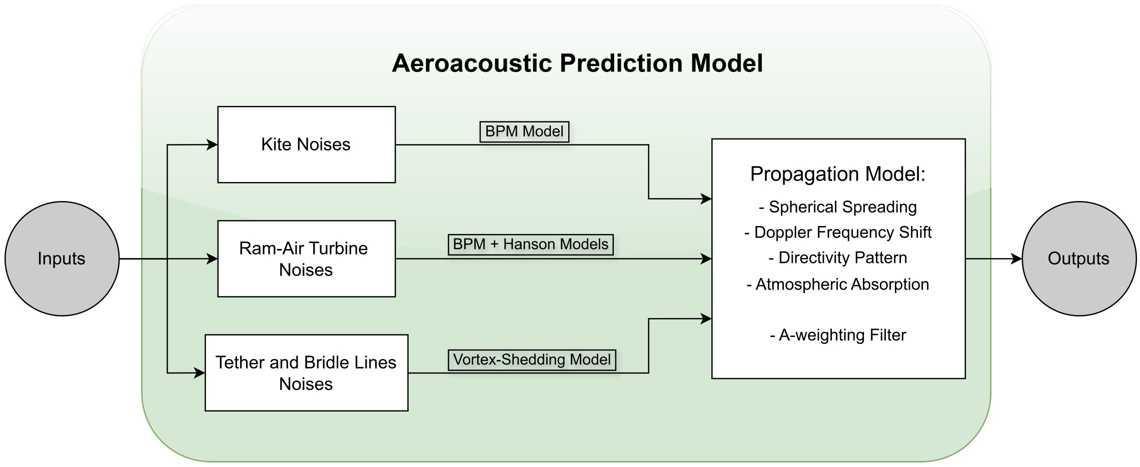

Figure 5.2: Schematic layout of the complete Aeroacoustic Prediction Model, including component-level noise sources and the integrated propagation effects.

6

Geometry Extraction and Properties

The geometrical properties of all system components serve as critical inputs for the aerodynamic analysis conducted using XFOIL [72], as well as for the Aeroacoustics Predictor described in the previous chapter. The current chapter outlines the procedures developed to extract and process this geometrical data.

Kitepower provided the *.stl* files containing the 3D models of the blade geometry used in their ram-air turbine, along with the V9.60 kite currently deployed in flight testing. The primary objective of the geometry extraction process is to isolate and define the airfoil profiles, enabling subsequent aerodynamic and acoustic analysis. To streamline this process, an automated extraction script was developed in MATLAB.

6.1. Kite Geometry

Due to the proprietary nature of the V9.60 kite geometry, the following extraction methodology is demonstrated using an earlier version of the kite—referred to as the V3 model—which is illustrated in Figure 6.1. The leading-edge inflatable (LEI) kite features a tubular leading edge (LE) and chordwise struts extending toward the trailing edge (TE). For the purposes of this analysis, the struts were excluded, and only the LE tube and the membrane canopy were retained for airfoil shape extraction.

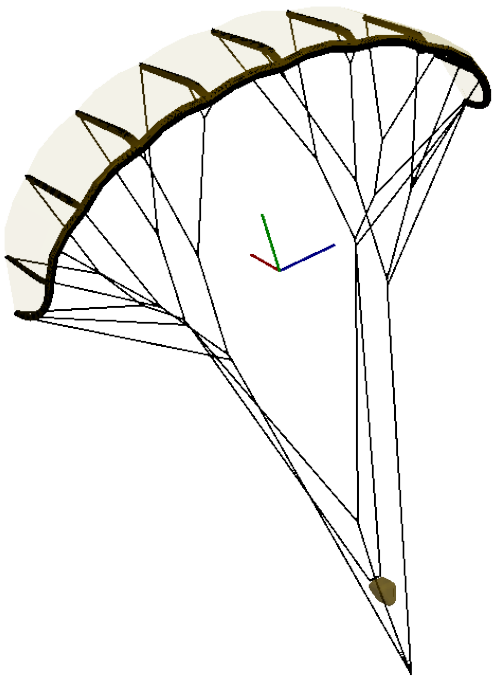

Figure 6.1: Kitepower's V3.25 kite presented as a 3D model used for slicing and airfoil extraction.

The MATLAB code reads the *.stl* file, interprets the mesh faces and vertices, and visualizes the 3D geometry. The user can then specify the desired locations along the span where airfoil cross-sections should be extracted. At each specified spanwise position, the code computes a local surface normal on the LE tube, constructs a plane passing through the corresponding point and oriented along that normal vector, and then intersects this plane with the 3D model. The resulting intersection defines the airfoil contour at that spanwise location. Figure 6.2 presents the V3 kite model with 9 sections, the middle section passing through the mid-span and divided with a cosine distribution.

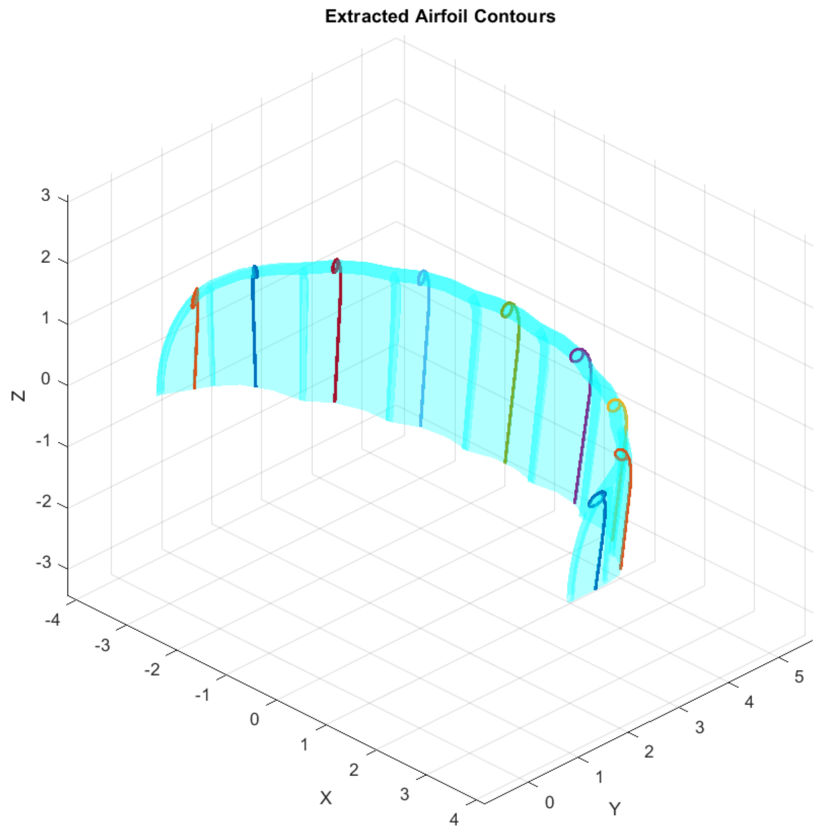

Figure 6.2: Sectioning strategy used for extracting airfoil contours along the kite span.

All extracted airfoil contours are saved in a data file for further processing. Upon inspection, it was found that the points obtained from the intersection are not ordered sequentially, making them unsuitable for direct use as closed airfoil profiles. To address this, a custom algorithm was developed that combines a nearest-neighbor approach with a smoothing criterion based on minimizing the angle between successive point triplets. This ensures a continuous and physically plausible airfoil shape. An example of such a result after the ordering process is illustrated in Figure 6.3a.

As previously discussed, the chord length and angle of attack (AoA) distributions along the span are essential parameters for determining the noise frequency spectrum of the component. To facilitate their calculation, the 3D model of the V3 kite is oriented such that the leading-edge is towards the positive global z-axis. This alignment is achieved by applying a rotation to all vertices using a rotation matrix R_θ, defined around an appropriate axis to satisfy the desired orientation.

Once aligned, the chord line at each section is determined by identifying the points with the minimum and maximum z-coordinates, corresponding to the trailing edge (TE) and leading edge (LE), respectively. The chord length is computed as the Euclidean distance between these two points. The relative angle of attack based on the kite's twist is then calculated as the angle between the local chord vector and the z-axis. The resulting chord length and local angle of attack distributions along the span are shown in Figure 6.3b.

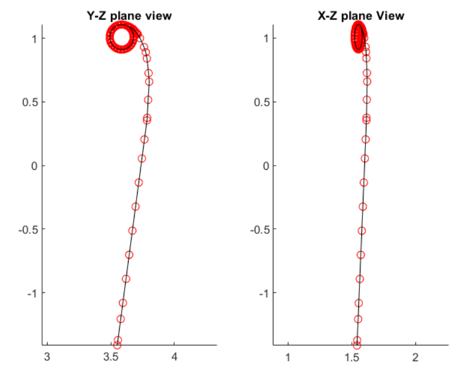

(a) Example of an extracted and ordered airfoil contour.

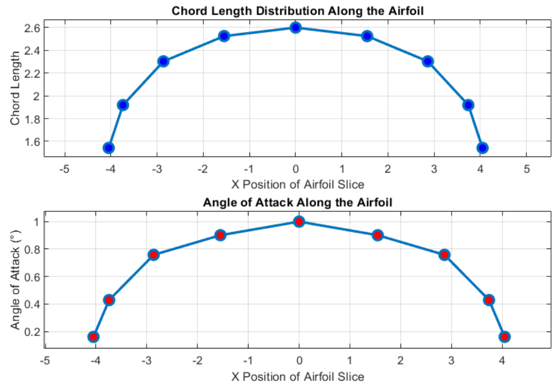

(b) Chord length and angle of attack distributions along the kite span.

Figure 6.3: Airfoil extraction and parameter distribution for the V3 kite.

6.2. ONBOARD RAM-AIR TURBINE GEOMETRY

The procedure used for turbine blade sectioning follows a similar logic to that applied to the kite, with a few simplifications. In this case, it is not necessary to rotate the blade or define normal planes along the surface, as the turbine blade is already aligned with the positive global x-axis in the spanwise direction.

Once the user specifies the desired number of sections, the code divides the blade span into equally spaced intervals and extracts the airfoil contours at those positions. The original 3D model of the turbine blade, as processed in MATLAB, is shown in Figure 6.4, while the blade sectioned at 15 positions along the span is illustrated in Figure 6.5.

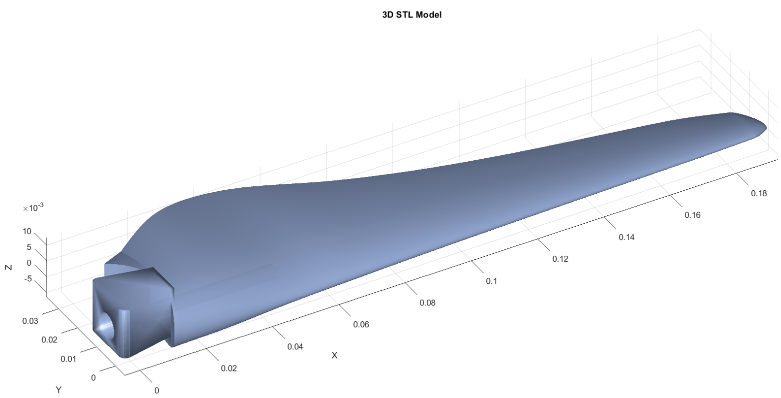

Figure 6.4: 3D model of the onboard ram-air turbine blade imported and processed in MATLAB.

Considering that the turbine rotates at a frequency influenced by the advance ratio, the apparent flow encountered by each blade section depends on both the axial freestream velocity and the rotational speed at that section. Since the rotational velocity increases with radial distance from the hub, the local apparent inflow angle—and thus the angle of attack—varies along the blade span. Additionally, the turbine blade features geometric twist, meaning that each section has a different pitch angle.

The twist angle θ is calculated by determining the angle between the local chord line and the xy-plane. To compute the inflow angle ϕ, the flight conditions must be known. Kitepower provided wind tunnel data for the turbine, including axial inflow velocity and RPM values. Using these, the local angle of attack α at a given spanwise location can be estimated using the following relationship:

$$\alpha = \theta - \phi, \quad \text{with} \quad \phi = \tan^{-1}\left(\frac{V}{\omega r}\right). \tag{6.1}$$

Here, V represents the axial freestream velocity, ω is the angular velocity of the turbine in radians per second, and r is the radial distance from the rotor hub to the point of interest. While a more rigorous approach

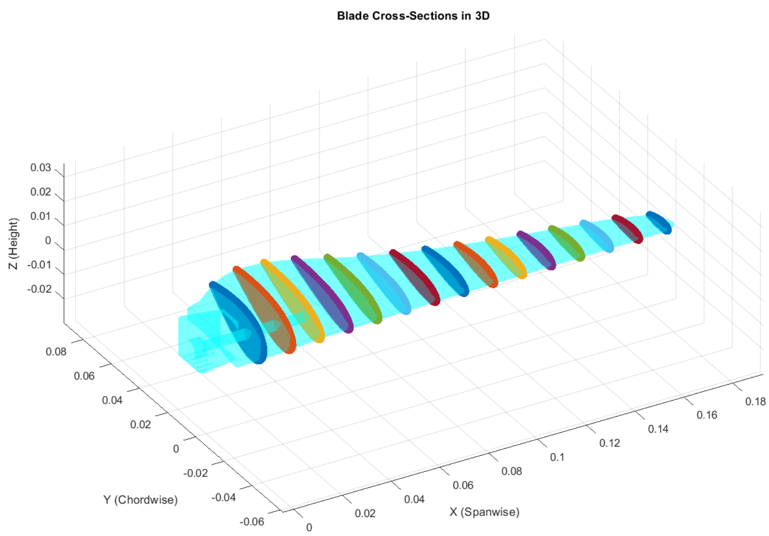

Figure 6.5: Blade sectioned at 15 spanwise locations for airfoil extraction.

would involve applying Blade Element Momentum (BEM) theory, this simplified method offers sufficiently accurate results for the scope of the current study.

The spanwise distribution of chord length, thickness, and angle of attack under nominal flight conditions is illustrated in Figure 6.6. The airfoil geometry, local angle of attack, and flight conditions can be further analyzed in XFOIL [72] to extract aerodynamic properties such as lift and drag coefficients, as well as boundary layer thickness and displacement thickness—parameters required for the aeroacoustic prediction models.

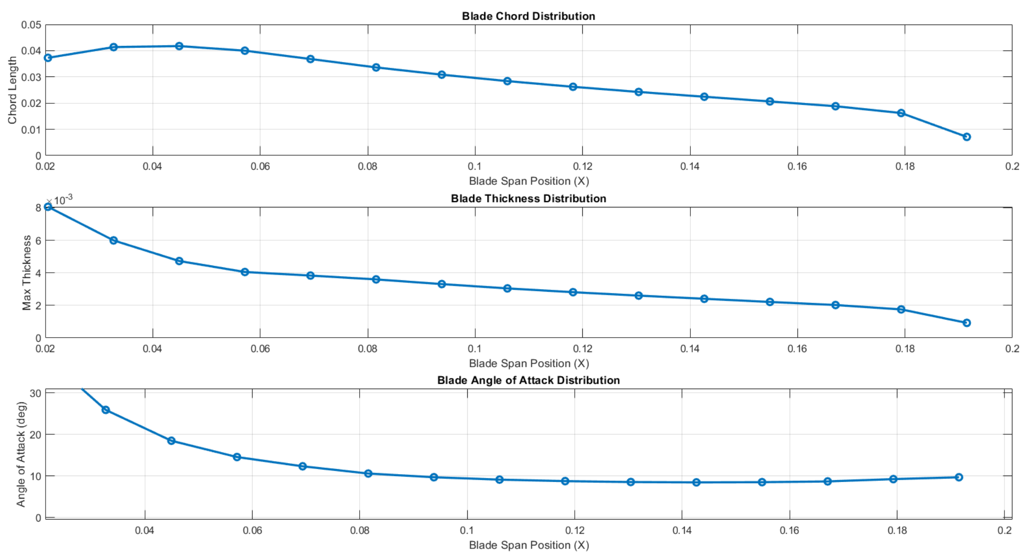

Figure 6.6: Chord length, thickness, and local angle of attack distribution along the turbine blade span at 20 m/s and 5000 RPM.

6.3. TETHER AND BRIDLE LINES GEOMETRY

The input data required for the tether and bridle lines do not require extensive processing. Kitepower provided the dimensional specifications of the materials used in their system. The tether consists of a 16-strand plaited hollow braid rope made of Dyneema®, with a diameter of 14 mm. The elevation angle, which determines the inclination of the tether, and the total tether length are obtained from the Extended Kalman Filter (EKF) developed by Cayon et al. [71].

During the reel-out phase, the tether is under high tension and can be approximated as a straight line, as can be observed in Figure 6.7. In contrast, during reel-in, the tether may exhibit noticeable sagging. The inclination angle plays a critical role, as it influences both the vortex-shedding frequency and the resulting sound pressure level (SPL), as discussed in Section 5.1. Since the flow velocity varies along the tether—lowest near the Ground Station and highest near the kite—it was decided to divide the tether into equally spaced segments. The local flow velocity is computed at the midpoint of each segment, and the vortex-shedding model is applied individually to each. According to Dunker [14], a long cylindrical body can exhibit multiple lock-in phenomena, meaning that vortex-induced vibrations (VIV) can occur at different frequencies along different sections of the tether.

Figure 6.7: Schematic of tether approximation as a straight line under high tension. Retrieved from Cayon et al. [71].

The bridle line configuration for the V3 kite is illustrated in Figure 6.1. Kitepower reported that the total bridle line length is approximately 402 m, with line diameters ranging from 2 mm to 8 mm. However, detailed information regarding the location, orientation, and specific usage of each line was not available. Therefore, it was assumed that all bridle lines are exposed to the same flow velocity as the kite itself and are oriented horizontally, with no inclination. For the acoustic simulations, the diameters used include 2 mm, 3 mm, 4 mm, 5 mm, 6 mm, and 8 mm, consistent with the simulations conducted by Bouman [12]. Each line diameter was assumed to have equal length when estimating its contribution to the total sound emissions.

GEOMETRY PROCESSING

The geometry processing methodology for each system component was discussed throughout this chapter. To summarize, Figure 6.8 provides an overview of the key steps involved in the geometric data extraction pipeline. This visual layout helps clarify the logic and structure behind the MATLAB-based framework implemented for processing the 3D models and preparing input data for the aerodynamics tool and aeroacoustic prediction model.

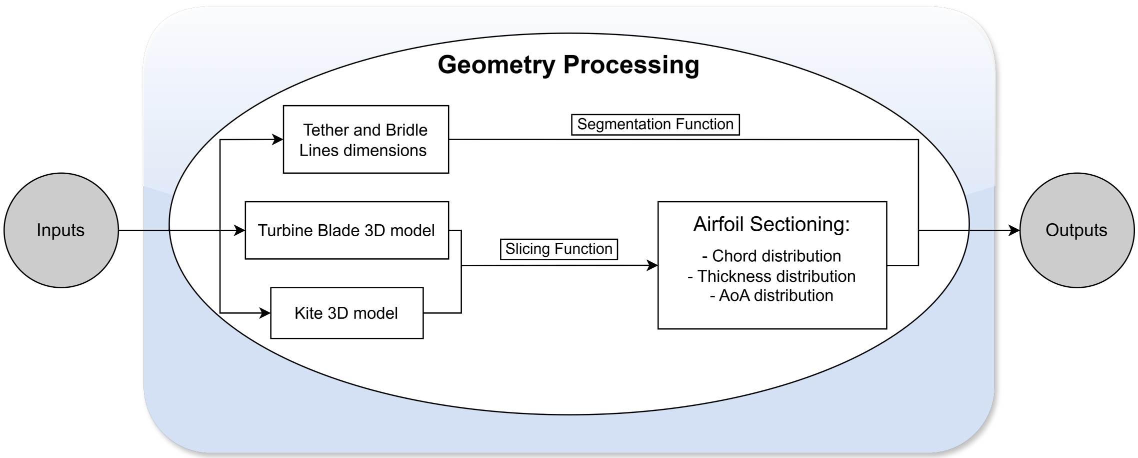

Figure 6.8: Schematic layout of the geometry processing steps for each component.

7

Simulation and Analysis Tools

This chapter presents the external tools integrated into the Aeroacoustic Prediction Framework for estimating flight states and extracting aerodynamic parameters. The Extended Kalman Filter (EKF) is used for real-time wind and system state estimation, while XFOIL is employed to compute aerodynamic properties needed for aeroacoustic modeling. Together, these tools provide essential input data for the noise models used in the prediction framework.

7.1. Extended Kalman Filter

Airborne wind energy systems require continuous active control, making them highly sensitive to wind fluctuations. To address this challenge, Cayon et al. [71] developed a sensor fusion framework based on an iterated Extended Kalman Filter (EKF), capable of estimating both system dynamics and wind conditions in real time.

The EKF combines multiple onboard measurements—such as kite position, velocity, tether tension, and reeling speed—within a dynamic model to estimate unmeasured states, including kite orientation, tether sagging, and wind characteristics. This eliminates the need for external sensing equipment, such as lidar, while still achieving high accuracy compared to reference systems. The EKF outputs can be used in supervisory control strategies, enabling adaptive trajectory optimization and improving system reliability.

Flight data recorded during test flights can be stored and later processed using the EKF, allowing for visualization and extraction of key parameters for applications such as noise prediction modeling. Both the V9.60 and V3.25 kites are equipped with a comprehensive sensor suite. However, due to IP-sensitive information, the following discussion focuses on the V3 kite, although the methodology is identical for the V9.

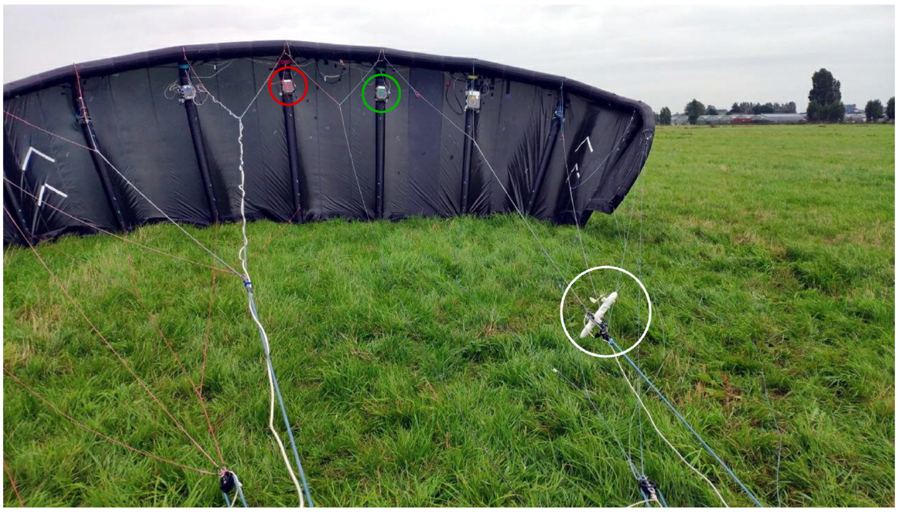

Figure 7.1: Fully instrumented layout on the V3.25 kite used for EKF-based state and wind estimation (red, green, and white circles showing Pixhawk® sensor 1 and 2, and flow sensors, respectively). Retrieved from Schelbergen et al. [84].

The sensor suite on the V3.25 kite includes a load cell to measure tether force, a linear encoder for tether length, and magnetic encoders for the azimuth and elevation angles of the tether at the ground station. Additional data is obtained from onboard GPS and IMU units, pitot tubes for apparent wind speed, and wind vanes for wind direction. The full sensor layout is illustrated in Figure 7.1.

By integrating all available sensor data into a dynamic model, the EKF produces a consistent and time-resolved estimation of the kite's aerodynamic state and the surrounding wind profiles. The complete methodology and implementation details can be found in the work by Cayon et al. [71]. These state estimations not only improve the system's control performance but also serve as key inputs for downstream models, including the Aeroacoustic Prediction Framework. Specifically, parameters such as the kite's angle of attack, apparent wind speed, three-dimensional position of the kite, and the length of the tether are extracted and used either directly within the aeroacoustic model or passed to the aerodynamic solver XFOIL [72]. The layout of the EKF solver is presented in Figure 7.2.

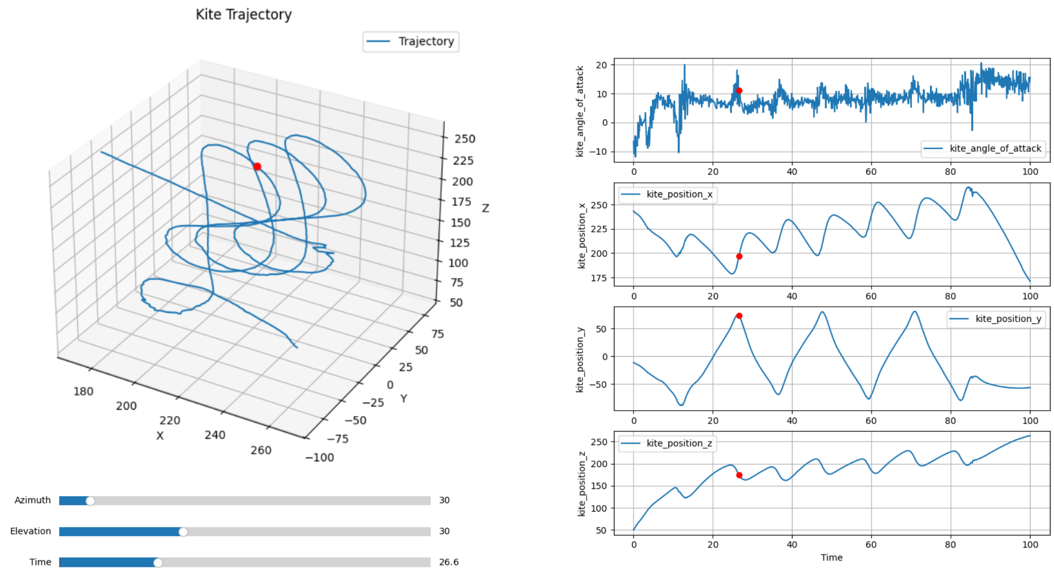

Figure 7.2: Example output from the Extended Kalman Filter (EKF) developed by Cayon et al. [71, 85], illustrating state estimation during the first 100 seconds of flight, including the take-off phase.

7.2. XFOIL

As explained in Chapter 5, the Hanson model [53] and the Brooks-Pope-Marcolini model [50] require aerodynamic data and parameters related to blade loading and boundary layer properties around an airfoil. XFOIL [72] was selected for this task due to its ease of automation and integration into the MATLAB framework, its ability to generate fairly accurate results quickly, and its prior use in similar aeroacoustic analyses, such as the methodology followed by Bouman [12]. XFOIL is a two-dimensional, low-fidelity aerodynamic tool that combines a linear-vorticity panel method for inviscid flow with an integral boundary layer formulation for viscous effects. The panel method calculates the surface pressure distribution assuming potential flow, while the boundary layer solver accounts for viscous phenomena such as transition, separation, and reattachment. These two solvers are iteratively coupled, allowing for the estimation of aerodynamic coefficients and boundary layer parameters, including displacement and momentum thicknesses.

Chapter 6 described how the airfoil shapes for both the turbine blades and the kite are extracted. These profiles can be directly imported into XFOIL along with the relevant flight conditions. A dedicated MATLAB script was developed to automate this process by launching the XFOIL executable in viscous mode, loading the airfoil coordinates, and applying the angle of attack (AoA) and flight parameters obtained from the EKF.

For the turbine blades, both the Reynolds number (based on chord length) and the Mach number vary along the span due to the rotation and increasing radius. Additionally, due to the twist of the blade, the local AoA changes with the spanwise position. All of these inputs are already calculated from the geometry extraction functions and the Extended Kalman Filter.

However, for the kite, the problem is more complex due to its unconventional airfoil shape. The airfoil is composed of a circular tube at the leading edge (LE) and a canopy that curves towards the trailing edge (TE). Because of the very thin material, the extracted geometry appears as a single line without distinguishable top and bottom surfaces. This poses difficulties for XFOIL as it needs clear top and bottom surfaces specified, but also due to the large recirculation zone that typically forms behind the cylindrical tube, which prevents convergence. An example of this flow pattern is shown in Figure 7.3.

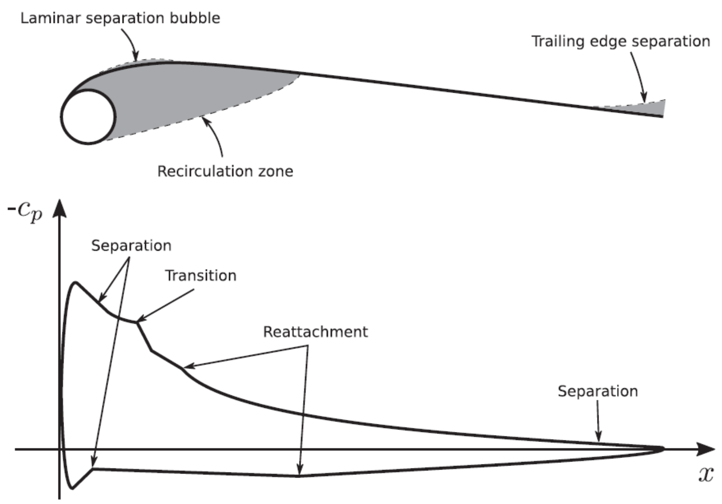

Figure 7.3: Flow behavior around an LEI kite section, showing the recirculation region. Retrieved from Folkersma et al. [86].

Two solutions have been proposed in the literature to address these issues. Because the canopy is extremely thin, negligible, meshing practices require artificially increasing its effective thickness. This introduces a trade-off: a thicker canopy improves meshing quality and solver convergence, but deviates more from the true geometry. Conversely, a thinner canopy is more accurate but harder to mesh. An illustration of this approach is shown in the work of Watchorn [87] in Figure 7.4.

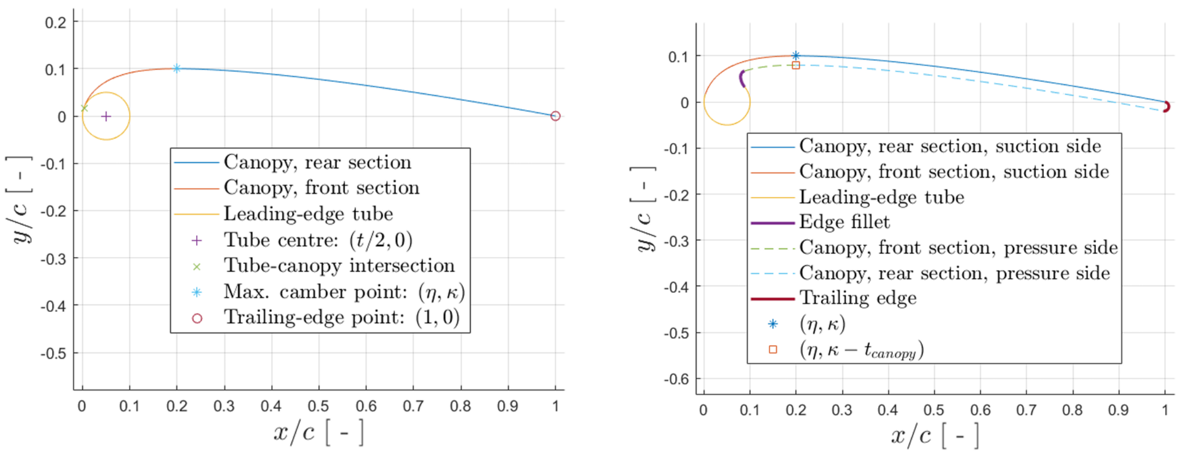

(a) Original thin canopy profile.

(b) Modified canopy with increased thickness.

Figure 7.4: Effect of airfoil thickness adjustment for improved meshing. Retrieved from Watchorn [87].

The second solution focuses on the suction-side flow separation. As seen in Figure 7.3, a large recirculation region forms behind the leading-edge tube, together with a TE separation on the pressure side depending on the AoA. When this region becomes too large, XFOIL cannot converge. Some authors have proposed adding a suction-side fillet behind the tube, smoothly connecting it to the canopy. This method was used by Deaves [88], as shown in Figure 7.5.

In the present study, a similar morphing strategy was applied to the mid-span airfoil of the kite prior to running simulations in XFOIL. This modification process was performed manually and proved to be challeng-

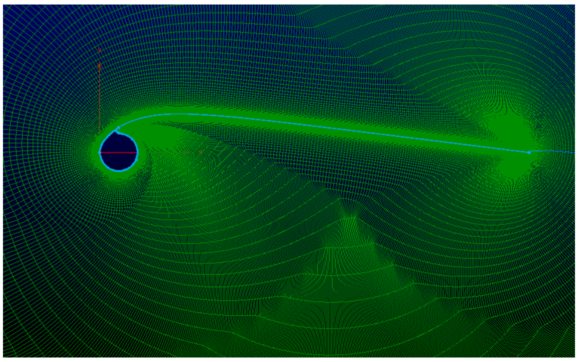

(a) Tight mesh.

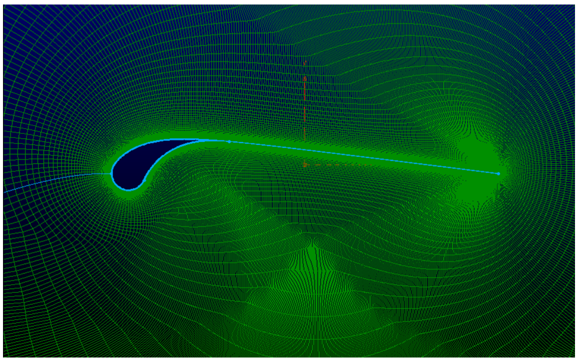

(b) Filled in mesh.

Figure 7.5: Modified airfoil with suction-side fillet to reduce recirculation. Retrieved from Deaves [88].

ing to automate. As a result, only the mid-span airfoil was used for aerodynamic simulations. Nonetheless, the airfoil shape along the kite span remains relatively consistent, making this simplification reasonable. The adapted airfoil used for XFOIL input is shown in Figure 7.6.

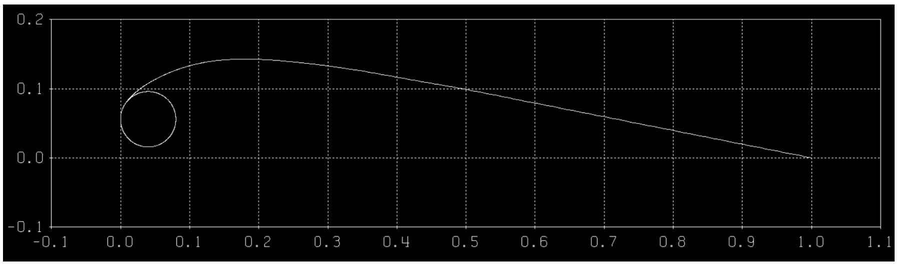

(a) Original airfoil shape of the kite at mid-span.

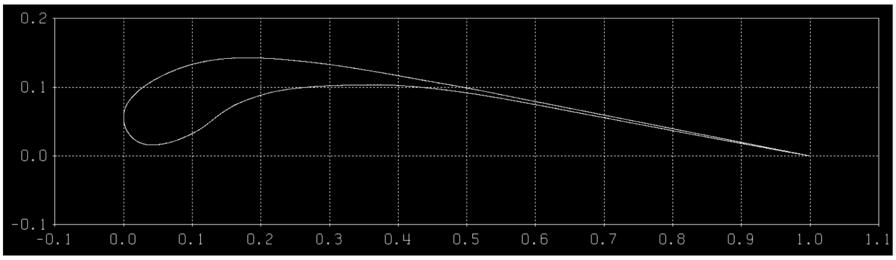

(b) Modified airfoil shape of the kite with added fillet.

Figure 7.6: Comparison of the original and modified airfoil shapes at the kite mid-span, showing the morphing process applied to enable XFOIL convergence.

Although the fillet may appear large, the airfoil thickness decreases significantly beyond mid-chord. This added volume behind the leading-edge tube was introduced to ensure XFOIL convergence during simulation. Since the kite's aeroacoustic modeling relies exclusively on the Brooks–Pope–Marcolini (BPM) approach [50], the key aerodynamic parameters required from XFOIL are the boundary layer thickness and the displacement thickness at the trailing edge.

While XFOIL does not directly output the boundary layer thickness, this parameter is mainly relevant for modeling laminar vortex-shedding noise. Given the high Reynolds number during kite operation, the flow is fully turbulent, and this noise mechanism is not dominant. In contrast, turbulent boundary layer trailing edge noise—dependent on accurate estimation of δ^*—is considered the primary sound source. For this reason, the airfoil was designed with a sufficiently long and thin trailing-edge region to allow full boundary layer development in the simulation, while preserving the original geometry as much as possible to enable reliable estimation of δ^*.

In reality, the flow recirculates on the pressure side behind the leading-edge tube. However, it is expected to reattach and allow boundary layer development along the remaining surface. CFD analyses using the

Reynolds-averaged Navier–Stokes (RANS) method were carried out for LEI kites by Lebesque et al. [89] and Folkersma et al. [86]. Both studies showed that at lower angles of attack and Reynolds numbers, reattachment typically occurs before $x/c = 0.6$ on the pressure side. As angle of attack and apparent wind speed increase, reattachment moves closer to the leading edge. These findings support the approximation made with the added fillet behind the tube.

Thus, the adjusted airfoil remains a valid approximation for extracting displacement thickness values at the trailing edge. The computed δ^* values are shown in Figure 7.7, based on a flight condition with an apparent wind speed of 27 m/s and an angle of attack of approximately 8°. The Reynolds number varies along the span due to changes in chord length, while the Mach number remains nearly constant. Local angle of attack variation must also be considered. Higher displacement thickness values on the suction side suggest possible separation near the TE, as expected from other studies and shown in Figure 7.3. Additionally, the lift and drag coefficients were verified against the results from Folkersma et al. [86], showing good agreement, particularly for lift.

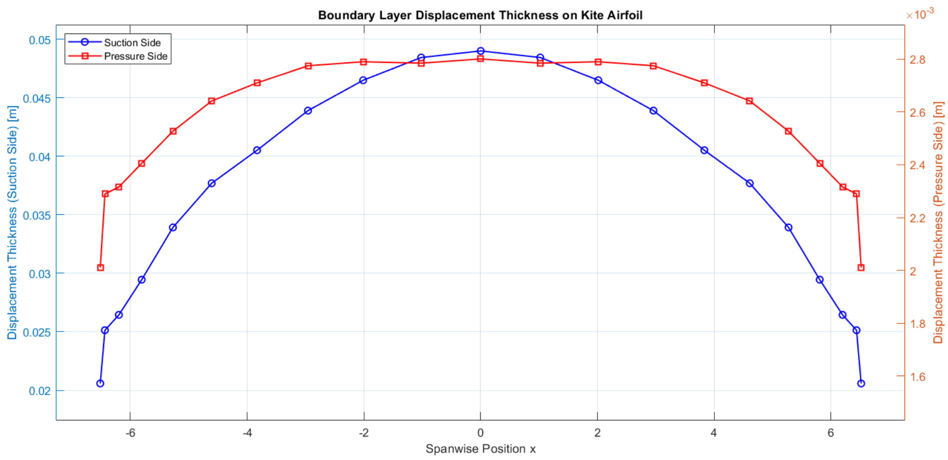

Figure 7.7: Displacement thickness δ^* distribution of the kite mid-span airfoil from XFOIL at $V_a = 27$ m/s and $\alpha \approx 9°$.

Aerodynamics Data Pipeline

The methodology for obtaining and extracting the aerodynamic properties has been outlined in this chapter. Figure 7.8 provides a schematic overview of the tools and functions involved in this pipeline. Unlike previous frameworks, this pipeline does not rely on external inputs, as the necessary geometric and flight data are provided directly by Kitepower or EKF, serving as the starting point of the simulation process. The entire workflow is largely automated in MATLAB—from running the XFOIL executable for all airfoils extracted through the Geometry Processing routines (as described in Chapter 6), to exporting key aerodynamic parameters for use in the Aeroacoustic Prediction Framework.

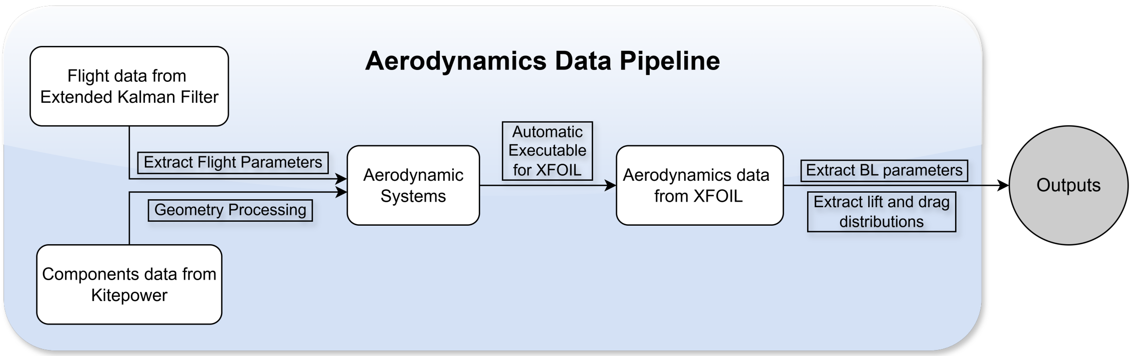

Figure 7.8: Schematic layout of the aerodynamic data extraction process for each component.

8
Audio Analysis

8.1. Acoustic Measurements

The audio recording used to validate Kitepower's acoustic emissions was obtained during a test flight conducted at the site in Bangor Erris, Ireland, on 27 November 2023. The footage was captured using a GoPro® camera, which recorded a 4K resolution video for approximately 1 hour and 23 minutes. During this period, a total of 66 pumping cycles were performed between launch and landing. A custom MATLAB script was developed to extract the audio stream from the original *.mp4* video files and convert it into a *.wav* format without loss of quality, which is more suitable for detailed acoustic analysis. The camera records in stereo using three built-in microphones, with a sample rate of 48 kHz.

Ground tracking data for the V9.60 kite during the flight is shown in Figure 8.1. The data illustrates the consistent and repeatable flight path, validating the controlled operational conditions maintained during testing and the constant wind direction.

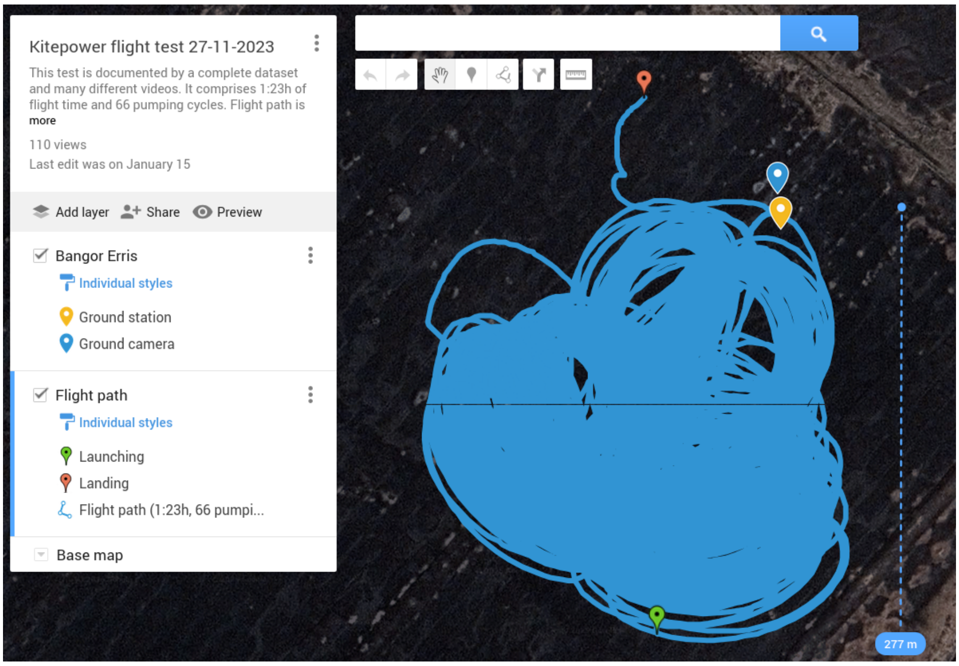

Figure 8.1: Kite's ground tracking position during the test flight on 27 November 2023 - Bangor Erris, Ireland.

All sensor data collected during the flight was logged and structured in accordance with the Extended Kalman Filter framework established by Cayon et al. [71], which facilitates further visualization and interpretation. As part of the MERIDIONAL project, these representative datasets have been shared with consortium partners and are scheduled for public release as open-access data by the end of 2025 [90].

During the flight, the main objective was data acquisition rather than maximum energy generation. As a result, the system operated under conservative conditions, leading to lower-than-normal power output. The wind was relatively steady, with an average speed of around 11 m/s, primarily coming from the southwest.

The position of the GoPro® camera used for the recording is shown in Figure 8.1. Based on GPS data, the camera was located approximately 24 meters upwind of the ground station and mounted a few centimeters above ground level. Its perspective is shown in Figure 8.2, which provides a visual overview of the ground station, the V9.60 kite, and the launch pad.

Figure 8.2: Camera view showing the ground station, V9.60 kite, and launch pad during the test flight on 27 November 2023 - Bangor Erris, Ireland.

8.1.1. BACKGROUND NOISE

The test site is located in a remote area, which ensures a low ambient noise environment with minimal external interference. However, it is important to note that the camera used was not specifically designed for aeroacoustic measurements. Consequently, it was not equipped with a windscreen or any protective cover to mitigate wind-induced noise. As a result, turbulence around the camera's microphone introduced significant unwanted noise, especially at low frequencies. Several methods can be employed to mitigate such noise, including spectral subtraction and filtering techniques. Spectral subtraction is most effective when the noise occurs at well-defined frequencies such as a tonal noise, which is not the case with wind noise, an observation also made by Bouman [12].

Given that wind-induced noise is primarily concentrated in the lower frequency spectrum, with minimal energy content above 500 Hz, a high-pass filter (HPF) was selected as the most appropriate method for noise reduction. An example of a spectrogram from the test flight, corresponding to the time interval between 330 and 360 seconds, is presented in Figure 8.3. The figure illustrates the concentrated noise caused by wind turbulence predominantly below the 500 Hz range, as previously discussed. An HPF allows higher-frequency components of the signal to pass through while attenuating or completely suppressing frequencies below a specified cutoff point. For this reason, it is also commonly referred to as a *low-cut filter*. The cutoff frequency was determined based on the characteristics of each recording, typically ranging between 250 Hz and 500 Hz.

It was tested multiple times whether the high-pass filter (HPF) would inadvertently remove noise generated by components of the airborne wind energy system (AWES). However, it was concluded that these components produced negligible acoustic energy within the filtered frequency range. Therefore, the use of the HPF proved to be an effective method for significantly reducing wind-induced noise while preserving the integrity of the relevant acoustic signals associated with the system's operation.

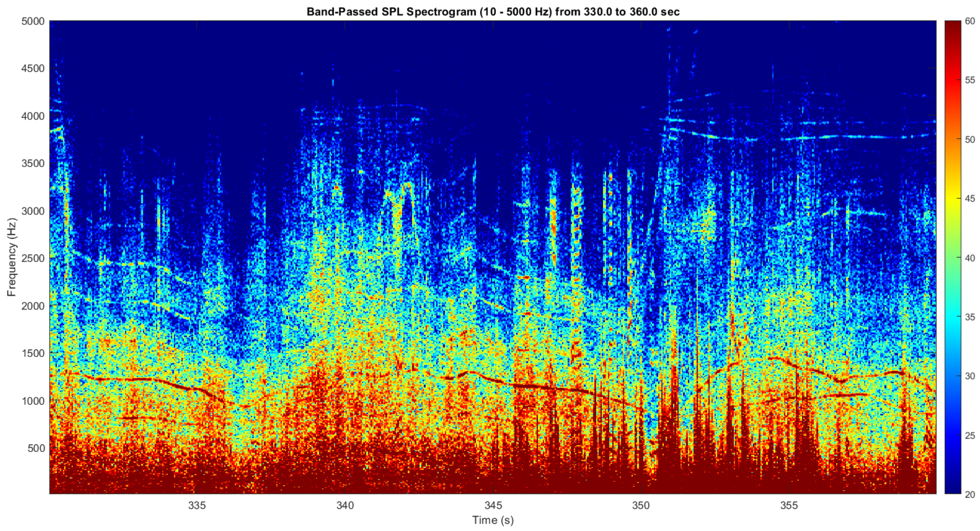

Figure 8.3: Example of spectogram between 330-360s of the recording showing the concentrated wind noise below 500Hz.

8.2. Frequency Domain Analysis

Frequency domain analysis is a fundamental technique in acoustic signal processing, enabling the extraction of spectral characteristics such as dominant tones, broadband noise, and harmonic content. The most commonly used method for this transformation is the Fast Fourier Transform (FFT), which converts a time-domain signal into its frequency-domain representation. This process is particularly valuable for analyzing the spectral content of aeroacoustic emissions captured during field tests, where noise sources can vary over time and exhibit both tonal and broadband features.

FFT-based spectral analysis is performed by segmenting a time-domain signal into overlapping frames, applying a window function to each segment, and computing the FFT individually for each frame. This approach enables time-resolved analysis of the signal's frequency components. The analysis is governed by several parameters, including frame size, window type, overlap, and sampling rate. Frame size determines the trade-off between time and frequency resolution—longer frames improve frequency resolution, while shorter frames enhance time resolution. The sampling rate defines the Nyquist frequency, which sets the upper limit of the analyzable frequency range. Frame overlap, typically between 50% and 75%, improves continuity between frames and reduces spectral leakage introduced by windowing.

Another important parameter is the number of FFT points, specified as N_{FFT}. This value determines the frequency resolution of the resulting spectrum, which is calculated as:

$$\Delta f = \frac{F_s}{N_{FFT}} \tag{8.1}$$

where F_s is the sampling rate and N_{FFT} is the number of FFT points. While it is common to set N_{FFT} equal to the frame size, using a larger value introduces zero-padding, which does not improve actual resolution but can make the spectrum appear smoother and more visually interpretable. In this study, N_{FFT} values between 8192 and 48,000 were employed depending on the analysis context, providing frequency bin spacings as fine as 1 Hz.

For example, a window duration of 0.1 seconds was used in some analyses, which corresponds to a frame size of 4800 samples at a sampling rate of 48 kHz. If the number of FFT points is set equal to 24,000, the frequency bin spacing becomes:

$$\Delta f = \frac{48,000}{24,000} = 2\text{ Hz} \tag{8.2}$$

However, it is important to distinguish between frequency bin spacing and actual spectral resolution. While the bin spacing is determined by N_{FFT}, the true frequency resolution is fundamentally limited by the duration of the analysis window. For a window duration of 0.1 seconds, the theoretical frequency resolution is approximately:

$$\text{Resolution} \approx \frac{1}{T_{\text{window}}} = \frac{1}{0.1} = 10 \text{ Hz} \tag{8.3}$$

This means that although the FFT output provides 2 Hz spaced frequency bins due to zero-padding, two tonal components closer than 10 Hz may not be reliably distinguished. While the increased value of N_{FFT} improves the visual smoothness of the spectrum, it does not enhance the physical resolving power of the analysis beyond the limit set by the window length. For tonal analysis, a longer window should be selected to maximize frequency resolution, whereas for broadband noise analysis, shorter windows are acceptable as precise frequency characterization is less critical.

By appropriately tuning the analysis parameters, FFT-based spectral analysis offers a robust framework for extracting meaningful insights from acoustic data. This includes the identification of tonal components, monitoring variations in broadband noise, and validating experimental results against predictive aeroacoustic models. In this study, audio recordings were sampled at 48 kHz. Window durations ranged from 0.1 to 0.5 seconds (corresponding to 4800 to 24,000 samples), with a 50% overlap between frames. The number of FFT points, N_{FFT}, was set equal to the sampling rate. These settings were applied using MATLAB's `spectrogram()` function.

8.2.1. WINDOWING IN ACOUSTIC SIGNAL INTERPRETATION

A common issue in the context of FFT analysis is *spectral leakage*, which occurs when a signal is truncated or not perfectly periodic within the observation window. This leakage introduces unwanted frequency components, distorting the true spectral representation of the signal. To mitigate this effect, a technique known as *windowing* is applied prior to performing the FFT.

Windowing involves multiplying the time-domain signal by a window function that tapers the signal's amplitude at the boundaries, thereby reducing discontinuities at the edges of the analysis frame. A visual representation of this method is presented in Figure 8.4. Several types of window functions exist, each with trade-offs between main lobe width and side lobe suppression, which impact frequency resolution and leakage control.

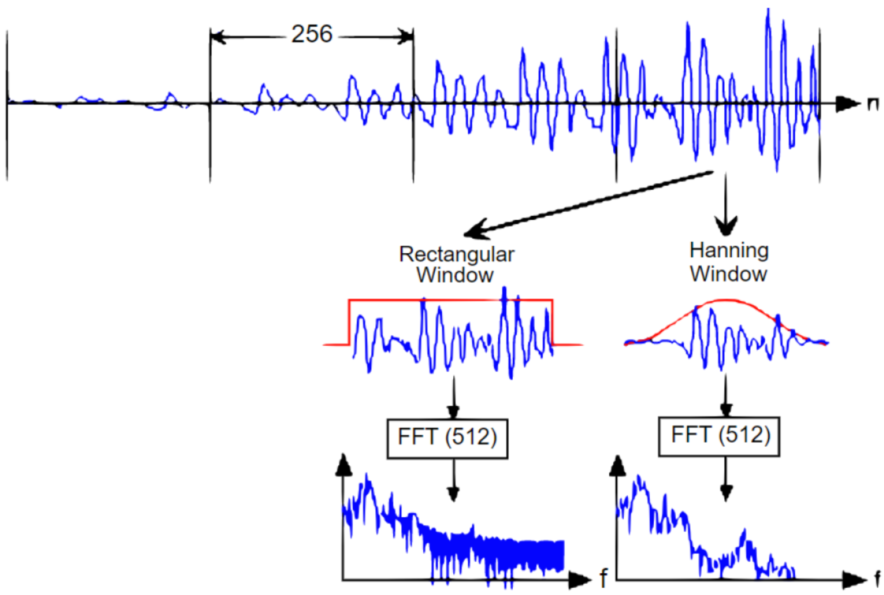

Figure 8.4: Example for applying a rectangular window and a Hanning window to the same signal. Retrieved from Johnson [91].

In this study, various window functions were considered, including the Hann, Hamming, and Blackman windows, each of which offers improved side lobe attenuation compared to a simple rectangular (non-windowed) approach. The Hann window was selected for its effective balance between spectral resolution and leakage suppression, making it suitable for general-purpose acoustic analysis. Its cosine-shaped taper reduces spectral leakage while preserving frequency detail through a relatively narrow main lobe width.

8.2.2. CONVERSION TO SPL

When FFT is applied to a windowed time-domain signal, the result yields a complex-valued output whose magnitude represents the contribution of each frequency component present in the signal. Mathematically, for a signal $x(n)$ with N samples, the FFT is given by:

$$X(k) = \sum_{n=0}^{N-1} x(n) \cdot e^{-j2\pi kn/N} \tag{8.4}$$

The magnitude spectrum is then computed as:

$$|X(k)| = \sqrt{\Re(X(k))^2 + \Im(X(k))^2} \tag{8.5}$$

This spectrum provides the amplitude of each frequency bin, but the raw FFT output is not immediately interpretable in terms of sound pressure level (SPL), which is a logarithmic measure more closely related to perceived loudness. Therefore, it is common to convert the FFT magnitudes to SPL using the following relationship:

$$SPL(f) = 20 \cdot \log_{10}\left(\frac{|X(f)|}{p_0}\right) \tag{8.6}$$

where $p_0 = 20 \times 10^{-6}$ Pa is the standard reference pressure in air. This formula requires that the signal be expressed in units of sound pressure (Pa).

For dedicated microphones, the conversion between voltage units and pressure is done through a gain-specific factor for all frequencies, as shown in Figure 8.5 for the M51 microphone used by Van Den Kieboom [17]. The audio signal used in this analysis was recorded using a GoPro® camera, which does not provide calibrated sound pressure data. Consequently, the signal amplitude is in arbitrary digital units and cannot be directly converted to physical sound pressure levels without a known microphone sensitivity or calibration reference.

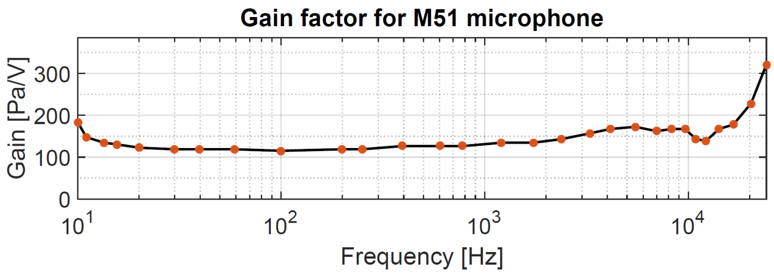

Figure 8.5: Gains of the M51 microphone used by Van Den Kieboom. Retrieved from Van Den Kieboom [17].

To address this limitation, a constant gain factor was applied to scale the recorded signal so that the resulting SPL spectrum could be meaningfully compared to the aeroacoustic prediction model. While the exact value of this gain is unknown due to the lack of a microphone calibration factor, it was selected empirically by aligning the amplitude of the measured spectrum with that of the prediction model, based on clearly identifiable tonal components. Although this approach does not yield absolute SPL values, it serves as a valid method for relative comparison and validation.

It is important to emphasize that this process does not compromise the spectral integrity of the data. The spectral shape, tonal peaks, and frequency distribution remain accurate, allowing for meaningful interpretation of harmonic content and overall spectral behavior. Therefore, the gain-adjusted SPL spectrum can be used reliably for evaluating the aeroacoustic characteristics of the system and assessing the accuracy of the prediction code, as long as the comparison is interpreted as relative rather than absolute. This distinction is especially important in interpreting the results presented in Chapter 9.3, where relative spectral comparisons are used to assess the performance of the prediction framework under real-world conditions.

ACOUSTICS ANALYSIS TOOL

A dedicated MATLAB tool was developed to facilitate the acoustic analysis of field recordings. The script enables any `.mp4` video file to be converted into a `.wav` audio format suitable for frequency-domain analysis.

This allows for the extraction of both tonal and broadband noise components generated by the airborne wind energy system (AWES). After applying an HPF and a constant gain factor, the resulting spectrum can be transformed into SPL and compared against predictions from the aeroacoustic simulation framework.

Figure 8.6 illustrates the structure of the MATLAB analysis tool using a publicly available video featuring Toyota's inflatable kite [92], in which trailing-edge fluttering is both visually observable and acoustically identifiable. The tool can play both the video and processed audio file in the same window, aiding with the visualization of different acoustics effects.

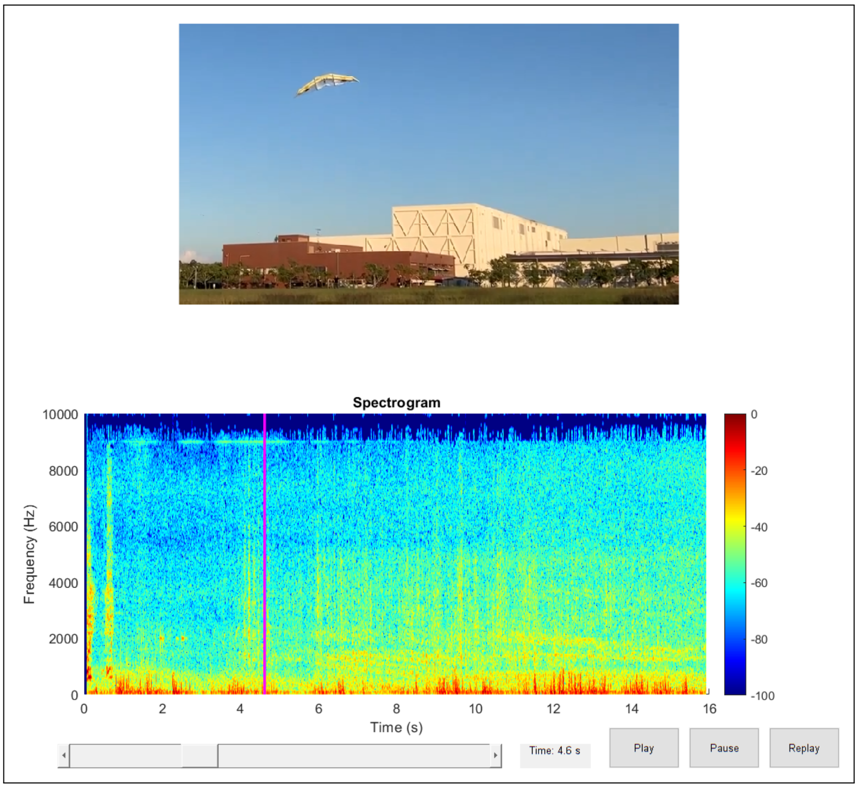

Figure 8.6: Acoustic analysis tool applied to a video of Toyota's inflatable kite [92], demonstrating clearly observable trailing-edge flutter.

The schematic layout of the full audio analysis process is presented in Figure 8.7. It shows all steps involved in extracting experimental data and preparing it for comparison with simulated results from the Aeroacoustic Prediction Framework.

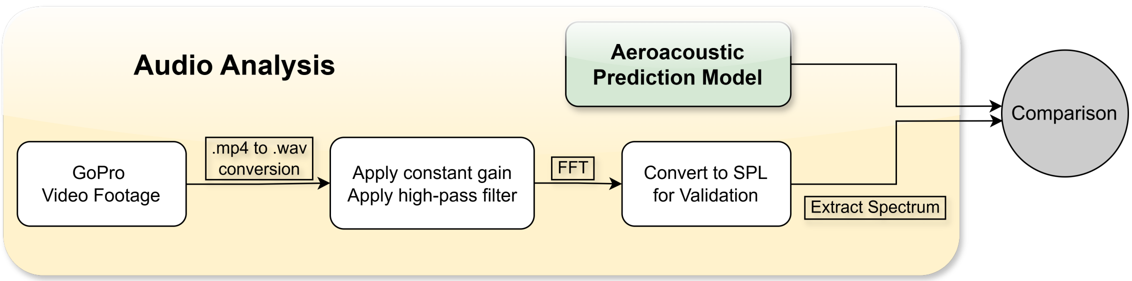

Figure 8.7: Schematic layout of the audio analysis process and validation against predicted aeroacoustic data.

III

RESULTS AND CONCLUSION

9

Results and Discussion

This chapter presents the results of the Low-Fidelity Aeroacoustics Prediction Framework along with its validation through comparison with experimental data. To maintain a clear structure, the results are organized into three main sections.

The first section showcases the predicted acoustic outputs generated by the aeroacoustics framework at selected moments during the flight. These predictions include contributions from all modeled noise sources, as described in Chapter 5, and incorporate atmospheric absorption effects. The second section provides a frequency-domain analysis of the measured audio data, including both the frequency spectrum and spectrogram at specific points during the test. Finally, the third section focuses on the comparison between the predicted and measured spectra. The audio was recorded using a GoPro® camera and captures a total of 66 pumping cycles over a span of more than 80 minutes. Only a few representative instances are analyzed in detail to assess the model's performance and identify similarities and discrepancies between the simulation and experimental results.

The interpretation and broader implications of these findings are discussed in the following chapter, followed by a summary of conclusions.

9.1. Aeroacoustic Prediction Framework

All the steps followed in developing the Aeroacoustic Prediction Framework are detailed in Chapter 5 and illustrated schematically in Figure 5.1. The model inputs include parameters related to flight conditions, environmental factors, and the dimensions and geometry of components. A significant portion of the flight data is derived from the Extended Kalman Filter (EKF) developed by Cayon et al. [71], which is utilized either directly as input for the Aeroacoustic Prediction Model or for aerodynamic analysis. XFOIL is the solver used for the aerodynamics of the system which takes as input the airfoils sectioned after the Geometry Processing part and the flight data from EKF.

The subsequent steps involve applying the Brooks-Pope-Marcolini model [50] for airfoil self-noise from both the kite and turbine, the Hanson model [53] for the tonal components of the turbine, and the Vortex Shedding model for noise from the turbine and the tether. This approach covers all the considered components and their acoustic emissions. The entire framework has been implemented in MATLAB as a standalone tool, which, based on all the inputs, predicts the noise as heard by an observer at a specified position. Results from this analysis are briefly presented in this section. Initially, the model was tested with only generic data to verify its functionality. Some of the key parameters needed for this analysis are displayed in Table 9.1.

Table 9.1: Parameters of the system for testing the Aeroacoustic Prediction Framework.

Apparent wind speed	25 m/s	**AoA of the kite**	5.5°	**Kite elevation angle**	30°
Turbine BPF	400 Hz	**Tether length**	250 m	**Tether sections**	5
Bridle lines total length	420 m	**Bridle sections**	9 (different diameters or inclinations)		

Based on these parameters, the aerodynamic properties of the kite airfoil and the turbine blades are derived using XFOIL. Once these properties are input into the framework, the results are obtained and can be viewed in Figure 9.1.

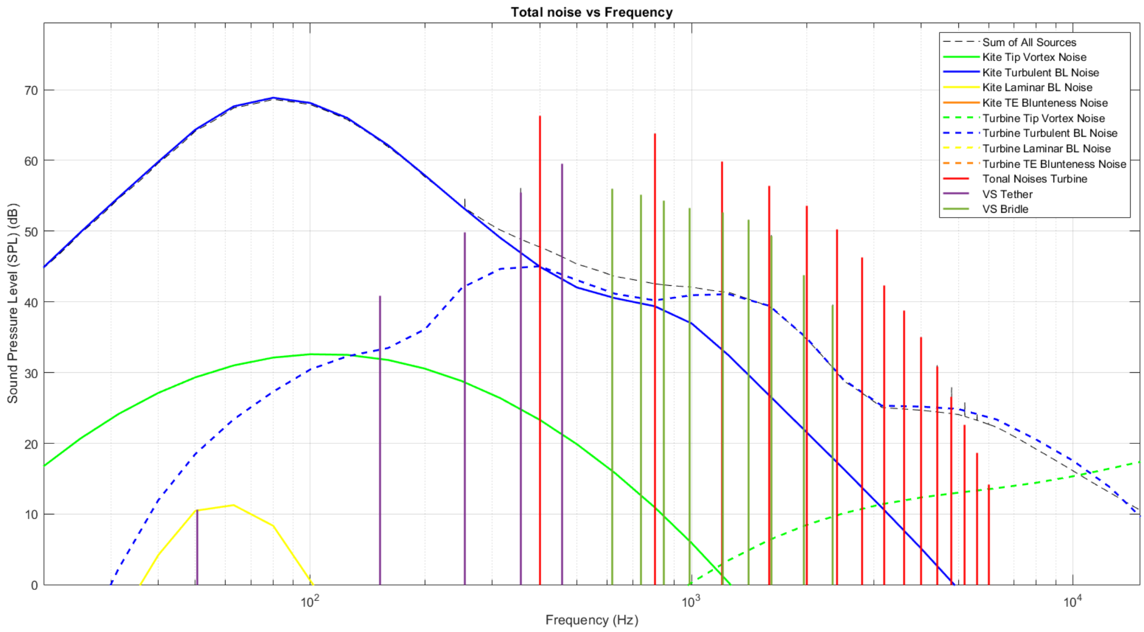

Figure 9.1: Predicted SPL results for kite, turbine, tether and bridle lines components using the Aeroacoustic Prediction Framework.

Due to the high Reynolds number and the large chord length of the kite, the dominant self-noise mechanism is identified as turbulent boundary layer trailing edge (TBL-TE) noise. This outcome was anticipated, given the flow conditions and airfoil geometry. The same applies to the turbine, where TBL-TE noise also represents the primary acoustic source. As expected, the prediction models confirm that laminar vortex shedding noise is negligible, given the fully turbulent flow regime around both the kite and turbine airfoils. Similarly, noise generated by trailing-edge bluntness is negligible, due to the sharp trailing edge geometry of both components. While this was anticipated, the prediction models have now confirmed that both laminar vortex shedding noise and TE bluntness noise can be disregarded.

The phenomena observed at higher angles of attack of the kite, as discussed previously and illustrated in Figure 7.3, reveal a significant flow separation region on the suction side near the trailing edge. While such behavior has been discussed in prior studies [86], it is also clearly captured through XFOIL simulations. For example, Figure 9.2 shows the separation pattern at an angle of attack of 15°, confirming the presence of this effect. As a result, the primary noise mechanisms associated with the kite are strongly influenced by flow separation near the trailing edge.

For the turbine, the TBL-TE noise is observed at higher frequencies compared to that from the kite. This shift is primarily due to the turbine's smaller chord length and elevated rotational speed (RPM), both of which contribute to a thinner boundary layer displacement thickness, δ^*. The reduced δ^* leads to a shift in the TBL-TE noise spectrum toward higher frequencies, in accordance with theoretical predictions.

While the discussion so far has focused primarily on self-noise generated by the airfoils, it is evident that some of the highest sound pressure level (SPL) values arise from tonal noise components. These are particularly significant in the 1–4 kHz frequency range, which coincides with the range of human speech and where human hearing sensitivity is heightened.

Among these tonal components, the blade passing frequency (BPF) noise from the turbine and the vortex shedding noise originating from the tether or bridle lines were calculated and plotted as discrete tonal peaks centered at specific frequencies. This approach aligns with the theoretical framework. However, in real-world scenarios, tonal noise is rarely confined to a single frequency. Although it maintains a dominant peak, the energy is typically distributed around that frequency.

Bouman [12], building on the experimental results of Latorre Iglesias et al. [65] for vortex shedding noise around a cylinder, modeled this distribution by applying a normal distribution function around the tonal peaks. This approach better reflects the spread of noise observed in physical measurements. However, in the present study, the tonal components have been represented as sharp peaks centered only on the predicted frequencies.

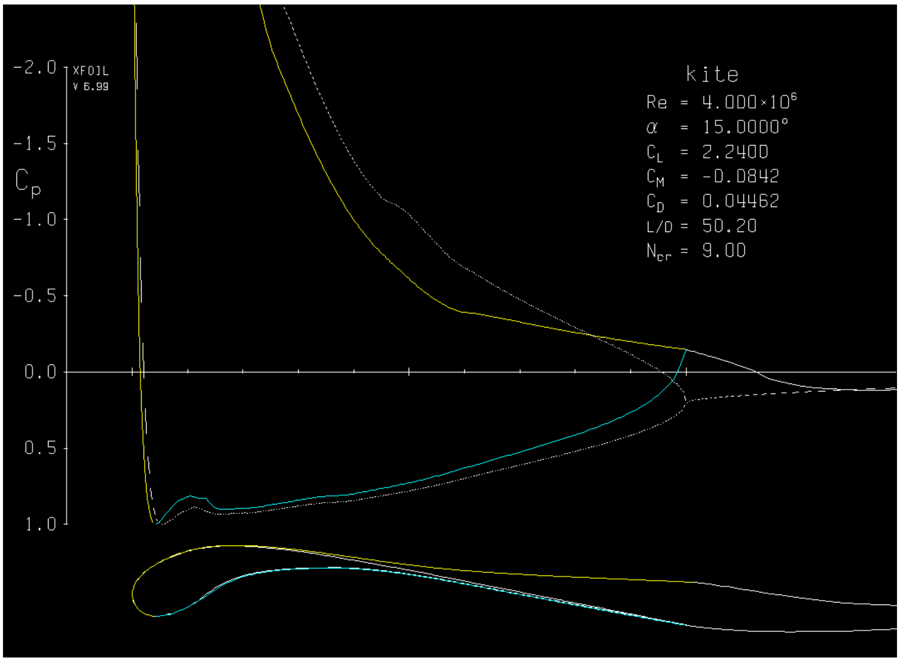

Figure 9.2: Kite results from XFOIL for 15° angle of attack. The yellow line shows large flow separation on the suction side towards the trailing edge.

The thin black dotted line in Figure 9.1 represents the total predicted noise from all components, shown without the application of any filters. This line corresponds to the cumulative sound spectrum of the entire system. At higher frequencies, it may appear that the total noise level is lower than that of individual components—particularly the TBL-TE noise from the turbine. However, this is not an error. The apparent drop is due to the inclusion of atmospheric absorption effects, which have already been applied to the total noise curve. Atmospheric absorption disproportionately affects high-frequency sounds, attenuating them more than low-frequency components over distance. This effect is illustrated in Figure C.1, where the absorption characteristics were analyzed. Consequently, the reduction in high-frequency noise seen in the total noise plot is a result of applying the propagation effects.

For improved clarity and interpretation, the overall results generated by the Aeroacoustic Prediction Framework showing the SPL contributions across the full spectrum without filtering are presented in Figure 9.3a. This plot provides a comprehensive view of the predicted acoustic behavior of the entire system under generic operational conditions.

For completeness, the A-weighting filter was applied to the overall results produced by the Aeroacoustic Prediction Framework. The methodology for applying perceptual noise weighting was discussed earlier in Section 2.3, and the corresponding attenuation function as a function of frequency is presented in Equation 5.16. This filter aligns with the frequency-dependent sensitivity of the human ear. Low-frequency components below 250 Hz are strongly attenuated under A-weighting, while mid-range frequencies—where human hearing is most sensitive—may even be amplified, leading to a perceived SPL higher than the actual source level. High frequencies are also attenuated, reflecting the reduced sensitivity of human hearing at those ranges.

The final outcome of the Aeroacoustic Prediction Framework, incorporating both atmospheric absorption and A-weighted filtering, is illustrated in Figure 9.3b. This figure provides an estimation of how an observer at the designated location would perceive the total noise emitted by the system, offering a more realistic interpretation from a human auditory perspective.

9.2. AUDIO ANALYSIS RESULTS

During the flight test, the GoPro® camera was positioned upwind of the ground station. In close proximity to the camera, two operators were present and occasionally engaged in conversation regarding the test. As a result, the time frame selected for analysis had to be carefully chosen to avoid any segments containing

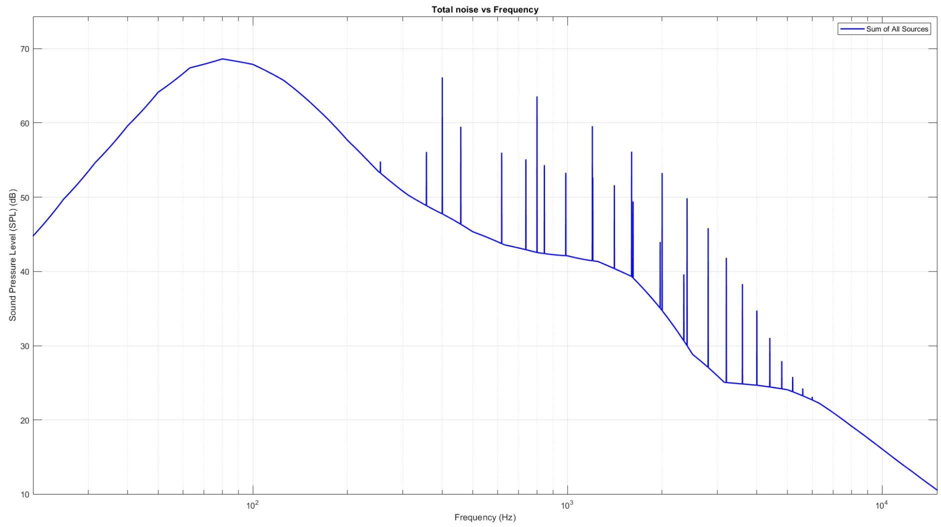

(a) Unfiltered SPL results showing all noise components and total system noise including atmospheric absorption.

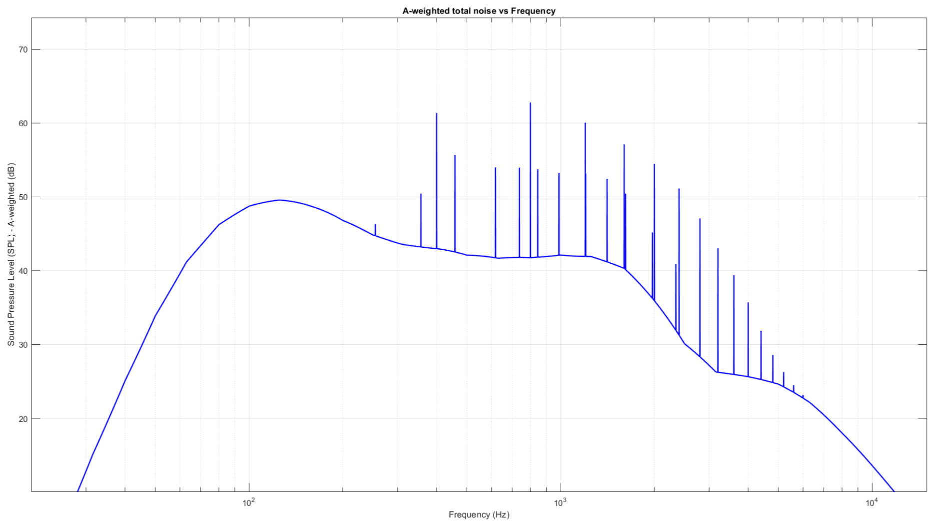

(b) A-weighted SPL results, representing perceived system noise by an observer.

Figure 9.3: Comparison of predicted SPL results: (a) without filtering and (b) with A-weighted filtering.

speech or unrelated ambient noise. Due to the large volume of recorded data, identifying a clean segment for analysis was not a limiting factor. One such longer time frame was found between 1716 and 1856 seconds, during which the kite completed more than two full power cycles, averaging around 60 seconds per cycle (including reel-in period). This 140-second section can be a base example for the following observations regarding the audio analysis. The spectrogram corresponding to this interval is shown in Figure 9.4.

For this analysis, a band-pass filter was applied with cut-off frequencies set between 300 and 10,000 Hz. The lower limit was chosen to suppress the majority of wind-related noise, as discussed in Chapter 8. There are also some higher frequency contributions from the wind noise, but it is difficult to remove them without loss of other data. The upper limit of the filter was defined based on the observation that the GoPro® microphones captured negligible signal content above 10 kHz.

From the spectrogram, it is evident that the signal exhibits very low SPL values for frequencies above approximately 5500 Hz. One notable exception is a tonal noise component originating from the winch/generator system. During the reeling-in phase, the electric motors operate to retract the tether and return the kite to its initial position. Since the camera is positioned near the ground station, this tonal noise is clearly captured and visible in the spectrogram, making it easier to identify different phases of the power cycle.

In the spectrogram shown in Figure 9.4, reeling-in occurs during the first 20 seconds of the window and

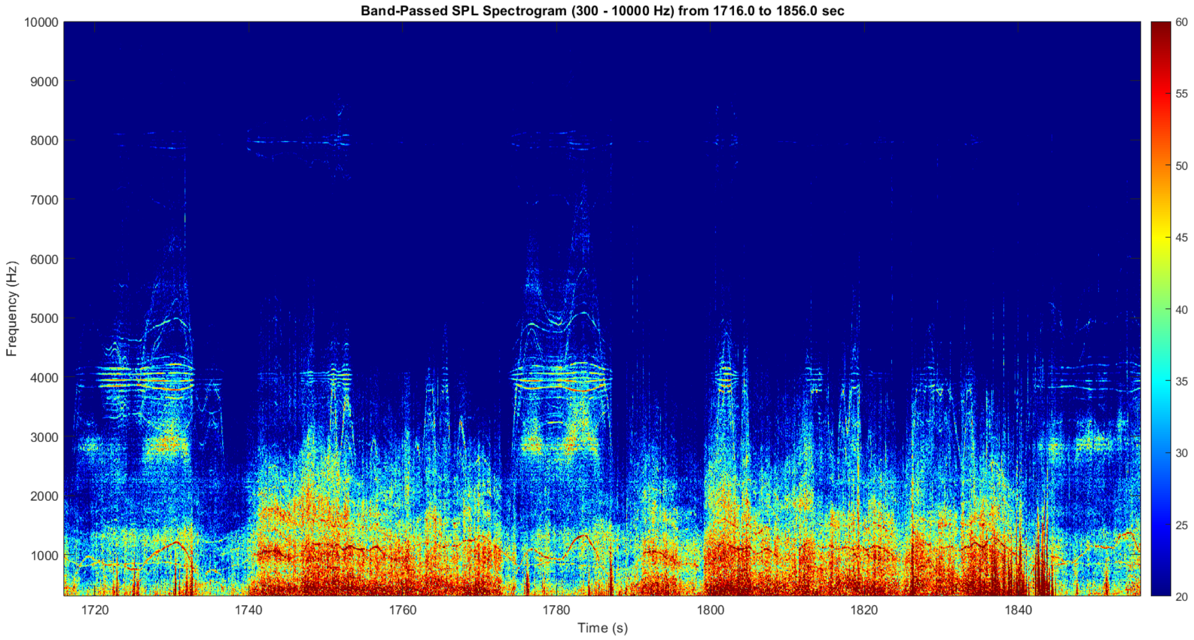

Figure 9.4: Spectrogram of the flight audio between 1716 and 1856 seconds, covering two full power cycles.

again between approximately 1775 and 1790 seconds. The high-pitched sound generated by the winch is distinctly audible in the audio recording, which allowed for the confident identification of the noise source. Additionally, it was observed that the winch/generator noise appears active during the reel-out phase, as evidenced by a tonal feature visible near the 1800-second mark. This is most probably due to high production of energy during harvesting period or to ensure tension in the tether for optimal control.

A more detailed view of the winch noise is presented in Figure 9.5, where the tonal components are more distinctly visible. These tones appear to be harmonics of a fundamental frequency and serve as a reliable acoustic signature for identifying winch activity during the operational cycle. Interestingly, the most prominent peaks in the SPL spectrum are found around the fourth harmonic, near the 4 kHz region, while the lower harmonics are either weak or not clearly detectable. This suggests that the energy of the winch noise is concentrated in the higher frequency range, rather than being evenly distributed across the spectrum.

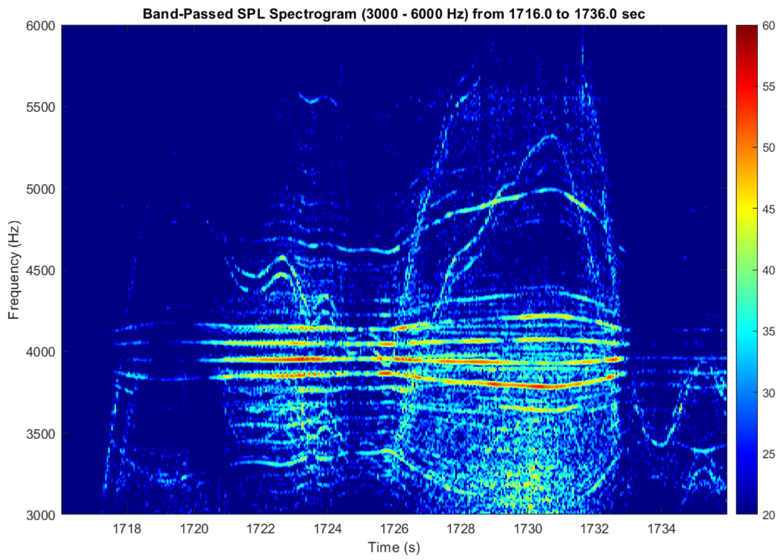

Figure 9.5: Detailed spectrogram showing the tonal components of the winching noise during reel-in.

A closer analysis is now conducted on the second power cycle shown in Figure 9.4. By examining the data from the Extended Kalman Filter (EKF) developed by Cayon et al. [71], it was determined that there is a time offset of approximately 19.6 seconds between the EKF data and the video recordings. This offset was used to synchronize the EKF data with the audio and video recordings with high precision.

Figure 9.6 presents a comparison between the EKF flight trajectory data and the spectral content of the corresponding time frame. The EKF analysis shows that the kite performs three large turns during this interval, along with an initial reorientation immediately following the reeling-in phase. During each turn, the kite descends and accelerates, followed by a climbing phase in which its apparent velocity decreases. The EKF plots illustrate key parameters such as tether length, tether force, and the kite's vertical velocity (z-axis). When the spectrogram is synchronized with the EKF data, a clear pattern emerges: generator noise consistently appears during periods of high tether tension—or high apparent wind velocity—just before the kite begins to ascend. This correlation reinforces the earlier interpretation that increased generator RPM occurs during energy production phases.

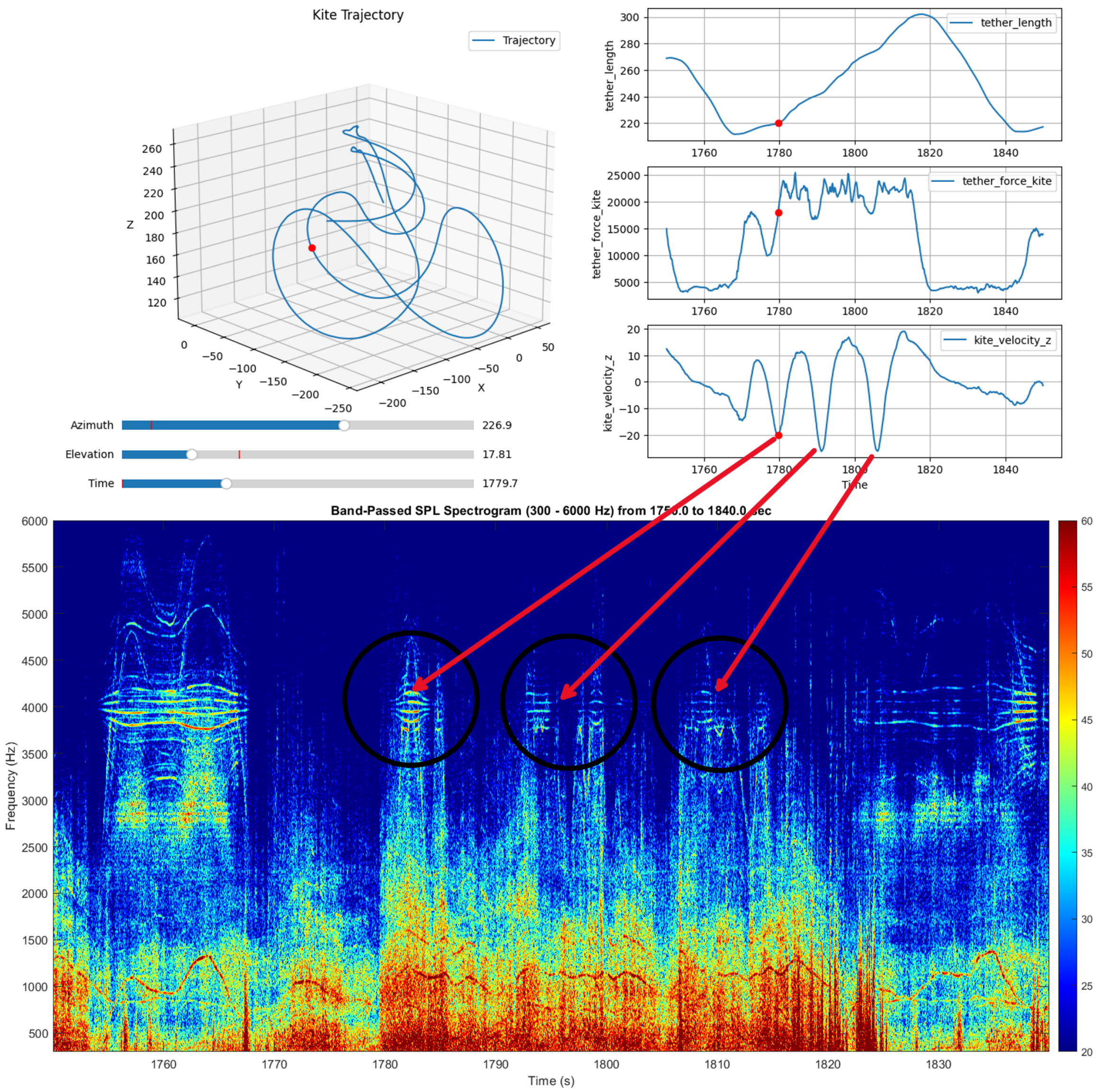

Figure 9.6: EKF trajectory analysis synchronized with spectral content. Red arrows indicate periods of fast generator operation during the power cycle, corresponding to high tether forces and gains in altitude after a turn made by the kite.

These operational phases are governed by the control algorithm and are illustrated in Figure 9.6. Red arrows highlight the moments where generator noise correlates with increased tether forces. For the purposes of spectral analysis, it is crucial to exclude these intervals, as the acoustic data during winch or generator activity is significantly affected by mechanical noise from the rotating drum. This interference can mask or distort the aeroacoustic signals of interest.

In the lower frequency range of the spectrum, additional noise components can be analyzed with greater clarity. By applying a band-pass filter limited to the range of 300–3500 Hz, harmonic noise generated by the turbine blades becomes more distinguishable. It is particularly interesting to observe how the frequencies of these harmonics vary in relation to the kite's flight speed. In some instances, up to eight harmonics can be identified. These harmonics correspond to integer multiples of the blade passing frequency (BPF), which itself is determined by the number of turbine blades and the rotational speed of the rotor. Since the RPM is influenced by the apparent wind speed, which varies with the kite's altitude and velocity, changes in the harmonic frequencies can be directly correlated with changes in flight dynamics.

This relationship is illustrated in Figure 9.7. The right-hand side of the figure provides a zoomed-in, five-second segment of the spectrogram highlighted by the arrow, where the harmonic structure is more clearly visible. The white circles mark the harmonics generated by the turbine, demonstrating that they are indeed spaced at regular intervals as multiples of the BPF.

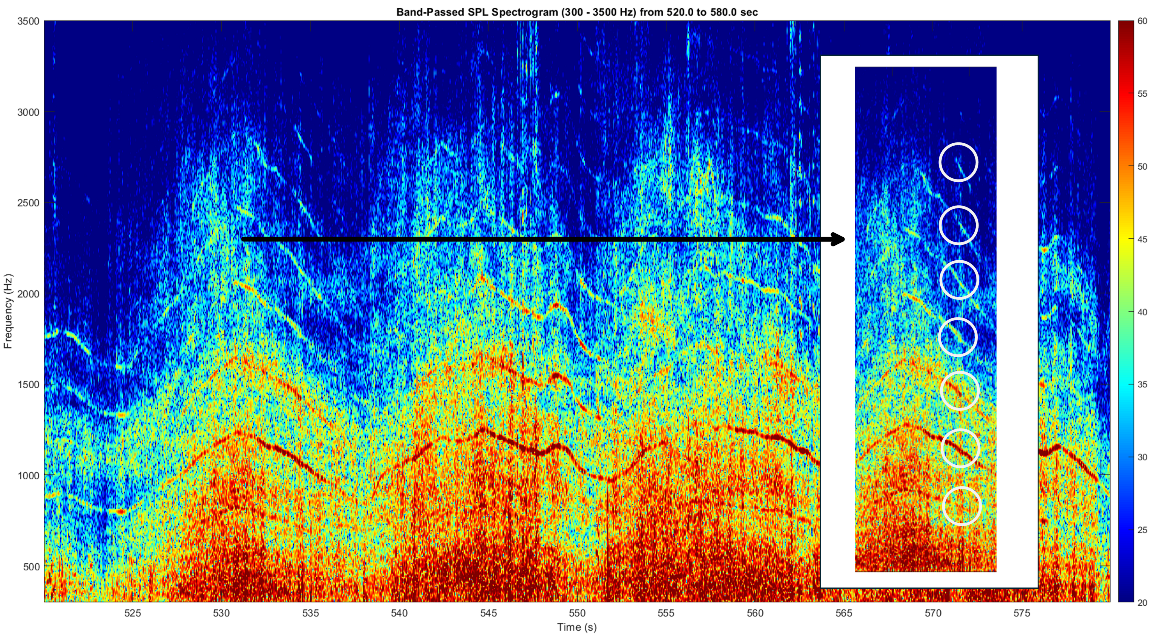

Figure 9.7: Spectrogram highlighting harmonic noise from the turbine. The zoomed-in section on the right shows tonal components, marked with white circles, that are multiples of the blade passing frequency (BPF).

From the spectrogram in Figure 9.7, the harmonic frequencies of the turbine noise can be extracted. At approximately 532 seconds, the harmonics appear at 800 Hz, 1200 Hz, 1600 Hz, and higher-order multiples of 400 Hz. Considering the turbine has four blades, this suggests a blade passing frequency (BPF) of 400 Hz, implying a rotor speed of 100 Hz, or approximately 6000 RPM. This estimation can be validated by examining the frequency spectrum extracted at the 532-second mark. The apparent wind speed was extracted from the EKF data and was found to be approximately 27.5 m/s at this instance of time. Other frequency peaks are observed in the analysis, such as those around 1000 Hz and 1300 Hz. These noises are believed to be caused by vortex shedding noise resulting from the flow around the tether or bridle lines, which will be investigated in the next section.

A key challenge in extracting this information lies in the trade-off between time and frequency resolution, governed by the chosen window duration. A longer window provides finer frequency resolution due to more sample points and reduced zero-padding. However, since the turbine sound is non-stationary and the rotational speed changes rapidly, longer windows tend to blur or smear the harmonic peaks. Conversely, shorter windows capture temporal changes better but at the cost of reduced frequency detail.

If the window duration is carefully selected during a time segment with minimal apparent wind speed variation, both time and frequency content can be reasonably preserved. Figure 9.8 illustrates this trade-off by comparing two FFT analyses centered around 532 seconds: one using a window duration of 0.1 s and the other with 1 s. In the first case (Figure 9.8a), the frequency resolution is approximately 10 Hz, with noticeable zero-padding. In contrast, Figure 9.8b achieves a 1 Hz resolution, clearly revealing additional harmonic peaks. Notably, harmonics around 400 Hz (the BPF) and 2400 Hz are difficult to distinguish in the shorter window but become more prominent in the longer one.

The same procedure was repeated multiple times to verify the reliability of the results and the performance of the microphone used in the experiments. The spectrogram and spectrum analysis conducted at the 365-second mark are illustrated in Figure 9.9, utilizing a time window of 0.5 seconds.

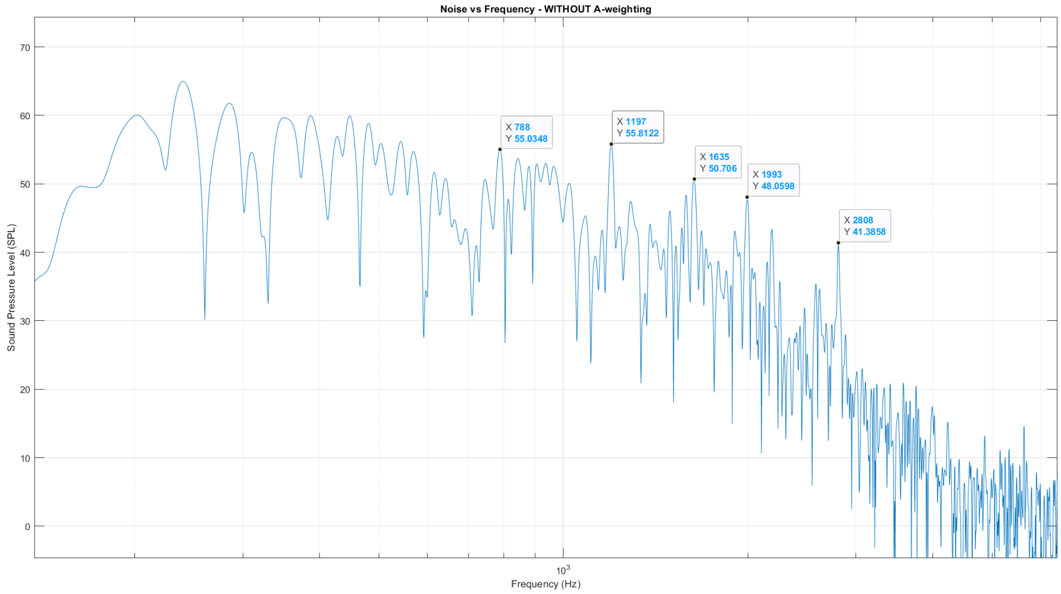

(a) Spectrum around 532 s with a window duration of 0.1 s. Resolution is limited (10 Hz) and some harmonic peaks are less visible due to zero-padding.

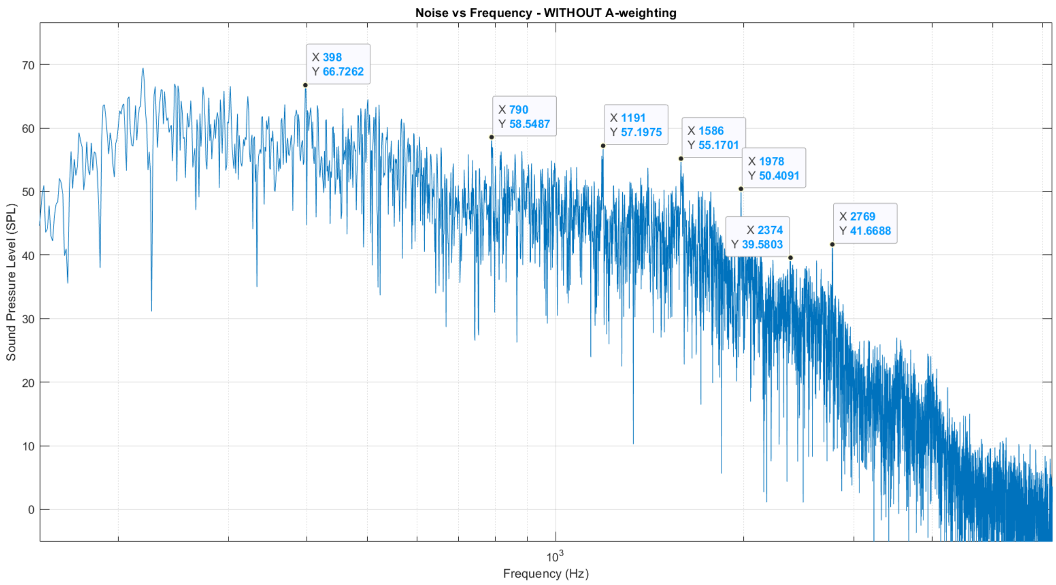

(b) Spectrum around 532 s with a window duration of 1 s. Higher resolution (1 Hz) enables clearer identification of multiple harmonics including the BPF.

Figure 9.8: Comparison of frequency spectra extracted at 532 seconds using different window durations. The longer window provides improved frequency resolution, making turbine harmonics more visible.

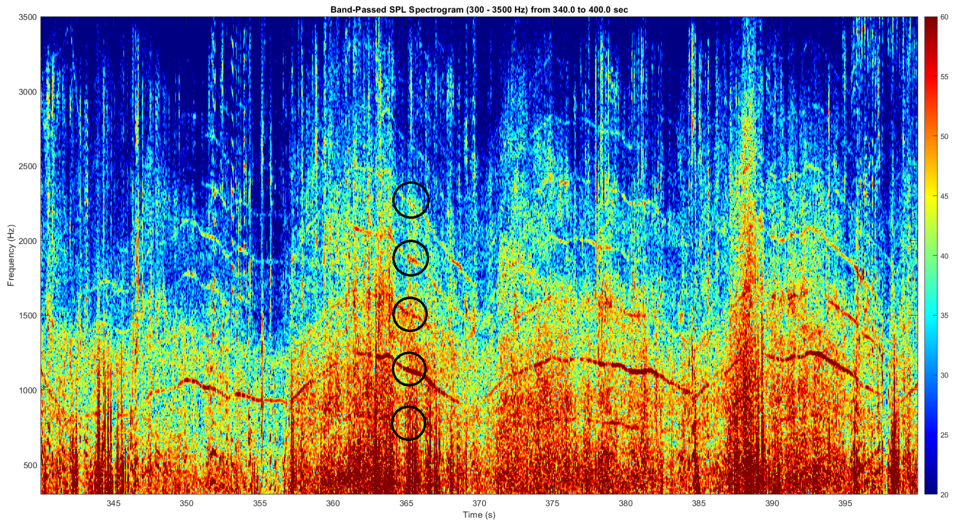

(a) Spectrogram of the system at second 365, showing identifiable harmonic frequencies of the turbine.

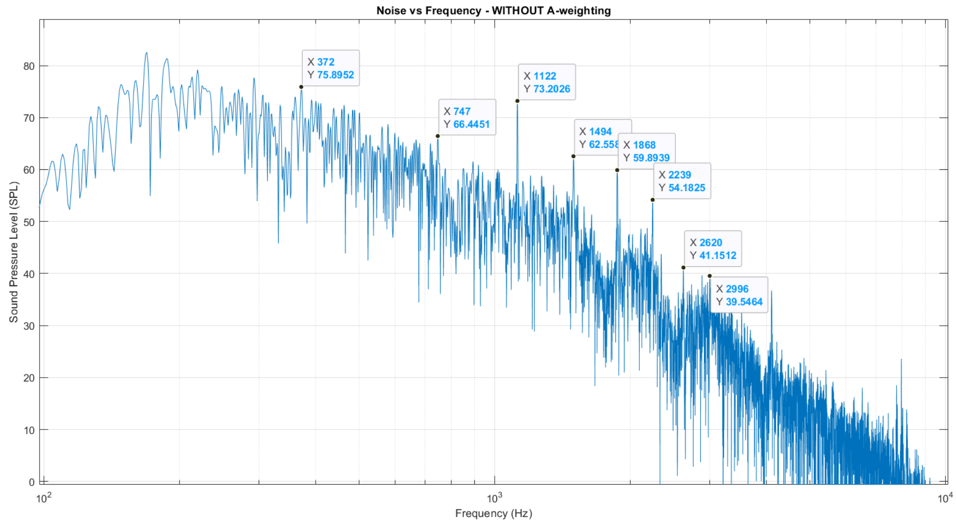

(b) Detailed spectrum of the system at second 365 with highlighted turbine harmonics.

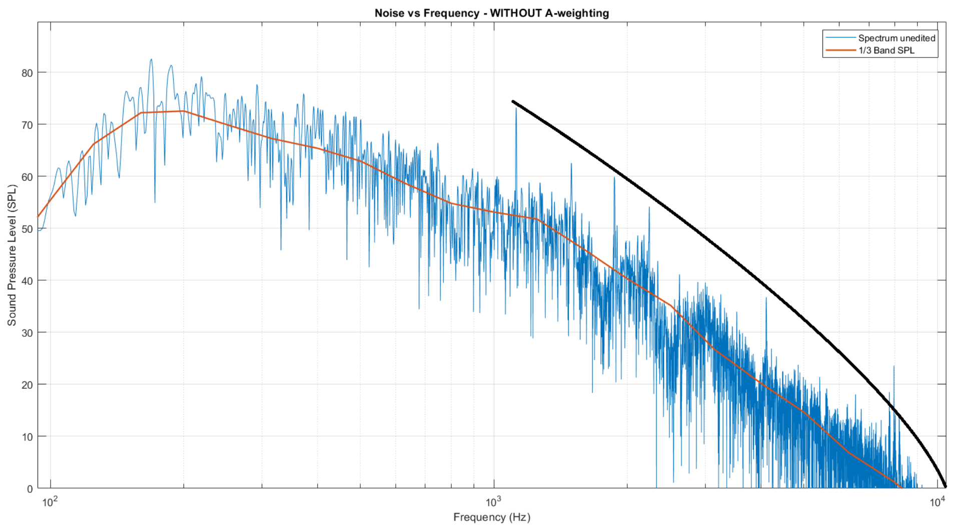

(c) Spectrum showing the turbine harmonics trend and the 1/3 band calculated SPL, with the black curve showing the decreasing trend of tonal peaks.

Figure 9.9: A compilation of figures showing various aspects of noise analysis at second 365.

In the spectrogram, black circles highlight the harmonics of the turbine, which remain identifiable despite some difficulties in recognition at higher frequencies. Based on the spectrum analysis depicted in Figure 9.9, the Blade Pass Frequency (BPF) was determined to be 374 Hz, corresponding to a turbine speed of 5610 RPM. The analysis shows clear peaks at higher order multiples of 374 up to 8×BPF, demonstrating minimal error and confirming the robustness of the method. The apparent flight velocity at this instance of time is 25.4 m/s obtained from the EKF. Figure 9.9c shows the decreasing trend of the turbine harmonics peaks with the black line, as expected and seen in the prediction code as well. The red line in the graph shows the 1/3 octave band SPL calculated, which can be interpreted as broadband noise from the kite and turbine. The remaining peaks observed in the spectrum analysis, while not as prominent as the harmonic peaks of the turbine, are likely to originate from the vortex shedding noise of tether or bridle lines.

The advance ratio of the turbine was not known. Thus, exploring this parameter through acoustic analysis was deemed necessary. It is hypothesized that there is a nearly linear relationship between the Blade Pass Frequency (BPF) and the apparent wind velocity of the kite. The spectrum was meticulously analyzed at multiple temporal intervals to consistently extract the BPF. Subsequently, the apparent wind speed was determined using data from the synchronized Extended Kalman Filter (EKF). These data points were graphically represented and subjected to linear regression to ascertain the relationship, as illustrated in Figure 9.10. The resulting linear model will serve as a crucial input for the aeroacoustic modeling of the kite, aiding in the understanding of the harmonic noises of the turbine.

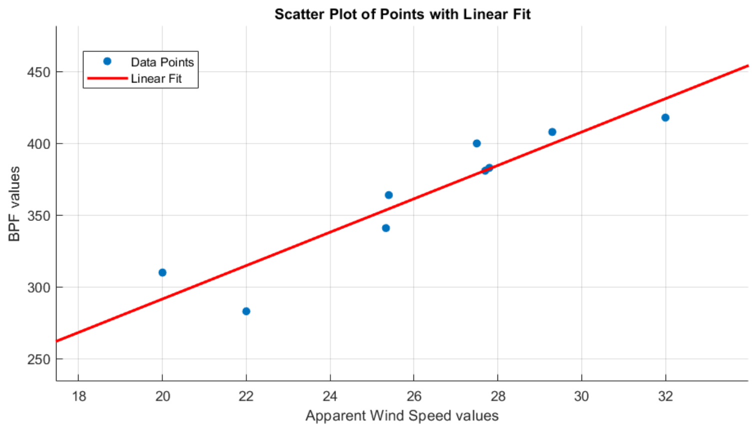

Figure 9.10: Fitted linear relationship between Blade Passing Frequency and apparent wind velocity, utilized for estimating the advance ratio in aeroacoustic modeling.

9.3. VALIDATION OF THE AEROACOUSTIC PREDICTION MODEL

For the validation of the results, specific moments during the test flight were selected, and all relevant data from the Extended Kalman Filter (EKF) were extracted to serve as input for the prediction model. The main criterion for choosing this validation moment was based on the quality of the video/audio recordings. Due to the use of a non-dedicated microphone, the audio is occasionally muffled, and the resulting spectrum may not be entirely accurate.

Furthermore, the sensitivity characteristics of the built-in microphones of the GoPro® camera are unknown, as no official datasheet is publicly available. As a result, it is not possible to determine the absolute value of the Sound Pressure Level (SPL) from the recordings. Consequently, the comparison between the experimental data and the simulation results is purely relative—it can indicate whether the trend is captured correctly, but not whether the predicted SPL values are quantitatively accurate. Calibration between the GoPro® spectrum and the simulation was performed using a linear gain, aligning the harmonic with the highest SPL and effectively bringing the overall spectra into close agreement.

VALIDATION AT HIGH APPARENT WIND SPEED

Multiple validation cases were conducted, but this section presents two representative scenarios: one at a higher kite speed and turbine RPM, and another at lower values. The first validation uses data from the

629th second of the flight, during which the kite executes a broad turn from higher altitude, reaching a high apparent wind speed of 30.7 m/s at an angle of attack of 9.5°. This maneuver is illustrated in Figure 9.11.

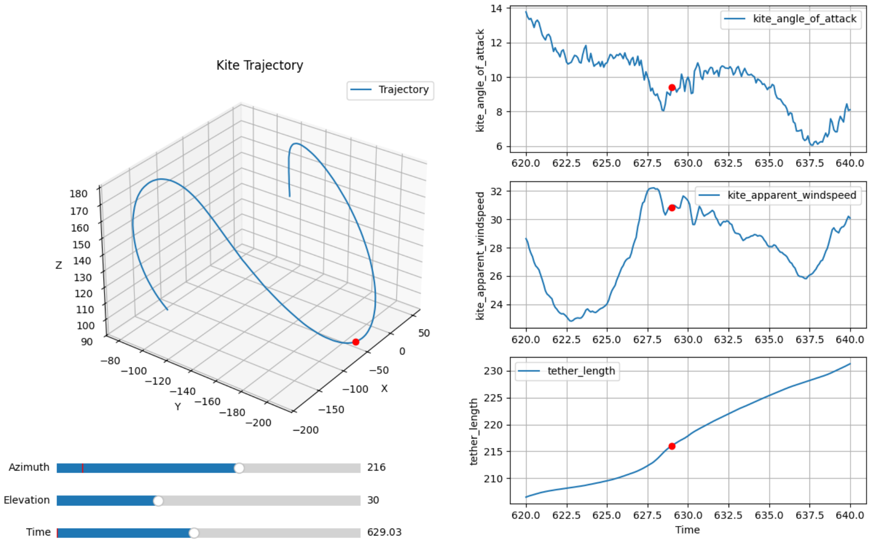

Figure 9.11: Kite maneuver during second 629 visualized with the EKF of Cayon et al. [71, 85], used for first validation.

The above parameters, along with the kite's position and tether length, were fed into the Aeroacoustic Prediction Framework. However, upon comparing the experimental spectrum with the prediction output, a frequency mismatch in the turbine's harmonic noise was detected. Further investigation revealed that the turbine's Blade Passing Frequency (BPF) differed from the predicted value. While the linear relationship between apparent wind speed and BPF generally holds, in this instance, the turbine was rotating slightly slower than expected, yielding a BPF of 406 Hz.

To address this, the actual BPF value was directly input into the solver to verify its behavior. With this adjustment, the prediction results aligned significantly better with the experimental data, particularly across most of the frequency spectrum, as illustrated in Figure 9.12.

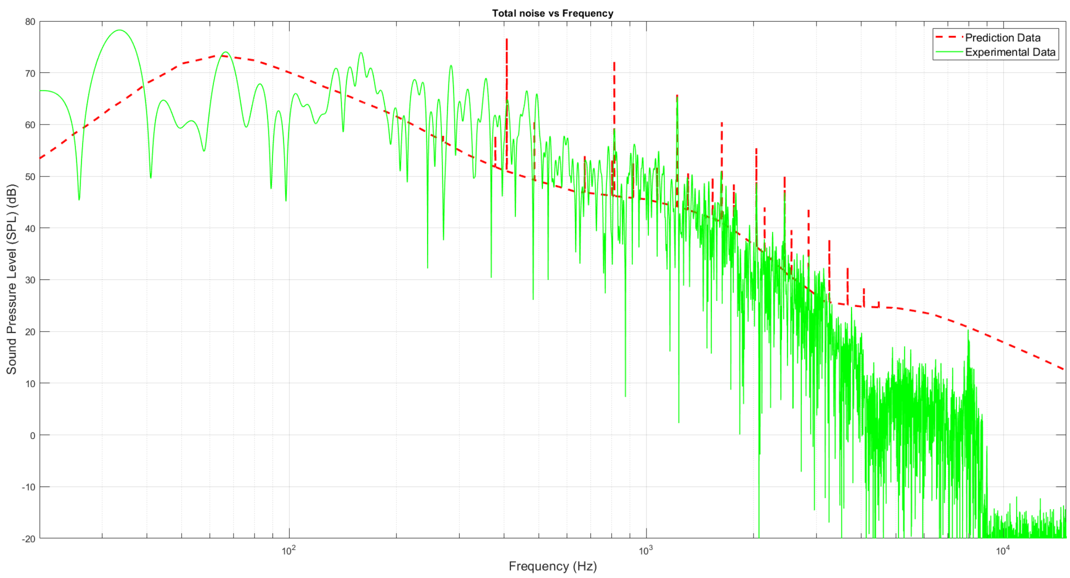

Figure 9.12: Comparison between predicted and experimental spectrum at second 629 of test-flight.

Figure 9.12 shows that up to approximately 4–5 kHz, the predicted spectrum closely matches the experimental data. The overall decreasing trend and characteristic curvature, mainly driven by broadband noise components, are well captured. Tonal noise frequencies from the turbine now align perfectly thanks to the corrected BPF input. The third harmonic, in particular, is accurately matched in SPL, while higher harmonics are present but slightly overestimated. However, a notable discrepancy appears in the first two harmonics, which are not clearly visible in the experimental spectrum, even though they are expected to be the most dominant. The underlying reasons for this discrepancy will be further discussed in Section 9.4. A more detailed view of the harmonics is provided in Figure 9.13, where turbine blade harmonics are labeled.

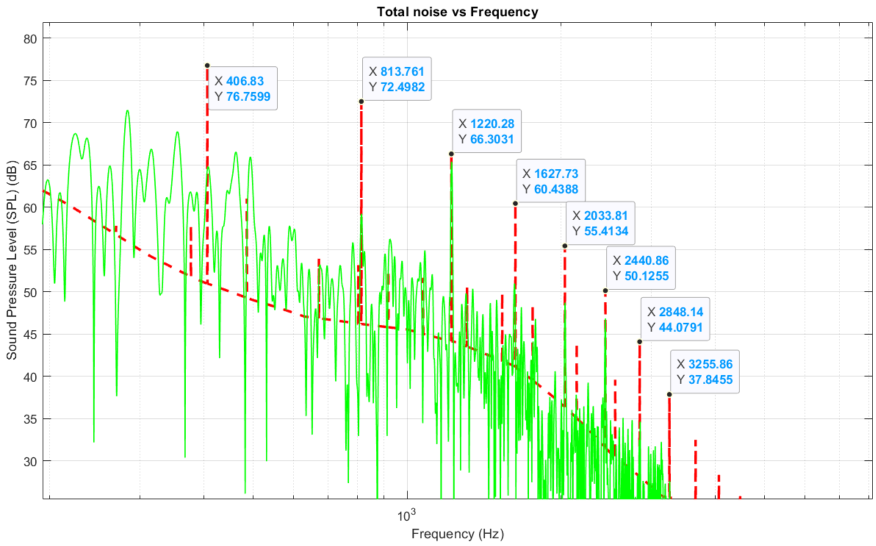

Figure 9.13: Detailed harmonic comparison between experimental and predicted data at second 629.

Another important aspect of the aeroacoustic environment is the noise generated by vortex shedding (VS) around the tether and bridle lines. Compared to other sources, their contribution appears relatively minor. The VS noise along the tether is predicted to be lower than the broadband noise from the kite. Only the faster-moving sections of the tether show marginal relevance. As for the bridle lines, most predicted VS noise peaks are identifiable in the simulation spectrum, though their overall contribution remains modest, with SPL levels just slightly higher than the broadband noise from other components.

Looking again at Figure 9.13, the predicted VS frequencies for the bridle lines correspond to noticeable peaks in the experimental data, particularly in the 800–1500 Hz range. This suggests that while the overall impact is limited, certain local resonances are captured by the simulation. A comprehensive breakdown of the noise contributions from all components, as calculated by the Aeroacoustic Prediction Framework, is shown in Figure 9.14.

VALIDATION AT LOW APPARENT WIND SPEED

The second validation was carried out using the audio analysis data recorded at the 464th second of the test flight. At this point, the kite was climbing in altitude in preparation for a loop. Due to this ascent, its speed was relatively low. Unlike the first validation, which examined a high-speed scenario, this case was chosen to represent the lower bound condition—where both the kite and turbine were operating at reduced speeds. Specifically, the kite reached an apparent wind velocity of only 20.6 m/s, and the corresponding turbine Blade Passing Frequency (BPF) was measured at 320 Hz. Interestingly, the angle of attack (AoA) of the kite during this instance was 10.7°, which is even higher than the AoA during the high-speed case. This elevated AoA is typical during the traction phase of flight, where the kite performs figure-eight patterns and maintains a high aerodynamic loading.

A comparative analysis between the results obtained from the audio spectrum of the flight footage and those predicted by the Aeroacoustic Prediction Framework is shown in Figure 9.15. One of the key observations is the significant reduction in Sound Pressure Level (SPL) across most of the frequency range (by as much as 10 dB in certain regions) when compared to the high-speed case. The harmonic tones generated by

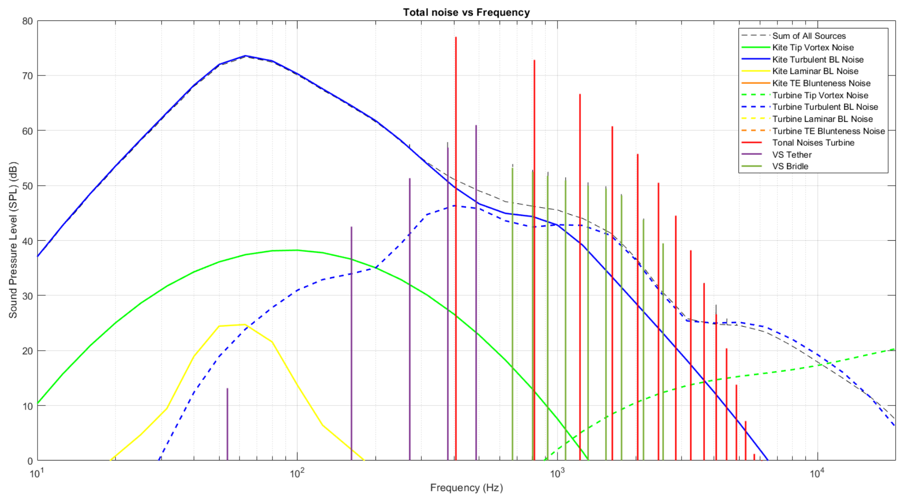

Figure 9.14: Breakdown of all noise sources as simulated by Aeroacoustic Prediction Framework (second 629).

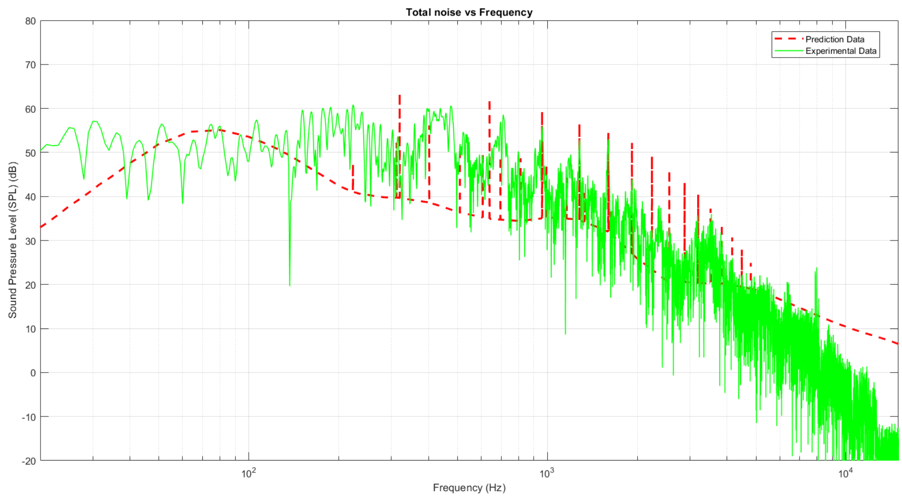

Figure 9.15: Overlay of predicted vs. experimental spectrum during low-speed kite climb (second 464).

the turbine are reasonably well captured starting from the third harmonic onward. The 3rd to 6th harmonics show accurate SPL values in the prediction, while higher harmonics tend to be slightly overestimated.

What stands out is that for the higher harmonics (specifically the 3rd to 7th), the predicted frequencies align well with a BPF of approximately 320 Hz, supporting the assumption of this operating condition. However, the first two harmonics appear inconsistent with the expected BPF. This anomaly could suggest that those particular tones originate from other sources (possibly environmental noise or wind interference) or that the analysis window was too broad, capturing extraneous frequencies not representative of the specific time instant simulated.

In this low-speed case, vortex shedding (VS) noise becomes more distinguishable. Peaks associated with VS around the bridle lines are visible in both the predicted and experimental spectra, particularly in the 800–1100 Hz range. The broadband noise predictions for both the kite and turbine exhibit some deviations from the measured data, yet they generally follow a similar trend up to about 5 kHz.

A more focused comparison, filtered between 200 and 5000 Hz, is presented in Figure 9.16, with side-by-side subfigures showcasing the predicted and experimental spectra.

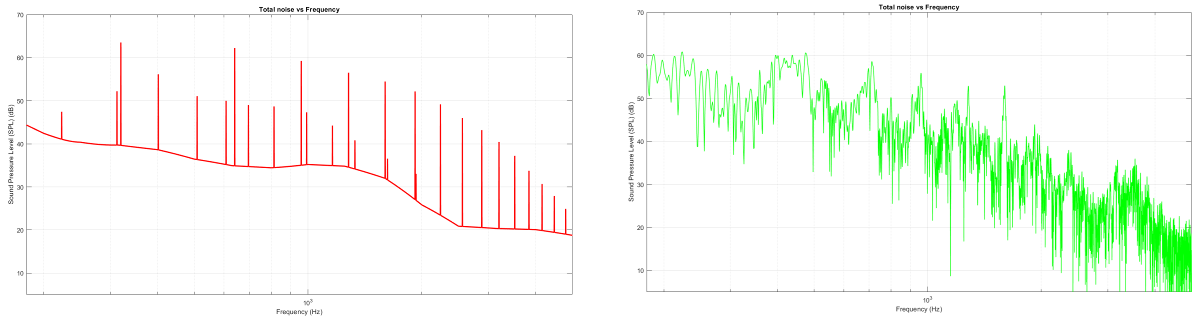

(a) Predicted spectrum (Aeroacoustic Prediction Framework)

(b) Experimental spectrum (Audio Analysis of GoPro® footage)

Figure 9.16: Side-by-side comparison between predicted and experimental acoustic spectra for the low-speed condition at second 464 (band-pass filter: 200–5000 Hz).

9.4. KEY OBSERVATIONS

9.4.1. FREQUENCY RESPONSE OF THE GOPRO® MICROPHONES

One of the main limitations of this study originates from the audio data obtained from the flight test recordings, which were used for comparison with the Aeroacoustic Prediction Framework. As previously discussed, the GoPro® camera is equipped with three built-in microphones positioned at the front, back, and one side of the camera. However, the specific datasheets for these microphones are not publicly disclosed by the manufacturer, making their technical specifications unknown. Consequently, it is not possible to calibrate the microphones based on their frequency sensitivity. This limitation means that absolute SPL values could not be derived during the audio analysis.

Further online research on relevant forums revealed three key pieces of information about the GoPro® microphones. First, several users noted that the microphones do not accurately capture sound above 5 kHz, suggesting the presence of a built-in low-pass filter. Second, it was reported that wind noise can cause the camera's software to muffle audio across the entire spectrum if strong wind is detected. Third, it was found that each of the three microphones appears to be sensitive to a specific range of frequencies. The camera's internal processing software then blends the signals from the three microphones to achieve clearer audio over a broader frequency range. In other words, it is believed that the GoPro® combines three audio streams, each focused on a specific frequency range.

To investigate this theory, a simple experimental test was performed. A MATLAB script was written to generate a sound signal with constant amplitude across a frequency sweep from 10 Hz to 20,000 Hz using the *chirp* function. Two types of frequency sweeps (logarithmic and linear) were generated over a 30-second duration. The resulting spectrograms of these sounds are shown in Figure 9.17, with the red regions representing the generated signals (note that the SPL values in the heatmaps are not scaled and, therefore, not representative).

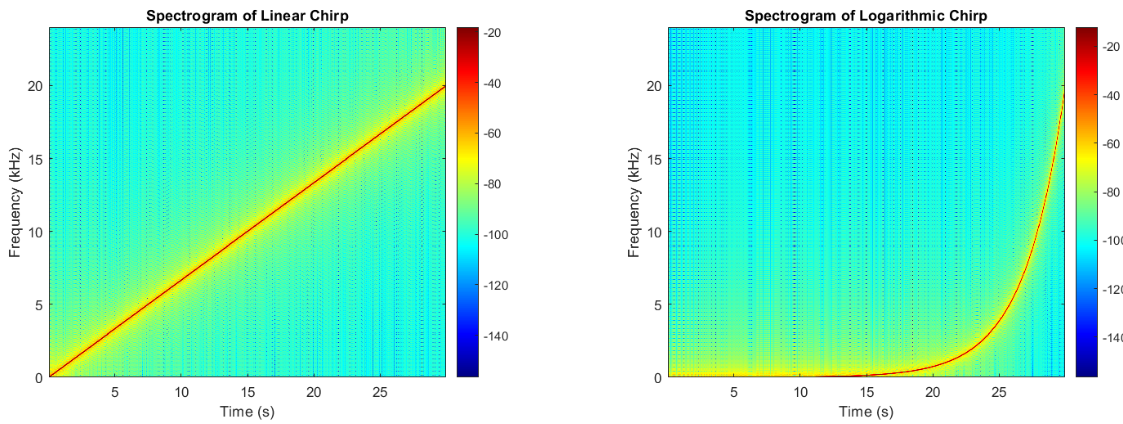

(a) Spectrogram of a linearly increasing frequency chirp.

(b) Spectrogram of a logarithmically increasing frequency chirp.

Figure 9.17: Spectrograms of generated chirp signals with constant amplitude over 30 seconds.

The generated chirp signal was then exported as a *.wav* file and played through a JBL® Boombox 3 speaker, which claims to have a flat frequency response over the human-audible range. The playback was recorded using a personal GoPro® camera inside a high-insulation acoustic enclosure, similar to the design shown in Figure 9.18. The camera was positioned approximately 1 meter from the speaker. A spectral analysis was then performed on the recorded audio, as shown in Figure 9.19.

While the test setup was improvised and a professional conclusion cannot be deduced directly from it, some insights can still be drawn. The JBL® speaker was not independently verified for linearity across the spectrum, and the enclosure, although lined with sound-absorbing foam, could introduce resonances or frequency shifts. Despite these limitations, the recorded frequency response clearly displays three distinct bumps, which aligns well with the information found in online sources regarding GoPro® microphone behavior.

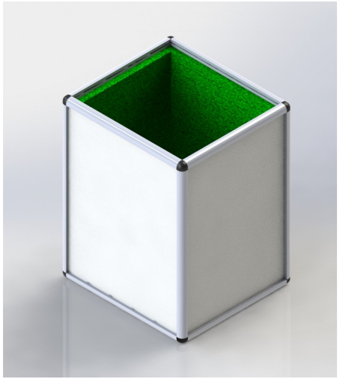

Figure 9.18: Sound enclosure used for the test.

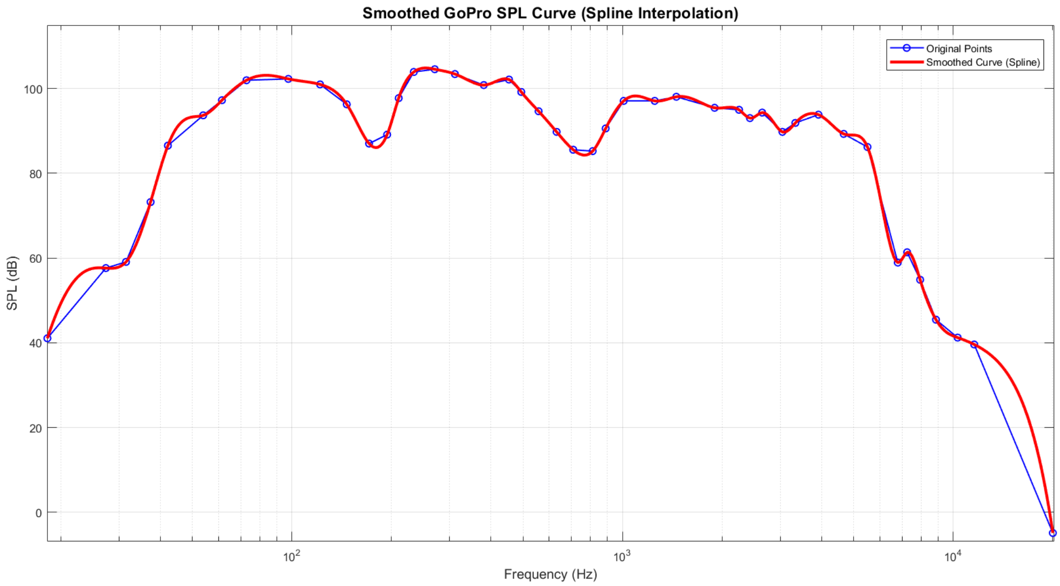

Figure 9.19: Spectral analysis of the recorded chirp using the GoPro® microphone.

CONCLUSIONS AFTER GOPRO® TEST

The test was conducted to explore how the GoPro® audio recordings might influence the experimental results. The built-in microphones appear to combine three audio streams, each sensitive to different frequency ranges. This processing creates visible bumps in the recorded spectrum, which can influence the accuracy of the comparison with simulation results—particularly in regions where microphone overlays occur. For example, around 700–1000 Hz, where the second harmonic of the turbine is expected, the combined response may distort or suppress relevant frequency content.

Furthermore, the microphones exhibit significantly reduced sensitivity above 5 kHz, a limitation that was clearly reflected in the audio analysis of the experimental data. In Figure 9.12, a good agreement is observed between the simulated and experimental spectra up to approximately 5 kHz. Beyond this point, the recorded SPL drops rapidly, which may explain the mismatch in the higher frequency range.

Although not directly tested using the presented setup, it was observed during various flight instances that the recorded audio was heavily suppressed when wind noise was prominent. This behavior is presumably due to the GoPro® software dynamically suppressing loud wind sounds to protect the microphones or improve playback clarity. In these situations, extracting useful spectral information becomes nearly impossible. Given that wind noise was present throughout most of the flight testing, it is likely that some degree of spectral suppression was applied across the entire recording duration, potentially affecting the accuracy of the experimental spectrum.

9.4.2. ATTENUATION OF LOW-FREQUENCY HARMONICS DUE TO DUCTING EFFECTS

During the validation process, it was observed that while the first two harmonics of the turbine are accurately predicted by the Aeroacoustic Prediction Framework, they are either significantly attenuated or completely missing in the GoPro® audio recordings. One possible explanation, as discussed in Section 9.4.1, is the frequency response characteristics of the camera itself. However, this section explores an additional contributing factor: the acoustic attenuation caused by the duct surrounding the ram-air turbine.

A second GoPro® camera was mounted onboard the system with a direct view of the turbine and kite. As shown in Figure 9.20, the turbine is encased in a protective duct made of rigid foam. Measurements of the 3D model of this duct indicate a radius of 232 mm and a chord of approximately 221 mm. During typical crosswind flight, the turbine is not directly facing the ground-based observer and camera, but is oriented at an angle of about 90°, with the duct positioned between the turbine and the microphone. This geometry introduces both physical and acoustic shielding.

Figure 9.20: Onboard GoPro® view of the ram-air turbine housed within a rigid foam duct during crosswind flight.

Malgoezar et al. [93] conducted an experimental study at TU Delft on the acoustic behavior of ducted propellers for unmanned aerial vehicles (UAVs). Their findings showed that while the duct increases broadband noise levels, it significantly reduces the amplitude of the first few tonal harmonics. Similarly, Simon et al. [94] investigated noise characteristics of a ducted propeller in hover conditions. Their test setup, featuring a blade passing frequency of around 400 Hz—very similar to the one in the current study—demonstrated that the duct reduces overall SPL and that optimal centering of the propeller within the duct can enhance destructive interference between upstream and downstream radiation.

The first two harmonics missing from the GoPro® far-field recordings are at approximately 400 Hz and 800 Hz. The corresponding wavelengths for these frequencies are 0.85 m and 0.42 m, respectively, based on the speed of sound. According to Groeneweg et al. [32], a general rule of thumb is that for efficient acoustic radiation, a duct's characteristic dimension should exceed one-quarter of the wavelength. Given that the duct chord is only around 0.2 m, this suggests that these lower-frequency harmonics may primarily diffract inside the duct rather than propagate outward effectively. This supports the theory that the duct acts as an acoustic filter for lower frequencies.

To verify this hypothesis, the onboard GoPro®, positioned near the turbine, was used to capture the direct sound without the same degree of shielding. Figure 9.21 shows the spectrogram of this recording, where the harmonics are more clearly visible. Furthermore, Figure 9.22 presents a detailed spectral analysis with the first 10 harmonics labeled. It is evident that, unlike in the far-field analysis, the first two harmonics are present and clearly distinguishable with significant SPL levels.

These findings strongly indicate that the duct reduces the efficiency of harmonic noise radiation into the far field for two reasons: (1) it acts as a physical barrier between the observer and the turbine during crosswind flight, and (2) it acoustically suppresses the radiation of low-frequency tones due to geometric cutoff effects.

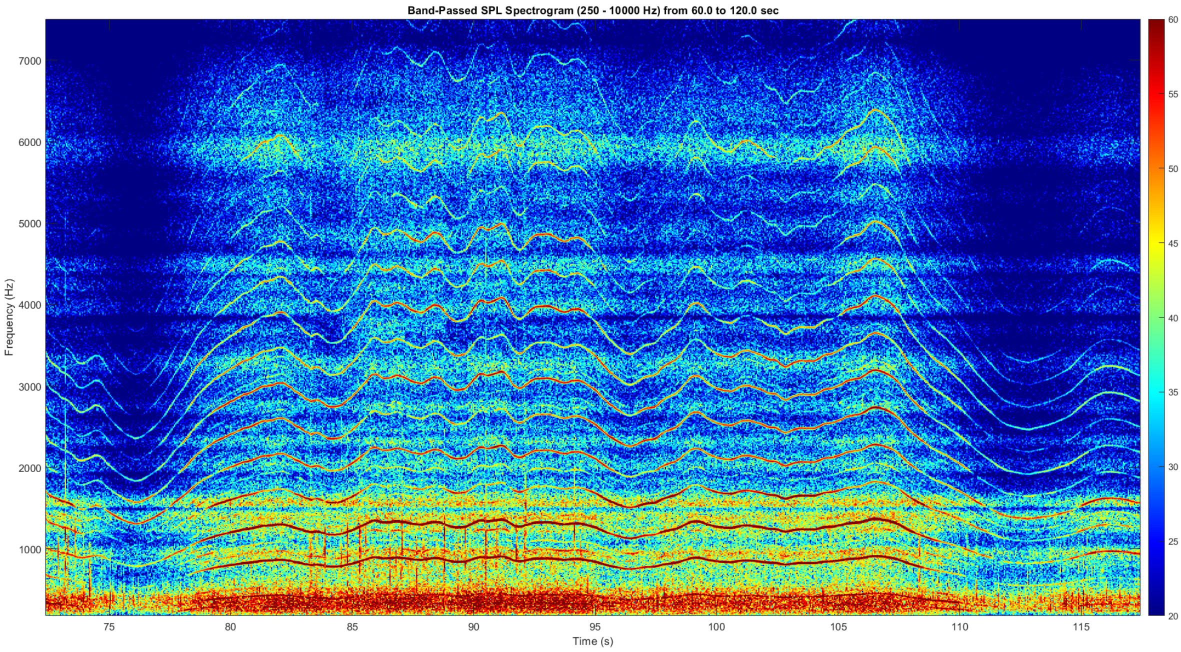

Figure 9.21: Spectrogram of turbine noise recorded by the onboard GoPro®, showing clearly visible harmonics.

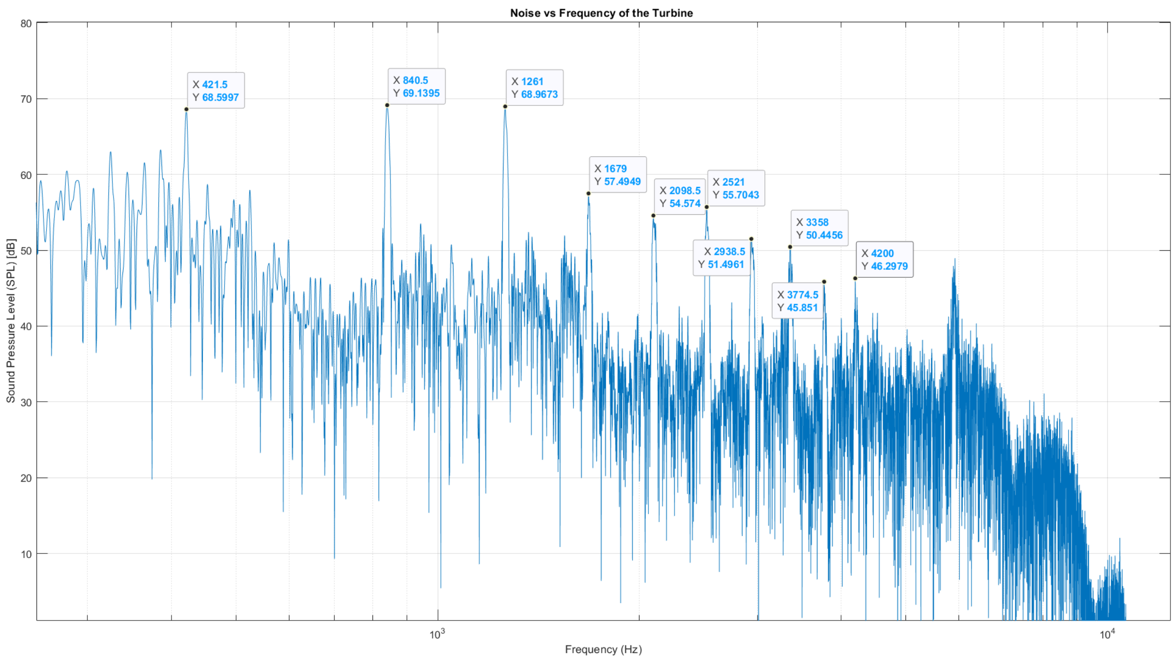

Figure 9.22: Spectrum of onboard audio recording, with the first 10 turbine harmonics labeled. The first two harmonics are clearly present.

10

Conclusions and Recommendations

10.1. Conclusions

This thesis developed and validated a low-fidelity Aeroacoustic Prediction Framework for airborne wind energy systems (AWES), using the Kitepower system as a case study. By applying established analytical models to each airborne component—the LEI kite, ram-air turbine, tether, and bridle lines—and validating the outputs against audio recordings, several key findings were established.

The framework reliably captured the dominant noise mechanisms observed during flight. For the kite and turbine blades, turbulent boundary layer trailing-edge (TBL-TE) noise was identified as the primary airfoil self-noise source. Laminar vortex-shedding, tip vortex, and trailing-edge bluntness noise were predicted to be negligible given the system's geometry and operational Reynolds numbers. For the tether and bridle lines, vortex-shedding noise was characterized using Strouhal-based formulations, with frequency content and amplitude matching expected patterns.

For the onboard ram-air turbine, tonal emissions at blade-passing frequencies and their harmonics were accurately reproduced using Hanson's frequency-domain model. Predicted blade-passing frequency and higher harmonics closely matched those observed in the recorded data of the test flight. However, in many cases the first two harmonics were not visible in the frequency spectrum of the audio recordings. This was attributed to the ducting effect, which shields the turbine and suppresses efficient radiation of lower frequencies. It was also observed that the turbine angle of attack is relatively high, especially near the hub, suggesting that aerodynamic optimization may be needed to reduce noise emissions.

Validation with experimental data confirmed that even without absolute SPL calibration, the model replicated spectral shapes, tonal peaks, and overall noise trends with good agreement, particularly up to 5 kHz. This demonstrates the feasibility of using low-order analytical models for early-stage acoustic assessments of AWES. Discrepancies in amplitude, especially at high frequencies, were attributed to propagation simplifications and limitations of the GoPro® camera, which appears to apply a software-based low-pass filter.

Beyond individual model performance, the integration of geometric extraction, aerodynamic analysis via XFOIL, dynamic flight data through EKF, and full signal processing enabled an end-to-end pipeline. The 2D XFOIL results for boundary layer parameters, lift, and drag coefficients were within realistic ranges upon verification with literature. Incorporating EKF data improved the fidelity of the solver by providing the precise flight states during testing.

This work highlights that even with limited experimental resources—such as non-professional microphones—meaningful acoustic predictions can be achieved. The methodology provides a solid basis for assessing the acoustic impact of AWES in populated or noise-sensitive areas. With increasing attention to social acceptance and environmental regulation, this type of simulation tool can assist both developers and policymakers in evaluating noise performance during early design stages or certification processes. Additionally, it offers potential for future applications such as component optimization, operational noise tracking, and psychoacoustic evaluation.

In summary, this thesis shows that low-fidelity, physics-based aeroacoustic models can effectively capture the key acoustic characteristics of AWES, such as the Kitepower system. The proposed framework not only demonstrates technical feasibility, but also serves as a practical tool for further development, validation, and responsible deployment of airborne wind energy technologies.

10.2. RECOMMENDATIONS AND FUTURE WORK

Building upon the insights and limitations of this study, several directions are proposed to enhance both the predictive accuracy and the experimental validation of the aeroacoustic framework:

- **Adoption of Calibrated Microphones and Improved Measurement Setup**
  Future recordings should rely on calibrated measurement-grade microphones with well-characterized frequency response curves. The use of professional wind caps or windscreens is strongly recommended to reduce wind-induced distortion, particularly at low frequencies. Additionally, conducting measurements at greater distances from the ground station would help assess whether mechanical or electrical noises—such as those generated by the winch—should be formally included in the noise model. This setup could also help to mitigate or better isolate the influence of the turbine duct, whose acoustic shielding and cut-off behavior vary with observer position and angle of incidence. The absence of calibrated equipment and proximity effects in the current study limit the ability to determine absolute SPL values and prevent direct comparison with regulatory thresholds.

- **Inclusion of Turbulent Inflow Noise and Trailing Edge Flutter of the Kite**
  The current framework does not account for noise contributions from turbulent inflow or TE flutter of the kite. Incorporating this mechanism could improve prediction accuracy, particularly in cases of high wind variability or aggressive flight maneuvers where unsteady inflow conditions are expected.

- **Refinement of Boundary Layer Inputs through CFD or Experimental Validation**
  Boundary layer displacement thickness was estimated using XFOIL under steady-state assumptions. To improve realism, these parameters could be refined and validated through high-fidelity computational fluid dynamics (CFD) simulations or direct experimental measurements, particularly in regions where separation or transition may occur.

- **Auralization and Psychoacoustic Testing**
  The framework outputs can be exported and later processed using auralization techniques to generate audio playback, enabling future psychoacoustic experiments and listener studies. This would support research on human perception, annoyance, and the social acceptance of AWES noise.

Once these improvements are implemented—particularly through the use of calibrated instrumentation and refined flow modeling—the aeroacoustic framework developed in this thesis has strong potential to support future psychoacoustic studies, regulatory assessments, and system-level optimization. By providing accurate, component-resolved noise predictions, it can contribute to a deeper understanding of human perception, annoyance thresholds, and environmental impact. As such, this work represents a meaningful step toward integrating acoustic performance as a core design criterion in the development of sustainable airborne wind technologies.

Bibliography

[1] International Energy Agency, *Net zero roadmap – a global pathway to keep the 1.5°c goal in reach,* https://iea.blob.core.windows.net/assets/9a698da4-4002-4e53-8ef3-631d8971bf84/NetZeroRoadmap_AGlobalPathwaytoKeepthe1.5CGoalinReach-2023Update.pdf (2023), 225 pp., accessed 13 April 2025.

[2] M. Schelbergen, P. C. Kalverla, R. Schmehl, and S. J. Watson, *Clustering wind profile shapes to estimate airborne wind energy production,* Wind Energy Science **5**, 1097 (2020).

[3] T. B. L. Energy, *Wind turbine efficiency: What you need to know,* https://lumifyenergy.com/blog/wind-turbine-efficiency/ (2023), accessed: 2025-04-13.

[4] C. Jensen, T. Panduro, and T. Lundhede, *The vindication of don quixote: The impact of noise and visual pollution from wind turbines,* Land Economics **90**, 668 (2014).

[5] S. Deshmukh, S. Bhattacharya, A. Jain, and A. R. Paul, *Wind turbine noise and its mitigation techniques: A review,* Energy Procedia **160**, 633 (2019), 2nd International Conference on Energy and Power, ICEP2018, 13–15 December 2018, Sydney, Australia.

[6] H. Schmidt, G. de Vries, R. J. Renes, and R. Schmehl, *The social acceptance of airborne wind energy: A literature review,* Energies **15** (2022), 10.3390/en15041384.

[7] A. Cherubini, A. Papini, R. Vertechy, and M. Fontana, *Airborne wind energy systems: A review of the technologies,* Renewable and Sustainable Energy Reviews **51**, 1461 (2015).

[8] R. Schmehl, ed., *Book of Abstracts - Airborne Wind Energy Conference 2015* (Delft University of Technology, Delft, The Netherlands, 2015) edited by Roland Schmehl, with editorial assistance from Roger Coenen and Pietro Faggiani.

[9] R. Schmehl, *Airborne wind energy: An introduction to an emerging technology,* (2019).

[10] R. van der Vlugt, J. Peschel, and R. Schmehl, *Design and experimental characterization of a pumping kite power system,* in *Airborne Wind Energy*, Green Energy and Technology, edited by U. Ahrens, M. Diehl, and R. Schmehl (Springer, Berlin, Heidelberg, 2013) Chap. 23, pp. 403–425.

[11] R. van der Vlugt, A. Bley, M. Noom, and R. Schmehl, *Quasi-steady model of a pumping kite power system,* Renewable Energy **131**, 83 (2019).

[12] N. Bouman, *Aeroacoustics of Airborne Wind Energy Systems,* Master's thesis, Faculty of Aerospace Engineering, Delft University of Technology (2023).

[13] M. L. Loyd, *Crosswind kite power (for large-scale wind power production),* Journal of Energy **4**, 106 (1980), https://doi.org/10.2514/3.48021 .

[14] S. Dunker, *Tether and bridle line drag in airborne wind energy applications,* in *Airborne Wind Energy: Advances in Technology Development and Research*, Green Energy and Technology, edited by R. Schmehl (Springer, 2019) Chap. 2, pp. 29–56.

[15] R. Bosman, V. Reid, M. Vlasblom, and P. Smeets, *Airborne wind energy tethers with high-modulus polyethylene fibers,* Airborne Wind Energy , 563 (2013).

[16] J. J. Oehler and R. Schmehl, *Aerodynamic characterization of a soft kite by in situ flow measurement,* Wind Energy Science **4**, 1 (2019).

[17] B. Van Den Kieboom, *Design and Noise Study of a Low-Drag Wind Turbine for Airborne Power Applications: A Numerical & Experimental Assessment,* Master's thesis, Faculty of Aerospace Engineering, Delft University of Technology (2017).

[18] U. Fechner, *A Methodology for the Design of Kite-Power Control Systems*, Ph.D. thesis, Delft University of Technology, Delft, Netherlands (2016).

[19] F. Friedl, *Fault-Tolerant Design of a Pumping Kite Power Flight Control System*, Master's thesis, Delft University of Technology (2015).

[20] R. Schmehl, *Airborne wind energy: An introduction to an emerging technology,* (2019).

[21] R. Schmehl, *Airborne wind energy ae4t40,* Lecture Notes, TU Delft (2024).

[22] M. Diehl, *Airborne wind energy: Basic concepts and physical foundations,* in *Airborne Wind Energy*, edited by U. Ahrens, M. Diehl, and R. Schmehl (Springer, Heidelberg, New York, Dordrecht, London, 2013) pp. 3–22.

[23] R. Leuthold, *Multiple-Wake Vortex Lattice Method for Membrane-Wing Kites*, Master's thesis, Delft University of Technology (2015).

[24] G. Müller and M. Möser, *Handbook of Engineering Acoustics*, edited by G. Müller and M. Möser (Springer, 2013) p. 702.

[25] S. Wagner, G. Guidati, and R. Bareiß, *Wind Turbine Noise*, 1st ed. (1996) p. 216.

[26] A. D. Pierce, *Acoustics: An Introduction to Its Physical Principles and Applications*, McGraw-Hill series in mechanical engineering (McGraw-Hill, United States, 1981).

[27] P. Dijkstra, *Rotor noise and aero-acoustic optimization of wind turbine airfoils*, Master's thesis, Delft University of Technology, Delft, The Netherlands (2015).

[28] D. A. Russell, J. P. Titlow, and Y.-J. Bemmen, *Acoustic monopoles, dipoles, and quadrupoles: An experiment revisited,* American Journal of Physics **67**, 660 (1999), https://pubs.aip.org/aapt/ajp/article-pdf/67/8/660/7528251/660_1_online.pdf .

[29] L. E. Kinsler, A. R. Frey, A. B. Coppens, and J. V. Sanders, *Fundamentals of Acoustics* (Wiley, New York, 1982) pp. 167–172.

[30] D. D. Reynolds, *Engineering Principles of Acoustics: Noise and Vibration Control* (Allyn and Bacon, Boston, 1981) pp. 531–594.

[31] D. Russel, *Acoustics and vibrations,* `https://www.acs.psu.edu/drussell/Demos/rad2/mdq.html` (2001).

[32] B. M. NASA, D. B. Hanson, and R. K. Amiet, *Aeroacoustics of Flight Vehicles: Theory and Practice, Volume 1: Noise Sources*, Tech. Rep. NASA-RP-1258, Vol. 1, WRDC Technical Report 90-3052 (NASA, United States, 1991) prepared for US Army Aviation Systems Command, Aviation RT Activity.

[33] M. Haddaoui, *Development of a Propeller Source Noise Model*, Master's thesis, Delft University of Technology, Delft, The Netherlands (2019).

[34] B. Marinus, *Multidisciplinary Optimization of Aircraft Propeller Blades*, Phd thesis, École Centrale de Lyon (2011).

[35] J. Pockelé, *Auralisation of Modelled Wind Turbine Noise for Psychoacoustic Listening Experiments: Development and Validation of the Wind Turbine Auralisation Tool WinTAur*, Master thesis, TU Delft (2023).

[36] F. Yunus, *Methodologies and Algorithms for Sound Propagation in Complex Environments with Application to Urban Air Mobility: A Ray Acoustics Approach*, Doctoral thesis, TU Delft (2023).

[37] M. Poessel, *Waves, motion and frequency: the doppler effect,* Einstein Online **05** (2011).

[38] I. O. for Standardisation (ISO), *Acoustics - Attenuation of Sound During Propagation Outdoors - Part 2: General Method of Calculation*, Tech. Rep. (International Standard ISO 9613-2, 1996).

[39] I. O. for Standardization (ISO), *Acoustics — Attenuation of sound during propagation outdoors — Part 2: Engineering method for the prediction of sound pressure levels outdoors*, Tech. Rep. (International Standard ISO 9613-2:2024, 2024).

[40] V. Salma, R. Ruiterkamp, M. Kruijff, M. M. van Paassen, and R. Schmehl, *Current and expected airspace regulations for airborne wind energy systems,* in *Airborne Wind Energy: Advances in Technology Development and Research*, Green Energy and Technology, edited by R. Schmehl (Springer, 2019) Chap. 29, pp. 703–720.

[41] R. voor Volksgezondheid en Milieu (RIVM), *Public focus on wind turbines and health,* RIVM Magazine (2021).

[42] I. van Kamp and G. P. van den Berg, *Health effects related to wind turbine sound: an update*, Tech. Rep. 2020-0150 (National Institute for Public Health and the Environment (RIVM), 2020).

[43] F. Fahy, *Foundations of Engineering Acoustics,* reprinted 2003, 2005 ed. (Elsevier Academic Press, San Diego, California, USA and London, UK, 2001) library of Congress Catalog Number: 00-103464. Institute of Sound and Vibration Research, University of Southampton, Southampton, UK.

[44] R. voor Ondernemend Nederland (RVO), *Geluidnormering windmolens,* (2018), accessed: 2025-02-14.

[45] E. Verheijen, J. Jabben, E. Schreurs, and K. B. Smith, *Impact of wind turbine noise in the netherlands,* Noise Health **13**, 459 (2011).

[46] H. Geleijns and M. Dijkstra, *Literatuuronderzoek laagfrequent geluid windturbines*, Tech. Rep. (LBP|SIGHT BV, 2013) accessed: 2025-02-14.

[47] A. Szücs, *Acoustic impact of airborne wind energy technology on the environment,* (2017).

[48] R. Amiet, *Acoustic radiation from an airfoil in a turbulent stream,* Journal of Sound and Vibration **41**, 407 (1975).

[49] R. Amiet, *Noise due to turbulent flow past a trailing edge,* Journal of Sound and Vibration **47**, 387 (1976).

[50] T. F. Brooks, S. Pope, and M. A. Marcolini, *Airfoil Self-Noise and Prediction*, Tech. Rep. 1218 (NASA, 1989).

[51] R. Parchen, *Progress report DRAW: a prediction scheme for trailing edge noise based on detailed boundary layer characteristics*, Progress Report (1998).

[52] D. HANSON, *Near field noise of high tip speed propellers in forward flight,* in *3rd Aeroacoustics Conference*.

[53] D. B. Hanson, *Helicoidal surface theory for harmonic noise of propellers in the far field,* AIAA Journal **18** (1980), 10.2514/3.50873.

[54] F. Yunus, E. Grande, D. Casalino, F. Avallone, and D. Ragni, *Efficient low-fidelity aeroacoustic permanence calculation of propellers,* Aerospace Science and Technology **123**, 107438 (2022).

[55] F. do N. Monteiro, D. Ragni, F. Avallone, and T. Sinnige, *Low-order acoustic prediction tool for estimating noise emissions from distributed propeller configurations,* in *AIAA AVIATION 2023 Forum*, https://arc.aiaa.org/doi/pdf/10.2514/6.2023-4180 .

[56] J. D. Blake, C. S. Thurman, N. S. Zawodny, and L. V. Lopes, *Broadband predictions of optimized proprotors in axial forward flight,* in *AIAA AVIATION 2023 Forum*, https://arc.aiaa.org/doi/pdf/10.2514/6.2023-4183 .

[57] J. H. Lienhard, *Synopsis of Lift, Drag, and Vortex Frequency Data for Rigid Circular Cylinders*, Tech. Rep. Bulletin 300 (Washington State University, Pullman, Washington, USA, 1966).

[58] R. Blevins, *Flow-Induced Vibrations - Second Edition* (Van Nostrand Reinhold, New York, 1990).

[59] R. Blevins, *Flow-induced Vibration* (Van Nostrand Reinhold Company, 1977).

[60] S. Goldstein, *Modern Developments in Fluid Dynamics, Vol. 2* (Dover Publications, 1938).

[61] R. King, *A review of vortex shedding research and its application,* Ocean Engineering **4**, 141 (1977).

[62] E. Naudascher and D. Rockwell, *Flow-Induced Vibrations: An Engineering Guide* (A. A. Balkema Publishers, Rotterdam, The Netherlands, 1994).

[63] S. Dunker, W. Meile, and G. Brenn, *Experiments in line vibration and associated drag for kites,* in *23rd AIAA Aerodynamic Decelerator Systems Technology Conference* (2015).

[64] M. M. Zdravkovich and P. W. Bearman, *Flow around circular cylinders—volume 1: Fundamentals,* Journal of Fluids Engineering **120**, 216 (1998), https://asmedigitalcollection.asme.org/fluidsengineering/article-pdf/120/1/216/5605743/216_1.pdf .

[65] E. L. Iglesias, D. J. Thompson, and M. G. Smith, *Experimental study of the aerodynamic noise radiated by cylinders with different cross-sections and yaw angles,* Journal of Sound and Vibration **361**, 108 (2016).

[66] L. Saur, J. Riedel, S. Dunker, and S. Becker, *Experimental investigation of flow-induced sound of kite lines,* Acta Acustica **7**, 13 (2023).

[67] T. Jung, *Wind tunnel study of drag of various rope designs,* in *27th AIAA Applied Aerodynamics Conference* (2009).

[68] K. Blake, *Flow-Induced Sound and Vibration, Volume I: General Concepts and Elementary Sources*, Vol. 1 (Academic Press, 1988) pp. 1397–1398, iSSN 83(1).

[69] M. E. Goldstein, *Aeroacoustics* (McGraw-Hill International Book Co., New York, 1976) p. 305.

[70] J. E. F. Williams and D. L. Hawkings, *Sound generation by turbulence and surfaces in arbitrary motion,* Philosophical Transactions of the Royal Society A: Mathematical, Physical and Engineering Sciences **264**, 321 (1969).

[71] O. Cayon, S. Watson, and R. Schmehl, *Kite as a sensor: Wind and state estimation in tethered flying systems,* Wind Energy Science Discussions **2025**, 1 (2025).

[72] M. Drela, *XFOIL: An Analysis and Design System for Low Reynolds Number Airfoils*, Tech. Rep. (Massachusetts Institute of Technology, 1989).

[73] N. Curle and M. J. Lighthill, *The influence of solid boundaries upon aerodynamic sound,* Proceedings of the Royal Society of London. Series A. Mathematical and Physical Sciences **231**, 505 (1955), https://royalsocietypublishing.org/doi/pdf/10.1098/rspa.1955.0191 .

[74] M. Howe, *Theory of Vortex Sound*, Cambridge Texts in Applied Mathematics (Cambridge University Press, 2003).

[75] H. Fujita, *The characteristics of the aeolian tone radiated from two-dimensional cylinders,* Fluid Dynamics Research **42**, 015002 (2010).

[76] C. Norberg, *Fluctuating lift on a circular cylinder: review and new measurements,* Journal of Fluids and Structures **17**, 57 (2003).

[77] L. Fagiano, K. Huynh, B. Bamieh, and M. Khammash, *Sensor fusion for tethered wings in airborne wind energy,* in *Proceedings of the 2013 American Control Conference (ACC)* (IEEE, Washington, DC, USA, 2013).

[78] J. Breukels, *An Engineering Methodology for Kite Design*, Ph.D. thesis, Delft University of Technology (2011).

[79] F. Yunus, *Methodologies and algorithms for sound propagation in complex environments with application to urban air mobility: A ray acoustics approach*, Dissertation, TU Delft, Delft University of Technology (2023).

[80] N. Elbers, *Assessment of an aircraft propeller noise model by verification & experimental validation*, Master's thesis, Delft University of Technology, Delft, The Netherlands (2021), to be publicly defended on December 22nd, 2021.

[81] A. Manela and M. Howe, *The forced motion of a flag,* Journal of Fluid Mechanics **635**, 439 (2009).

[82] P. Rojratsirikul, Z. Wang, and I. Gursul, *Effect of pre-strain and excess length on unsteady fluid–structure interactions of membrane airfoils,* Journal of Fluids and Structures **26**, 359 (2010).

[83] International Electrotechnical Commission, *International standard iec 61672-1:2013,* (2013), standard No. IEC 61672-1:2013.

[84] M. Schelbergen and R. Schmehl, *Swinging motion of a kite with suspended control unit flying turning manoeuvres,* Wind Energy Science **9**, 1323 (2024).

[85] O. Cayon, *Extended kalman filter for airborne wind energy systems (awes),* (2025).

[86] M. Folkersma, R. Schmehl, and A. Viré, *Boundary layer transition modeling on leading edge inflatable kite airfoils,* Wind Energy **22**, 908 (2019).

[87] J. Watchorn, *Aerodynamic Load Modelling for Leading Edge Inflatable Kites*, Master's thesis, Delft University of Technology, Delft, The Netherlands (2023), supervisors: A.C. Viré, R. Schmehl, Alexander van Zuijlen.

[88] M. Deaves, *An Investigation of the Non-Linear 3D Flow Effects Relevant for Leading Edge Inflatable Kites*, Master's thesis, TU Delft, Delft, The Netherlands (2015), supervisors: R. Schmehl, M. Gaunaa, T. Gillebaart.

[89] A. Viré, G. Lebesque, M. Folkersma, and R. Schmehl, *Effect of chordwise struts and misaligned flow on the aerodynamic performance of a leading-edge inflatable wing,* Energies **15** (2022), 10.3390/en15041450.

[90] O. Cayon, R. Schmëhl, A. Luca, and J. Peschel, *Kitepower flight data acquired on 27 november 2023,* Data set (2024).

[91] D. Johnson, *Electrical engineering,* (2023).

[92] Toyota FRC, *Toyota leading edge inflatable kite flight demonstration,* (2024), video posted on X (formerly Twitter).

[93] A. M. Malgoezar, A. Vieira, M. Snellen, D. G. Simons, and L. L. Veldhuis, *Experimental characterization of noise radiation from a ducted propeller of an unmanned aerial vehicle,* International Journal of Aeroacoustics **18**, 372 (2019).

[94] F. Simon, N. H. Schiller, N. S. Zawodny, N. A. Pettingill, and M. B. Galles, *Fundamental noise characterization of a ducted propeller in hover,* in *Inter-noise 2022* (International Institute of Noise Control Engineering, Glasgow, Scotland, 2022) nASA Langley Research Center.

[95] M. Jafari, F. Hou, and A. Abdelkefi, *Wind-induced vibration of structural cables,* Nonlinear Dynamics **100**, 351 (2020).

[96] W. S. Chiu and J. H. Lienhard, *On real fluid flow over yawed circular cylinders,* in *Proceedings of the ASME Winter Annual Meeting* (1967) pp. 1–8.

[97] S. Yamada, H. Fujita, Y. Maruta, H. Maki, and J. Shiraishi, *Experimental study on aerodynamic noise generated from two-dimensional models: 2nd report, effect of the angle of inclination of circular cylinders and the angle of attack of square cylinders to aerodynamic noise,* Transactions of the Japan Society of Mechanical Engineers (B Edition) **63** (1974), paper No. 96-1406.

[98] M. Arntzen, *Aircraft Noise Calculation and Synthesis in a Non-Standard Atmosphere*, Doctoral thesis, TU Delft (2014).

[99] I. O. for Standardisation (ISO), *Acoustics - attenuation of sound during propagation outdoors - Part 1: Calculation of the absorption of sound by the atmosphere*, Tech. Rep. (International Standard ISO 9613-1, 1993).

[100] H. E. Bass, L. C. Sutherland, and A. J. Zuckerwar, *Atmospheric absorption of sound: Update,* The Journal of the Acoustical Society of America **88**, 2019 (1990).

[101] H. E. Bass, L. C. Sutherland, A. J. Zuckerwar, D. T. Blackstock, and D. M. Hester, *Atmospheric absorption of sound: Further developments,* The Journal of the Acoustical Society of America **97**, 680 (1995).

[102] F. Bertagnolio and A. Fischer, *Wind turbine aerodynamic noise sources,* in *Handbook of Wind Energy Aerodynamics*, edited by B. Stoevesandt, G. Schepers, P. Fuglsang, and Y. Sun (Springer International Publishing, Cham, Switzerland, 2022) pp. 1365–1396.

[103] B. Plovsing and J. Kragh, *Nord2000. Comprehensive Outdoor Sound Propagation Model. Part 1: Propagation in an Atmosphere without Significant Refraction*, Tech. Rep. (DELTA, 2001).

[104] B. Plovsing, *Nord2000. Comprehensive Outdoor Sound Propagation Model. Part 2: Propagation in an Atmosphere with Refraction*, Tech. Rep. (DELTA, 2006).

A

Tether and Bridle Line Noise Model - Verification

The verification for the vortex-shedding predictive model was performed using experimental data from Latorre Iglesias et al. [65]. The first verification looks at the shedding frequency and the value of the sound pressure level. In the paper of Latorre Iglesias et al., an array of microphones was used to capture the noise emission of circular cylinders in an open jet anechoic wind tunnel. The values obtained for a cylinder with no inclination are presented in Figure A.1, in comparison with the predictive model. The experimental data is presented for two different measurements at $31.5 m/s$ and $50 m/s$ with values in 1/3 octaves. The predictive model calculates only the tonal noise produced at the shedding frequency, shown as a single peak. It can be observed from Figure A.1 that the value of the peak itself and at which frequency is emitted is similar for both the experimental data and the simulation. The model slightly overpredicts the shedding frequency and the SPL, although this difference might appear from multiple factors related to the model or the measured data.

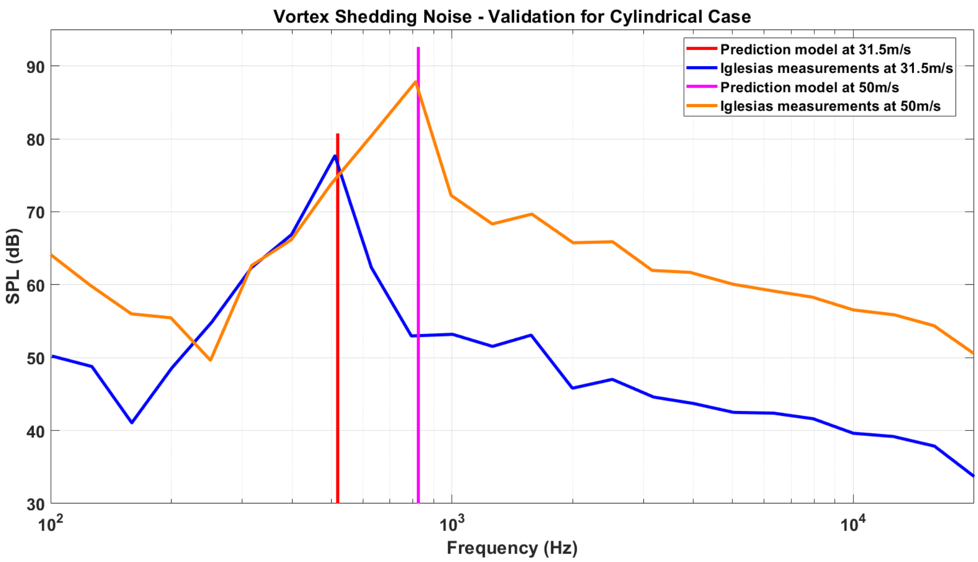

Figure A.1: Verification of the noise spectrum for the circular cylinder between predictive model and experimental data from Latorre Iglesias et al. [65] at $31.5 m/s$ and $50 m/s$ and $\beta = 0$.

The second verification reviews the dependency of the vortex shedding frequency on the yaw angle. Based on Equation 3.5, the shedding frequency should be the highest when the yaw angle is zero, and it should increase with the flow velocity when the yaw angle is kept constant. Figure A.2 presents this trend using the predictive model and the experimental data from Latorre Iglesias et al. [65]. It can be observed that the frequency increases with velocity as expected, but the values of the simulation and real measurements are quite different. Based on the independence principle, the Strouhal number and the shedding frequency implicitly should only change with a factor approximated by $\cos(\beta)$ when the speed is kept constant. The prediction model respects this, but it appears that the experimental data does not present the same behavior.

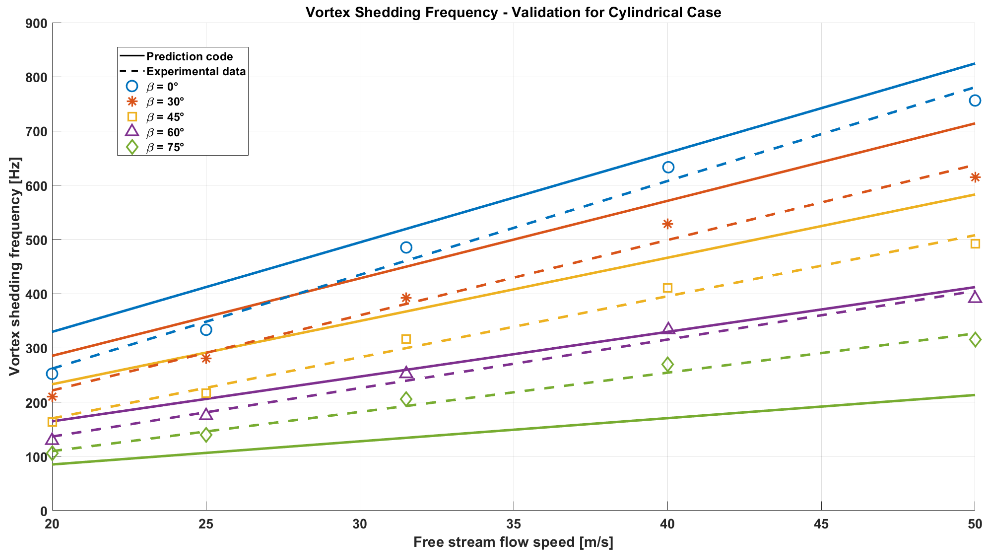

Figure A.2: Verification between predictive model and experimental data from Latorre Iglesias et al. [65] of the vortex shedding frequency of circular cylinder with different flow speeds and yaw angles.

To understand the reasons behind these differences, all the plotted lines were analyzed to assess how they change. For the prediction model, it is clear that at constant yaw angle, the frequency increases proportionally with the speed. The Reynolds number increases as well, but its influence on the Strouhal number is negligible. Therefore, it can be concluded that St stays constant and the frequency varies linearly with velocity at constant yaw angle. When the velocity is kept constant, the shedding frequency decreases with increasing yaw angle by a factor $\cos(\beta)$ for the predictive model.

The experimental measurements from Latorre Iglesias et al. [65] were investigated by calculating different properties from the plotted lines. After further inspecting the slopes of the lines from Figure A.2, it seems that the differences come from the values of the Strouhal number. As discussed before and shown in Equation 3.3, the value of the Strouhal number for this Reynolds interval should be around 0.2. However, the values obtained by Latorre Iglesias et al. [65] correspond to Strouhal numbers spread over a large interval between 0.14 and 0.33, which leads to believe that some errors were involved in these Strouhal number calculations. For the Reynolds numbers corresponding to speeds of 31.5 m/s and 50 m/s, it seems that the St value is around 0.2, as can be seen in Figure A.3. This is exactly the reason for which the verification in Figure A.1 only showed small differences.

The Strouhal value was further validated with experimental data from other authors, such as Jafari et al. [95], Chiu et al. [96], and Yamada et al. [97]. In all the aforementioned papers, the measured St value respects the independence principle accurately. Figure A.4 shows the effect of yaw angle on the Strouhal number, which is almost identical to the results from the prediction code.

The final verification is performed to check if the variation of the radiation angle Ψ yields the expected behavior. The lift fluctuation correlated with the vortex shedding around a cylindrical body should exhibit the directivity pattern of a dipole, as explained in Section 2.3. The maximum SPL value should be obtained when the observer is placed in the same direction as the axis of lift fluctuation, and it should decrease toward the perpendicular direction. Figure A.5 presents the results obtained from the prediction model for radiation angles between $-90°$ and $90°$, which are identical to the ones from a theoretical dipole also shown in Latorre Iglesias et al. [65]. Finally, a last verification was performed through a sensitivity analysis by changing multiple parameters of the model (such as doubling the diameter of the cylinder) and it was observed that the SPL value changes as expected.

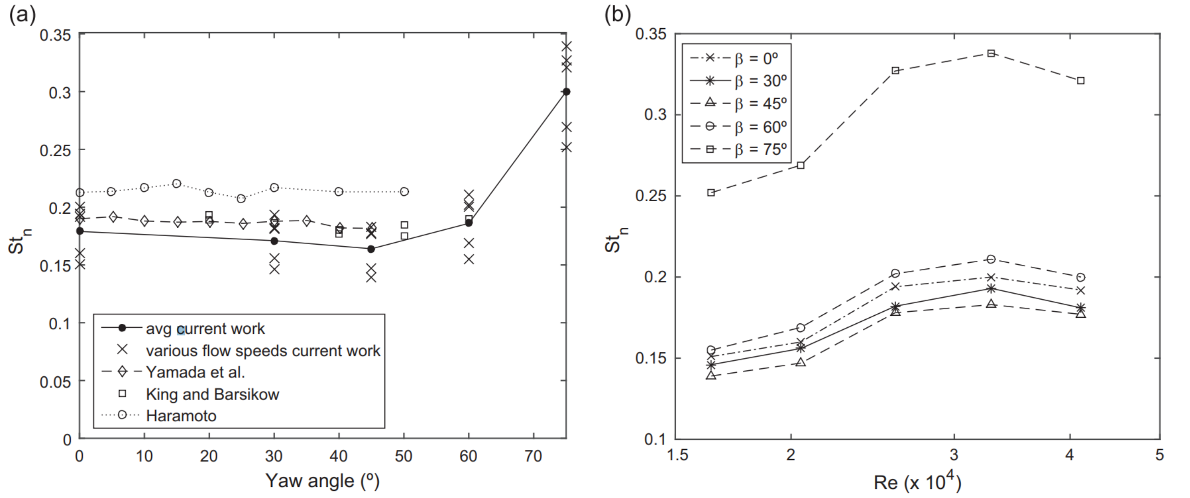

Figure A.3: Variation of Strouhal number with a) the yaw angle and with b) the Reynolds number. Retrieved from Latorre Iglesias et al. [65].

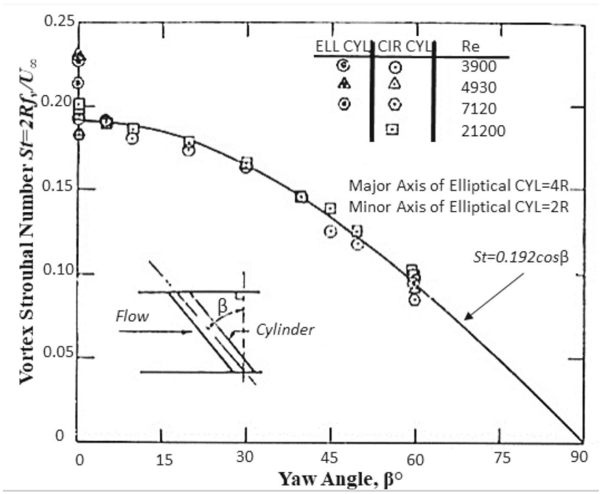

Figure A.4: Experimental results showing the effect of yaw angle on the Strouhal number for a circular cylinder, respecting the independence principle. Retrieved from Chiu et al. [96].

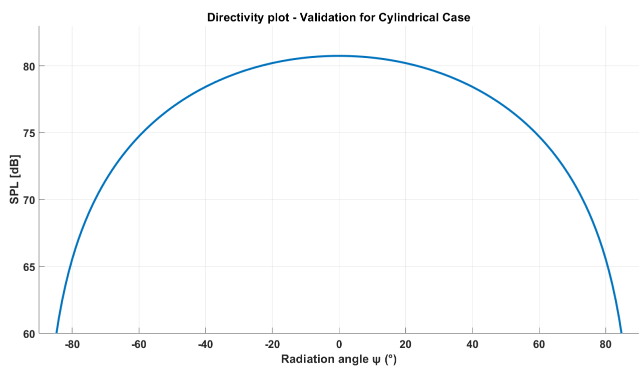

Figure A.5: Directivity pattern of vortex shedding around a circular cylinder, obtained from the prediction model ($v_a = 31.5$ m/s, $\beta = 0°$).

B

BPM Model Equations - Verification

B.1. Turbulent Boundary Layer - Trailing Edge Noise (TBL-TE)

The Strouhal numbers must be calculated first as they are the base for the other shape functions.

$$St_p = \frac{f\delta_p^*}{U} \tag{B.1}$$

$$St_p = \frac{f\delta_s^*}{U} \tag{B.2}$$

$$St_1 = 0.02M^{-0.6} \tag{B.3}$$

$$\bar{St}_1 = \frac{St_1 + St_2}{2} \tag{B.4}$$

$$St_2 = St_1 \times \begin{cases} 1 & (\alpha < 1.33^\circ) \\ 10^{0.0054(\alpha-1.33)^2} & (1.33^\circ \le \alpha \le 12.5^\circ) \\ 4.72 & (12.5^\circ < \alpha) \end{cases} \tag{B.5}$$

The spectral shape functions A can be calculated using the Strouhal numbers from above, and based on other parameters such as chord Reynolds number. Multiple intermediary steps must be taken before for all the scaling functions.

$$A_{min}(a) = \begin{cases} \sqrt{67.552 - 886.788a^2} - 8.219 & (a < 0.204) \\ -32.665a + 3.981 & (0.204 \le a \le 0.244) \\ -142.795a^3 + 103.656a^2 - 57.757a + 6.006 & (0.244 < a) \end{cases} \tag{B.6}$$

$$A_{max}(a) = \begin{cases} \sqrt{67.552 - 886.788a^2} - 8.219 & (a < 0.13) \\ -15.901a + 1.098 & (0.13 \le a \le 0.321) \\ -4.669a^3 + 3.491a^2 - 16.699a + 1.149 & (0.321 < a) \end{cases} \tag{B.7}$$

$$a = \left| \log_{10}\left(\frac{St}{St_{peak}}\right) \right| \tag{B.8}$$

$$a_0(R_c) = \begin{cases} 0.57 & (R_c < 9.52 \times 10^4) \\ (-9.57 \times 10^{-13})(R_c - 8.57 \times 10^5) + 1.13 & (9.52 \times 10^4 \le R_c \le 8.57 \times 10^5) \\ 1.13 & (8.57 \times 10^5 < R_c) \end{cases} \tag{B.9}$$

$$A_R(a_0) = \frac{-20 - A_{min}(a_0)}{A_{max}(a_0) - A_{min}(a_0)} \tag{B.10}$$

$$A(a) = A_{min}(a) + A_R(a_0)\,[A_{max}(a) - A_{min}(a)] \tag{B.11}$$

The spectral shape function B is calculated in a similar manner to A, where B will be calculated as an interpolation between the intermediary shape functions B_{min} and B_{max}.

$$B_{min}(b) = \begin{cases} \sqrt{16.88 - 886.788b^2} - 4.109 & (b < 0.13) \\ -83.607b + 8.138 & (0.13 \le b \le 0.145) \\ -817.810b^3 + 355.210b^2 - 135.024b + 10.619 & (0.145 < b) \end{cases} \tag{B.12}$$

$$B_{max}(b) = \begin{cases} \sqrt{16.88 - 886.788b^2} - 4.109 & (b < 0.10) \\ -31.330b + 1.854 & (0.10 \le b \le 0.187) \\ -80.541b^3 + 44.174b^2 - 39.381b + 2.344 & (0.187 < b) \end{cases} \tag{B.13}$$

$$b = \left|\log_{10}\left(\frac{St_s}{St_2}\right)\right| \tag{B.14}$$

$$b_0(R_c) = \begin{cases} 0.30 & (R_c < 9.52 \times 10^4) \\ \left(-4.48 \times 10^{-13}\right)(R_c - 8.57 \times 10^5) + 0.56 & (9.52 \times 10^4 \le R_c \le 8.57 \times 10^5) \\ 0.56 & (8.57 \times 10^5 < R_c) \end{cases} \tag{B.15}$$

$$B_R(b_0) = \frac{-20 - B_{min}(b_0)}{B_{max}(b_0) - B_{min}(b_0)} \tag{B.16}$$

$$B(b) = B_{min}(b) + B_R(b_0)\,[B_{max}(b) - B_{min}(b)] \tag{B.17}$$

The amplitude function K_1 is calculated first as a function of Reynolds number. There is a level adjustment ΔK_1 for the pressure-side contribution for nonzero angles of attack.

$$K_1 = \begin{cases} -4.31\log_{10}(R_c) + 156.3 & (R_c < 2.47 \times 10^5) \\ -9.0\log_{10}(R_c) + 181.6 & (2.47 \times 10^5 \le R_c \le 8.0 \times 10^5) \\ 128.5 & (8.0 \times 10^5 < R_c) \end{cases} \tag{B.18}$$

$$\Delta K_1 = \begin{cases} \alpha_* \left[1.43\log_{10}\left(R_{\delta_p^*}\right) - 5.29\right] & (R_{\delta_p^*} \le 5000) \\ 0 & (5000 < R_{\delta_p^*}) \end{cases} \tag{B.19}$$

where $R_{\delta_p^*}$ is the Reynolds number based on pressure-side displacement thickness. The second amplitude function K_2 can be calculated now.

$$K_2 = K_1 + \begin{cases} -1000 & (\alpha < \gamma_0 - \gamma) \\ \sqrt{\beta^2 - (\beta/\gamma)^2(\alpha - \gamma_0)^2} + \beta_0 & (\gamma_0 - \gamma \le \alpha \le \gamma_0 + \gamma) \\ -12 & (\gamma_0 + \gamma < \alpha) \end{cases} \tag{B.20}$$

where the parameters are described by:

$$\begin{cases} \gamma = 27.094M + 3.31 \\ \beta = 76.65M + 10.74 \end{cases} \quad \begin{cases} \gamma_0 = 23.43M + 4.651 \\ \beta_0 = -34.19M - 13.82 \end{cases} \tag{B.21}$$

B.1.1. Verification of the Implementation

For the analysis of turbulent boundary layer trailing edge noise, seven distinct cases were examined. The specification for these cases are presented in Table B.1. According to the study by Brooks, Pope, and Marcolini [50], the experimental data was gathered using a NACA0012 airfoil. This airfoil was tested with varying chord lengths from 5.08 cm to 30.48 cm and a span of 45.72 cm, under different velocities and angles of attack. It is important to note that these measurements were taken from both tripped and untripped boundary layers. Results from the model are compared in Figure B.1 and Figure B.2.

Table B.1: Input parameters for the model verification of turbulent boundary layer trailing edge noise.

Case #	1	2	3	4	5	6	7
c, [cm]	15.24			22.86			
U, [m/s]	31.7	39.6	55.5	39.6			
α, [°]	0			0	2	4	7.3

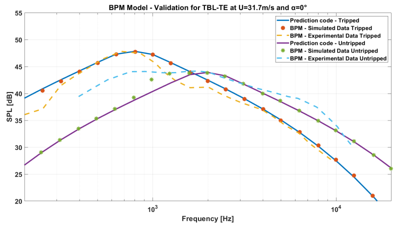

(a) Case 1

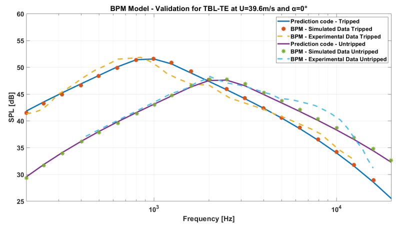

(b) Case 2

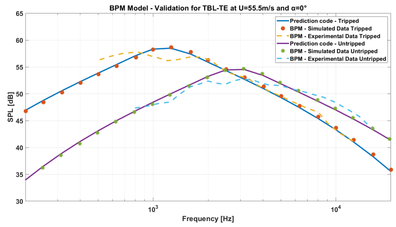

(c) Case 3

Figure B.1: Comparison between prediction values of TBL-TE noise and experimental data: cases 1-3.

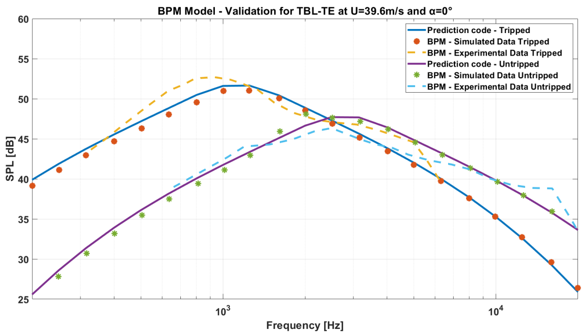

(a) Case 4

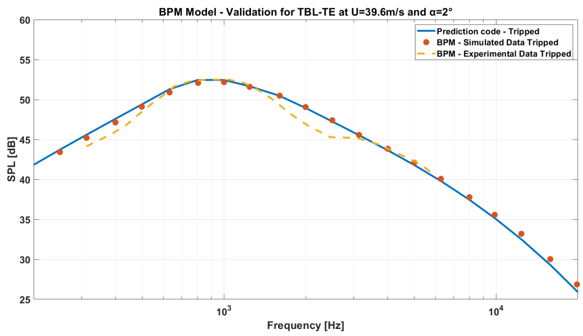

(b) Case 5

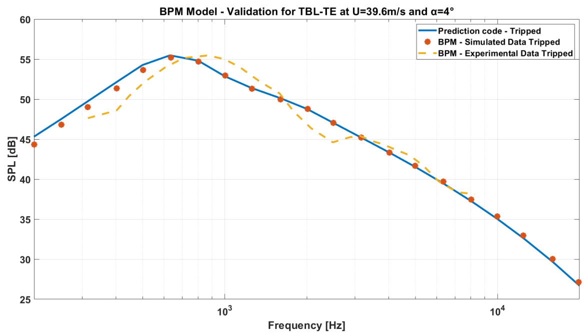

(c) Case 6

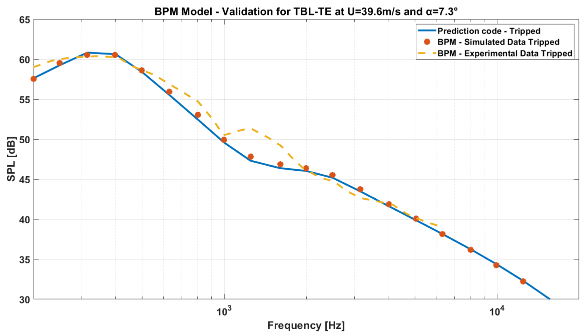

(d) Case 7

Figure B.2: Comparison between prediction values of TBL-TE noise and experimental data: cases 4-7.

B.2. LAMINAR BOUNDARY LAYER-VORTEX SHEDDING NOISE (LBL-VS)

The Strouhal definitions for the laminar boundary layer vortex shedding noise are:

$$St' = \frac{f\delta_p}{U} \tag{B.22}$$

$$St_1' = \begin{cases} 0.18 & (R_c < 1.3\times 10^5) \\ 0.001756 R_c^{0.3931} & (1.3\times 10^5 \le R_c \le 4\times 10^5) \\ 0.28 & (4\times 10^5 < R_c) \end{cases} \tag{B.23}$$

$$St'_{peak} = St_1' \times 10^{-0.04\alpha} \tag{B.24}$$

If the Strouhal ratio e is defined as $e = St'/St'_{peak}$, the spectral shape function G_1 can be calculated.

$$G_1(e) = \begin{cases} 39.8\log_{10}(e) - 11.12 & (e \le 0.5974) \\ 98.409\log_{10}(e) + 2 & (0.5974 < e \le 0.8545) \\ -5.076 + \sqrt{2.484 - 506.25\left[\log_{10}(e)\right]^2} & (0.8545 < e \le 1.17) \\ -98.409\log_{10}(e) + 2 & (1.17 < e \le 1.674) \\ -39.8\log_{10}(e) - 11.12 & (1.674 < e) \end{cases} \tag{B.25}$$

The peak scaled level shape curve G_2 depends on Reynolds number and angle as:

$$G_2(d) = \begin{cases} 77.852\log_{10}(d) + 15.328 & (d \le 0.3237) \\ 65.188\log_{10}(d) + 9.125 & (0.3237 < d \le 0.5689) \\ -14.052\left[\log_{10}(d)\right]^2 & (0.5689 < d \le 1.7579) \\ -65.188\log_{10}(d) + 9.125 & (1.7579 < d \le 3.0889) \\ -77.852\log_{10}(d) + 15.328 & (3.0889 < d) \end{cases} \tag{B.26}$$

where $d = R_c/(R_c)_0$ and:

$$(R_c)_0 = \begin{cases} 10^{0.215\alpha + 4.978} & (\alpha \le 3) \\ 10^{0.120\alpha + 5.263} & (3 < \alpha) \end{cases} \tag{B.27}$$

$$G_3(\alpha) = 171.04 - 3.03\alpha \tag{B.28}$$

B.2.1. VERIFICATION OF THE IMPLEMENTATION

This verification evaluates six distinct cases to validate the laminar boundary layer vortex shedding noise model. Each case subjects the airfoil to a consistent freestream velocity of 39.6 m/s. Half of the cases feature an airfoil with a chord of 10.16 cm, while the others use a larger chord of 30.48 cm. The angles of attack range between 0° and 6.7° for airfoils with the smaller chord and between 0° and 3° for those with the larger chord. Notably, the BPM report utilizes untripped boundary layer parameters specifically for these laminar boundary layer vortex shedding noise evaluations. Detailed parameters for this analysis can be found in Table B.2, and the results are presented in Figure B.3.

Table B.2: Input parameters for the model verification of laminar boundary layer vortex shedding noise.

Case #	1	2	3	4	5	6
c, [cm]	10.16			30.48		
U, [m/s]	39.6					
α, [°]	0	3.3	6.7	0	1.5	3

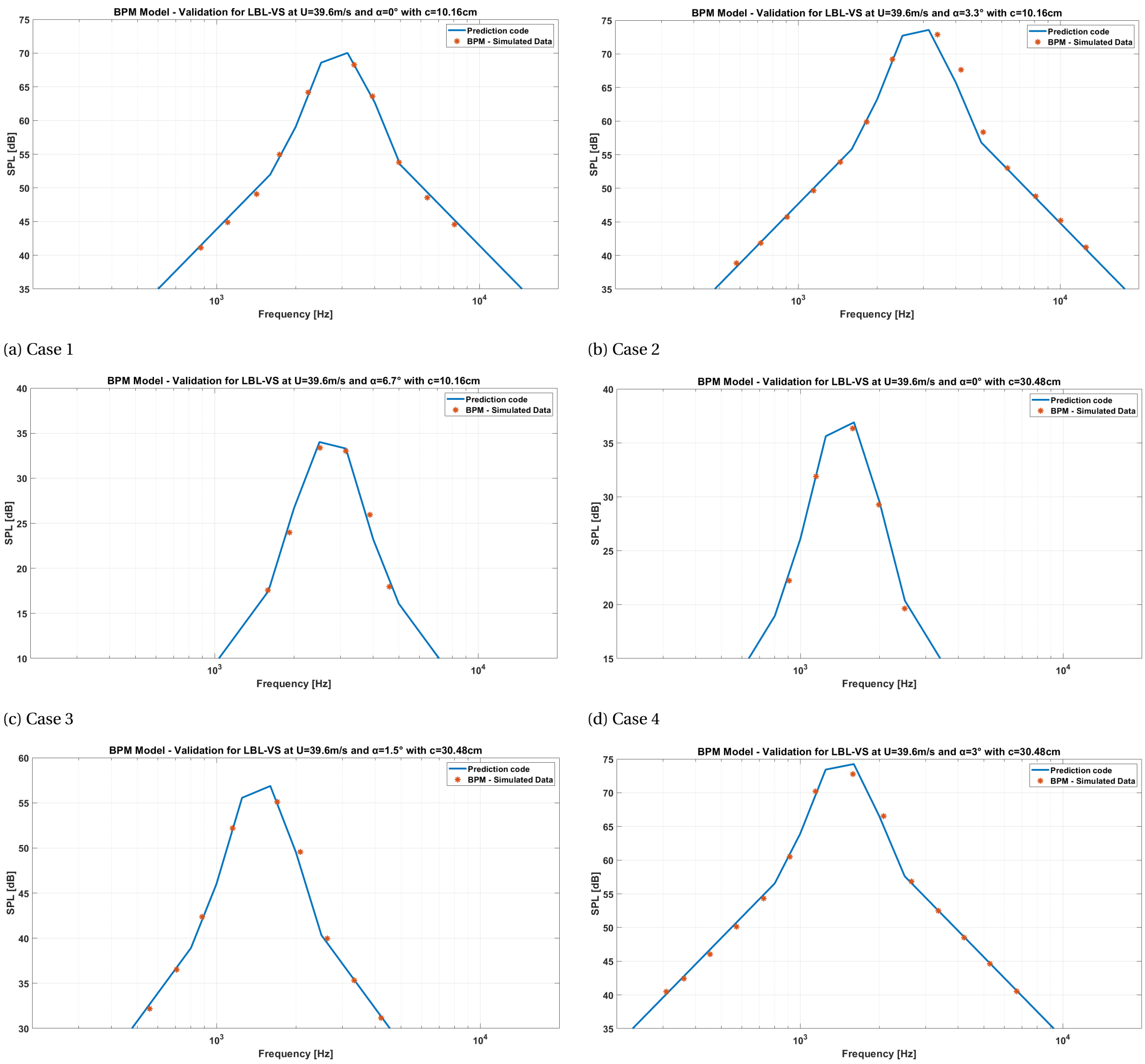

(a) Case 1

(b) Case 2

(c) Case 3

(d) Case 4

(e) Case 5

(f) Case 6

Figure B.3: Comparison between prediction values of LBL-VS noise and experimental data.

B.3. TRAILING EDGE BLUNTNESS NOISE (TEB)

The Strouhal number for the trailing edge bluntness noise is:

$$St''' = \frac{fh}{U} \tag{B.29}$$

$$St'''_{peak} = \begin{cases} \frac{0.212-0.0045\Psi}{1+0.235(h/\delta^*_{avg})^{-1}-0.0132(h/\delta^*_{avg})^{-2}} & (0.2 \leq (h/\delta^*_{avg})) \\ 0.1(h/\delta^*_{avg}) + 0.095 - 0.00243\Psi & ((h/\delta^*_{avg}) < 0.2) \end{cases} \tag{B.30}$$

The ratio between the TE thickness to the average boundary-layer displacement is:

$$\delta^*_{avg} = \frac{\delta^*_p + \delta^*_s}{2} \tag{B.31}$$

The angle Ψ is the angle between the sloping surfaces upstream of the trailing edge. The shape functions can be calculated:

$$G_4(h/\delta^*_{avg}, \Psi) = \begin{cases} 17.5\log_{10}(h/\delta^*_{avg}) + 157.5 - 1.114\Psi & (h/\delta^*_{avg} \leq 5) \\ 16.7 - 1.114\Psi & (5 < h/\delta^*_{avg}) \end{cases} \tag{B.32}$$

$$G_5\left(\frac{h}{\delta^*_{avg}}, \Psi, \frac{St'''}{St'''_{peak}}\right) = (G_5)_{\Psi=0^\circ} + 0.0714\Psi\left[(G_5)_{\Psi=14^\circ} - (G_5)_{\Psi=0^\circ}\right] \tag{B.33}$$

$$(G_5)_{\Psi=14^\circ} = \begin{cases} m\eta + k & (\eta < \eta_0) \\ 2.5\sqrt{1-(\eta/\mu)^2} - 2.5 & (\eta_0 \le \eta < 0) \\ \sqrt{1.5625 - 11794.99\eta^2} - 2.5 & (0 \le \eta < 0.0316) \\ -155.543\eta + 4.375 & (0.0316 \le \eta) \end{cases} \tag{B.34}$$

$$\eta = \log_{10}\left(\frac{St'''}{St'''_{peak}}\right) \tag{B.35}$$

$$\eta = \begin{cases} 0.1221 & (h/\delta^*_{avg} < 0.25) \\ -0.2175(h/\delta^*_{avg}) + 0.1755 & (0.25 \le h/\delta^*_{avg} < 0.62) \\ -0.0308(h/\delta^*_{avg}) + 0.0596 & (0.62 \le h/\delta^*_{avg} < 1.15) \\ 0.0242 & (1.15 \le h/\delta^*_{avg}) \end{cases} \tag{B.36}$$

$$m = \begin{cases} 0 & (h/\delta^*_{avg} \le 0.02) \\ 68.724(h/\delta^*_{avg}) - 1.35 & (0.02 < h/\delta^*_{avg} \le 0.5) \\ 308.475(h/\delta^*_{avg}) - 121.23 & (0.5 < h/\delta^*_{avg} \le 0.62) \\ 224.811(h/\delta^*_{avg}) - 69.35 & (0.62 < h/\delta^*_{avg} \le 1.15) \\ 1583.28(h/\delta^*_{avg}) - 1631.59 & (1.15 < h/\delta^*_{avg} \le 1.2) \\ 268.344 & (1.2 < h/\delta^*_{avg}) \end{cases} \tag{B.37}$$

$$\eta_0 = -\sqrt{\frac{m^2\mu^4}{6.25 + m^2\mu^2}} \tag{B.38}$$

$$k = 2.5\sqrt{1-\left(\frac{\eta_0}{\mu}\right)^2} - 2.5 - m\eta_0 \tag{B.39}$$

$$\left(\frac{h}{\delta^*_{avg}}\right)' = 6.724\left(\frac{h}{\delta^*_{avg}}\right)^2 - 4.019\left(\frac{h}{\delta^*_{avg}}\right) + 1.107 \tag{B.40}$$

B.3.1. VERIFICATION OF THE IMPLEMENTATION

The vortex shedding noise due to bluntness at the trailing edge was investigated across three different edge heights from 1.1 mm to 2.5 mm. The airfoil used in this study has a chord length of 60.96 cm, and it is exposed to a freestream velocity of 38.6 m/s. As part of this analysis, the BPM report [50] incorporates tripped boundary layer conditions, and the detailed input parameters are specified in Table B.3 with results in Figure B.4.

Table B.3: Input parameters for the model verification of trailing edge bluntness vortex shedding noise.

Case #	1	2	3
h_{TE}, [mm]	1.1	1.9	2.5
c, [cm]	60.96		
U, [m/s]	38.6		
α, [°]	0		

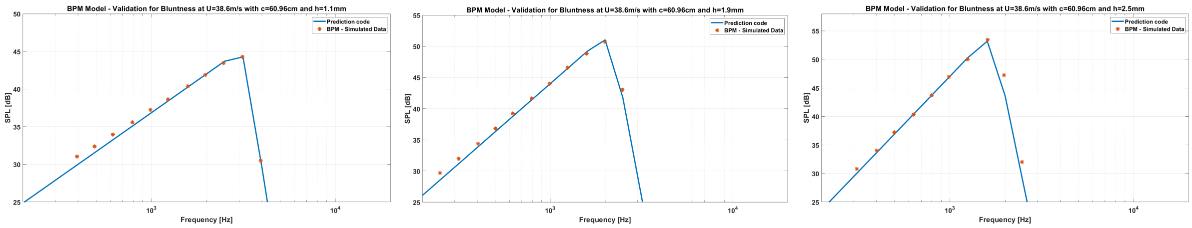

(a) Case 1 (b) Case 2 (c) Case 3

Figure B.4: Comparison between prediction values of TEB noise and experimental data.

B.4. TIP VORTEX NOISE (TV)

BPM model describes two types of tip shapes - flat and round - with different parameters depending on the shape. For this thesis, the flat formulation is of interest as both the propeller blade and the LEI kite have a sharper tip. The Strouhal number for the tip vortex noise is:

$$St'' = \frac{fl}{U_{max}} \tag{B.41}$$

$$\frac{l_{round}}{c} = 0.008\alpha_{TIP} \tag{B.42}$$

$$\frac{l_{flat}}{c} = \begin{cases} 0.0230 + 0.0169\alpha_{TIP} & (0° \leq \alpha_{TIP} \leq 2°) \\ 0.0378 + 0.0095\alpha_{TIP} & (2° < \alpha_{TIP}) \end{cases} \tag{B.43}$$

$$\frac{M_{MAX}}{M} \approx (1 + 0.036\alpha_{TIP}) \tag{B.44}$$

$$U_{MAX} = c_0 M_{MAX} \tag{B.45}$$

B.4.1. VERIFICATION OF THE IMPLEMENTATION

The noise attributable to tip vortex formation is evaluated by comparing it with experimental data from the BPM report. It is important to highlight that the original experimental dataset cannot differentiate properly the tip vortex noise from the noise measurements, but the semi-empirical formulation was constructed considering other literature reviews and papers. This predictive analysis is conducted on an airfoil with a chord length of 15.24 cm and a span of 38.48 cm, subjected to a freestream velocity of 71.3 m/s with a high AoA of 10.8°.

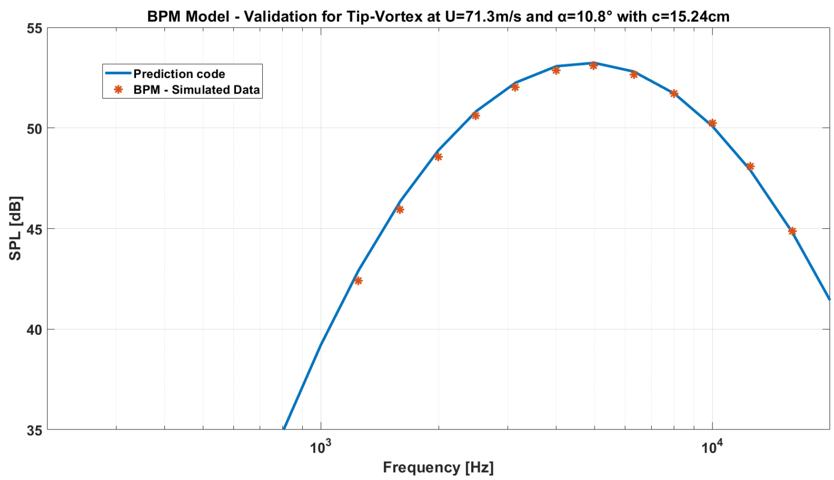

Figure B.5: Comparison between prediction values of tip vortex noise and experimental data.

B.5. FINAL REMARKS

The predicted data from the code and the experimental values closely match. Subsequently, a sensitivity analysis was performed by changing certain parameters, such as the distance to the observer and the Mach number, confirming the correct implementation of the model. However, during the verification process, some inconsistencies were noted regarding the secondary functions or shape functions. One of these problems is clearly shown with the G_2 function used for laminar boundary layer vortex shedding. Due to some errors in the original BPM report [50], some of the functions are not continuous across all intervals. When the verification was performed, the results of the prediction code differed significantly from the experimental values. After investigating and resolving these issues, it was proven that the prediction data matched the results from the original report.

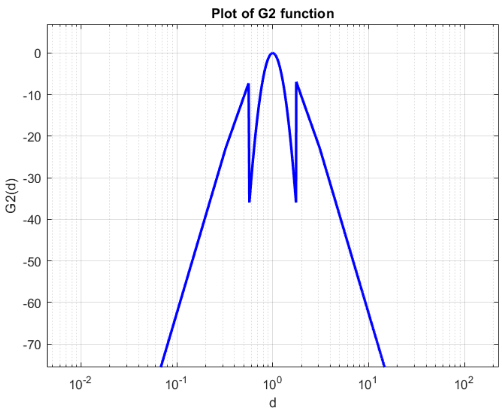

(a) Original intervals.

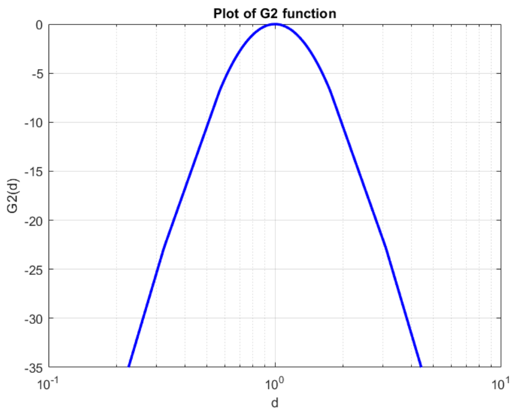

(b) Corrected intervals.

Figure B.6: Continuity correction for G_2 function used for prediction of LBL-VS noise.

C

Propagation Model

In this study, several fundamental sound propagation mechanisms, previously discussed in Section 2.4, were evaluated for potential integration into the acoustic prediction framework. These include spherical spreading, Doppler shift, atmospheric absorption, and ground reflection. Each of these phenomena can significantly influence the perceived sound level at the observer's location and can be reasonably modeled using established analytical or semi-empirical approaches. Accordingly, they were assessed for their relevance and suitability for inclusion in the framework.

In contrast, acoustic scattering and diffusion arising from atmospheric turbulence and surface irregularities were not incorporated into the current model. Although these mechanisms can impact long-range propagation and contribute to the redistribution of sound energy into acoustical shadow zones, accurately modeling them requires highly complex and computationally intensive approaches. Given the scope and practical focus of this work, it was considered appropriate to exclude scattering and diffusion from the analysis. Furthermore, the flight zones where the V9.60 kite from Kitepower currently operates and from which audio recordings were obtained are open-field environments, largely free from buildings or significant obstacles. This further supports the decision to omit such effects from the present framework.

C.1. Spherical Spreading

The spherical spreading can be described through the inverse square law, as depicted in Figure 2.13. This happens because the power emitted by the source is constant through all the spheres with varying distance, but the intensity (and therefore SPL) decreases with the distance squared. Based on ISO 9613-2 [38, 39], if a point source is considered, the sound pressure level at the location of a receiver can be calculated as:

$$L_s = L_w + D_c - A_{div} \tag{C.1}$$

where L_w is the sound power level produced by the point source, D_c considers the directivity correction, and A_{div} is the attenuation that occurs during the propagation towards the observer. In case of a directivity with an omnidirectional point source, the equation for calculating it is:

$$D_c = 10\log\left(\frac{4\pi}{\Omega}\right) \tag{C.2}$$

where Ω is the solid angle remaining for radiation. Table 2 from ISO 9613-2 [39] offers more details of how to calculate for different scenarios. The geometric divergence A_{div} from a point source makes use of the spherical area and it is:

$$A_{div} = 10\log(4\pi r^2) \approx 20\log(r) + 11 \tag{C.3}$$

where r is the distance to the observer and the value 11 comes from the conversion of sound power level to SPL. If the sound power level L_w is replaced by the SPL value, A_{div} will only depend on the ratio of intensity and the value $10\log(4\pi) \approx 11$ should not be included anymore [98].

C.2. Atmospheric Absorption Model

Sound absorption occurs through environmental and boundary mechanisms. Environmental absorption is influenced by temperature, humidity, pressure, and gas relaxation effects, while boundary absorption is typically included in reflection models. These mechanisms are incorporated in standards like ISO 9613-1 [99], based on studies by Bass et al. [100, 101].

The attenuation is a function of the two most abundant gases in the atmosphere, respectively oxygen and nitrogen. Their two relaxation factors are:

$$f_{r,N} = \frac{p_a}{p_0}\left(\frac{T_0}{T_a}\right)^{\frac{1}{2}}\left(9 + 280 \cdot H \cdot \exp\left(-4.17\left[\left(\frac{T_0}{T_a}\right)^{\frac{1}{3}} - 1\right]\right)\right) \tag{C.4}$$

$$f_{r,O} = \frac{p_a}{p_0}\left(24 + 4.04 \times 10^4 \cdot H \cdot \frac{0.02 + H}{0.391 + H}\right) \tag{C.5}$$

where p_a and T_a are the atmospheric pressure and temperature, p_0 and T_0 are the reference pressure and temperature, and H is the molar concentration of water vapor as a percentage. The atmospheric coefficient α can be calculated for the specific frequency f in the following way:

$$\alpha(f) = 8.686 f^2 \left[\left(\frac{1.84 \times 10^{-11}}{\left(\frac{T_0}{T_a}\right)^{\frac{1}{2}} \frac{p_a}{p_0}}\right) + \left(\frac{T_0}{T_a}\right)^{2.5}\left(\frac{0.10680 e^{-3352/T_a} f_{r,N}}{f^2 + f_{r,N}^2} + \frac{0.01275 e^{-2239.1/T_a} f_{r,O}}{f^2 + f_{r,O}^2}\right)\right] \tag{C.6}$$

The value 8.686 comes from the conversion of Nepers to dB. The absolute humidity H used for the molar relaxation factors can be determined from the relative humidity h as:

$$H = h \cdot \frac{p_{sat}}{p_0} \cdot \frac{p_0}{p_a} \tag{C.7}$$

The saturated pressure, p_{sat}, can be calculated using various methods. However, based on a more recent formulation by Bass et al. [101], it is given by:

$$\log_{10}\left(\frac{p_{sat}}{p_0}\right) = -6.8346\left(\frac{T_{01}}{T_a}\right)^{1.261} + 4.6151. \tag{C.8}$$

where $T_{01} = 273.16$ K is the triple-point isotherm temperature. Based on all the formulae from above, the atmospheric attenuation in dB can be calculated for a certain distance r to the observer as:

$$L_{att} = -\alpha(f) \cdot r \tag{C.9}$$

Figure C.1 illustrates the atmospheric absorption for an observer positioned 250 meters from the source. The results have been validated against ISO standards and clearly show that higher frequencies are more strongly attenuated. While atmospheric absorption has minimal impact across most of the audible spectrum, it becomes more significant at very high frequencies, which are generally less perceptible to the human ear. Nonetheless, the model was included in the simulation framework to ensure completeness.

C.3. Reflection and Refraction

Similar to light waves, sound waves are reflected and refracted when interacting with different media. At solid boundaries such as the ground or vegetation, part of the sound is reflected based on acoustic impedance, introducing phase shifts and partial absorption [102]. Refraction occurs due to wind and temperature gradients, bending sound toward regions of lower effective sound speed. This creates shadow zones (upward refraction) or enhances propagation (downward refraction), especially under temperature inversions or downwind conditions. Wind direction relative to the source-receiver path significantly impacts propagation, as shown in Figure 2.17 [98].

In flat, obstacle-free terrain, the sound reaches the observer through a direct and a single reflected path off the ground [17]. The longer path of the reflected wave introduces a phase shift, which can cause constructive or destructive interference. Anti-phase reflections reduce the observed SPL [103].

Altitude-dependent wind gradients further influence reflection behavior, as illustrated in Figure C.2. Downwind propagation increases sound speed, while upwind slows it down, resulting in curved ray paths. There

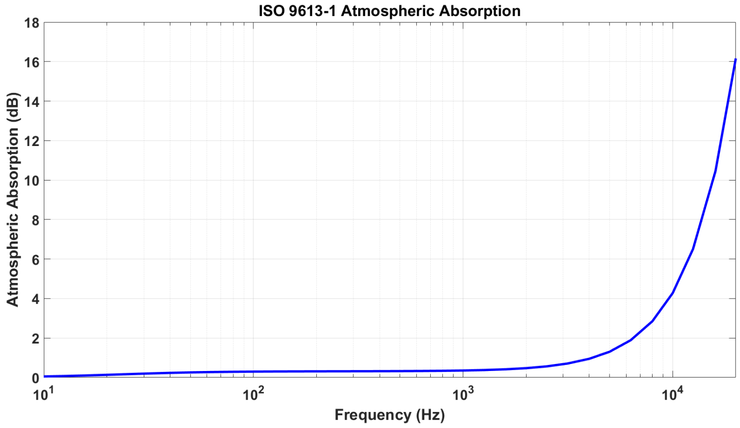

Figure C.1: Atmospheric absorption at a distance of 250 m with $T_a = 15°$, p_a=1 bar and relative humidity h=80%.

are multiple models that can simulate this, such as the one from DELTA manuals [103, 104] or the ray tracing implemented by Arntzen [98].

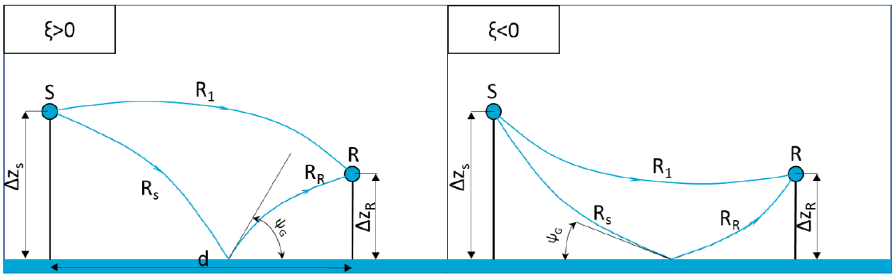

Figure C.2: Wind gradient effect on a reflected and refracted sound wave. Retrieved from Van Den Kieboom [17].

Figure C.3, retrieved from Arntzen [98], illustrates the bending of sound rays over distance. The source is placed at a height of 500 meters, which is slightly higher than the typical altitude of the Kitepower V9.60 kite but still within the same order of magnitude. The figure shows that a considerable distance is required for the sound wave to follow a noticeably curved path. As a result, a simplified model was adopted, using a straight ray with ground absorption, as shown in Figure C.4.

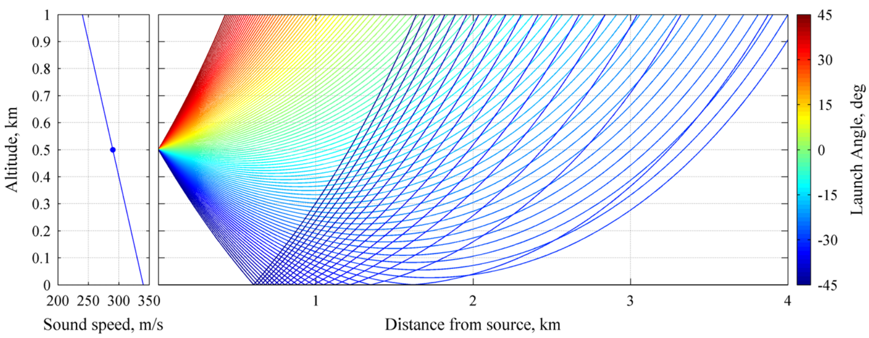

Figure C.3: Sound ray from a source at a height of 500 m in an atmosphere with decreasing gradient. Retrieved from Arntzen [98].

Due to the simplification mentioned earlier, the sound ray is modeled as a straight-line path, similar to a light ray. This approach is known as the two-path propagation model. When the positions of the source and observer are known, the distances for the direct path r_1 and the reflected path r_2 can be calculated as:

$$r_1 = \sqrt{(x_s - x_m)^2 + (h_s - h_m)^2} \tag{C.10}$$

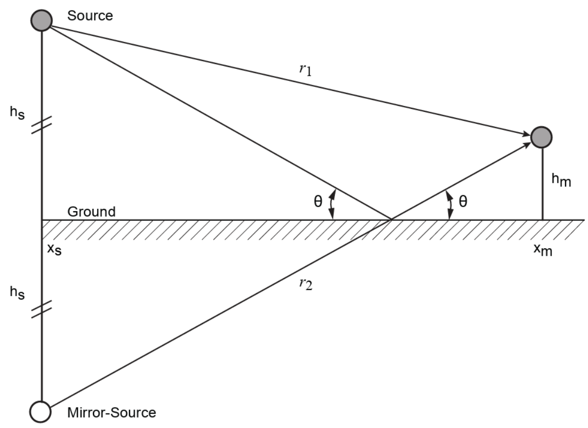

Figure C.4: Simple reflected ray with straight path. Retrieved from Arntzen [98].

$$r_2 = \sqrt{(x_s - x_m)^2 + (h_s + h_m)^2} \tag{C.11}$$

Here, the horizontal distance x and height h are illustrated in Figure C.4. The reflected ray is treated similarly to the direct ray, but some of its energy is absorbed upon contact with the ground, depending on the boundary material and frequency. Soft surfaces like snow and grass absorb more sound, while hard surfaces such as concrete and asphalt reflect more [98].

The phase difference between the two paths determines whether the interference is constructive or destructive. Atmospheric refraction and wind-induced attenuation can be estimated using the following expression, adapted from the DELTA model [103, 104]:

$$A_r = 20\log_{10}\left|1 + \frac{r_1}{r_2}\,Q(\Psi_G, \tau_2)\,e^{j\omega(\tau_2-\tau_1)}\right| \tag{C.12}$$

Here, τ_1 is the travel time of the direct path, while τ_2 is the travel time of the reflected path, including propagation from the source to the ground and then to the receiver. The grazing angle Ψ_G is the angle at which the sound ray hits the ground, similar to the reflection angle in optics. The angular frequency ω is defined as $2\pi f$, where f is the frequency of interest. The function $Q(\Psi_G, \tau_2)$ is the complex spherical reflection coefficient, describing how ground properties and frequency affect sound reflection and absorption. The full methodology for calculating Q and acoustic impedance is available in the DELTA documentation.

A simplified reflection model with constant ground impedance was implemented in MATLAB for testing. The simulation assumed a source emitting a constant SPL of 50 dB across frequencies at a distance representative of the kite operating altitude. Results showed SPL variations at the observer's position of about ±1.5 dB, depending on whether interference between direct and reflected paths was constructive or destructive. Given this small impact and the simplifications involved, the reflection model has been excluded from the final noise prediction framework in most of the tests.